

**University of Alberta**

Magnetosphere-Ionosphere Coupling During Substorms

by

Kyle R. Murphy

A thesis submitted to the Faculty of Graduate Studies and Research  
in partial fulfillment of the requirements for the degree of

Doctor of Philosophy

Department of Physics

©Kyle R. Murphy

Spring 2014

Edmonton, Alberta

Permission is hereby granted to the University of Alberta Libraries to reproduce single copies of this thesis and to lend or sell such copies for private, scholarly or scientific research purposes only. Where the thesis is converted to, or otherwise made available in digital form, the University of Alberta will advise potential users of the thesis of these terms.

The author reserves all other publication and other rights in association with the copyright in the thesis and, except as herein before provided, neither the thesis nor any substantial portion thereof may be printed or otherwise reproduced in any material form whatsoever without the author's prior written permission.

## **Abstract**

This thesis concerns the development and evolution of the magnetospheric substorm. In particular this thesis concentrates on the dynamics of Ultra Low Frequency (ULF) waves during the substorm growth and expansion phases, the coupling of the ionosphere and magnetosphere through substorm onset and the substorm expansion phase and the location in the magnetosphere and physical processes leading to substorm onset.

Firstly we present a superposed epoch analysis of ULF waves through the substorm growth and expansion phase, characterizing the two dimensional distribution of power spectral density and polarization of these waves with respect to auroral onset. We demonstrate that ULF wave power during substorms is characteristic of a power law and that the distribution of wave power and polarization is consistent with the expected pattern in the presence of a substorm current wedge.

Secondly we examine the global field aligned current (FAC) morphology through the substorm growth and expansion phase. We demonstrate, for the first time, that there is a clear reduction in FACs coupling the ionosphere and magnetosphere just prior to substorm onset. We suggest that this change in coupling may play an important role in the destabilization of the magnetosphere at substorm onset. We also present the first two-dimensional in-situ observation of the FACs and ionospheric current sheets comprising the substorm current wedge in the substorm expansion phase. We demonstrate that the structure of the substorm current wedge is significantly more complex than the classical view of the substorm current wedge.

Finally we present a comprehensive ground and in-situ analysis of two substorms to determine where in the magnetosphere the substorms initiate. We demonstrate that

both substorms initiate on closed field lines in the inner magnetosphere. More significantly we demonstrate that magnetic reconnection can follow substorm onset and that earthward magnetotail flows or auroral streamers, their ionospheric counterparts, are not a necessary condition for substorm onset.

## **Acknowledgements**

First off, I would like to thank my wife and best friend Hillary Sparkes whose love and support makes anything possible. Without her nothing is worth doing.

I would also like to express my deepest gratitude to my best man Dr. Jonathan Rae and to my groomsman and supervisor Dr. Ian Mann. Their friendship has meant the world to me. Without their guidance, support, and encouragement this thesis would not have been possible.

Special thanks goes out to the space physics group and in particular, Andy Kale, David Miles, David Milling and Clare Watt, whose helpful discussions over coffee and beer made this possible.

And many thanks to my parents, who were always supportive and interested in what I was doing.

I would also like to acknowledge and thank the Natural Sciences and Engineering Research Council of Canada and Alberta Innovates for financial support throughout this degree.

# Table of Contents

Chapter 1	Introduction .....	1
1.1	The Magnetosphere.....	1
1.2	The Ionosphere .....	4
1.3	Magnetosphere-Ionosphere Coupling .....	6
1.4	Magnetospheric Substorms .....	9
1.4.1	Phenomenological Model of Substorms .....	9
1.4.2	Substorm Expansion Phase Onset.....	11
1.4.3	ULF Waves and Substorms.....	14
1.4.4	FACs and the Substorm Current Wedge .....	15
1.5	References .....	17
Chapter 2	On the nature of ULF wave power during nightside auroral activations and substorms: Spatial Distribution.....	24
2.1	Introduction .....	24
2.2	Methodology.....	27
2.2.1	Data Sets .....	27
2.2.2	Data Processing.....	30
2.3	Analysis and Results .....	35
2.4	Discussion.....	44
2.5	Summary and Conclusions .....	54
2.6	References .....	55
Chapter 3	Reduction in Field-Aligned Currents Preceding and Local to Auroral Substorm Onset .....	60
3.1	Introduction .....	60
3.2	Instrumentation .....	61
3.3	Observations .....	62

3.4	Discussion and Conclusions .....	67
3.5	References .....	70
Chapter 4 The detailed spatial structure of field aligned currents comprising the substorm current wedge..... 74		
4.1	Introduction .....	74
4.2	Instrumentation .....	76
4.3	Observations .....	78
4.3.1	The 16 February 2010 Event .....	78
4.3.2	The 24 March 2011 Event .....	82
4.3.3	The 16 May 2011 Event.....	85
4.3.4	The Substorm Current Wedge .....	88
4.4	Discussion.....	91
4.5	Summary and Conclusions .....	100
4.6	References .....	101
Chapter 5 Inner-magnetospheric onset preceding reconnection during substorms .. 108		
5.1	Introduction .....	108
5.2	Instrumentation .....	111
5.3	Observations .....	114
5.3.1	Substorm 1, 04:15-04:45 UT .....	115
5.3.2	Substorm 2, 05:30-06:30 UT .....	121
5.4	Discussion.....	127
5.5	Conclusions .....	132
5.6	References .....	133
Chapter 6 Conclusions and Future Work..... 139		
6.1	References .....	141

## List of Figures

Figure 1.1: A schematic illustration of the Earth's magnetosphere. Image courtesy of the National Aeronautics and Space Agency (NASA). .....	3
Figure 1.2: A schematic of the Dungey cycle and the resulting convection of plasma and magnetic field (magnetospheric convections). Inset, the motion of the magnetic field and plasma projected on the ionosphere. Figure from Kivelson and Russell [1995] .....	4
Figure 1.3: Altitude profile of the electron density in the ionosphere. Taken from Kivelson and Russell [1995].....	5
Figure 1.4: A schematic illustrating the generation of the eastward and westward electrojets in the ionosphere and the foot prints of the region 1 (poleward) and region 2 (equatorward) FACs in the ionosphere.....	8
Figure 1.5: A schematic illustrating the region 1 and region 2 FACs and auroral electrojets, from <a href="http://www.meted.ucar.edu/">http://www.meted.ucar.edu/</a> .....	9
Figure 1.6: Schematic of the NENL and CD paradigms. Figure adapted from Rae et al. [2009]. .....	13
Figure 1.7: Schematic of the SCW. The top panel (a) illustrates the structure of an equivalent current system referred to as the substorm current wedge. The bottom panel (b) depicts the local-time and latitudinal structure of magnetic perturbations (left) in the presence of a modeled SCW (right). Figure from Clauer and McPherron [1974]. .....	15
Figure 2.1: The locations of 885 substorms (purple asterisk) identified in the Frey substorm database conjugate to the CARISMA (red triangles) and CANMOS (red squares) magnetometer stations. ....	30
Figure 2.2: The two-dimensional Pi1*, Pi1-2 and Pi2 waveband distribution of event occurrence with respect to the relative distance in CGM latitude and longitude of an individual station away from auroral onset for any particular substorm. Negative (positive) indicates the station is west/south (east/north) of auroral onset. The color bar indicates the number of magnetometer time-series in each spatial bin utilised to quantify both the ULF wave power and polarisation parameters.....	35
Figure 2.3: The two-dimensional spatial distribution of the logged median summed ULF wave power and median AE with respect to the location of auroral onset, c.f., Figure 2. Top row is the H-component ULF wave power middle row the D-component wave power and bottom the median AE for the respective event distributions. The left column	

is the summed Pi1\* power, middle the summed Pi1-2 power and right the summed Pi2 power. The color bar denotes the log of the median summed power where the median summed power is in units of nT<sup>2</sup>/mHz..... 36

Figure 2.4: The two-dimensional spatial distribution of the logged mean summed ULF wave power and mean AE with respect to the location of auroral onset. The figure is organised in the same format as Figure 3. Top middle and bottom rows are the H-component power, D-component power and mean AE respectively. The left, middle and right columns are the mean summed ULF wave power in the Pi1\*, Pi1-2 and Pi2 wavebands, respectively. The color bar denotes the log of the mean summed ULF wave power where the summed power is in units of nT<sup>2</sup>/mHz..... 38

Figure 2.5: The latitudinal decay of the mean and median summed H-component ULF wave power as a function of delta latitude in the Pi1\*, Pi1-2 and Pi2 wavebands (left, middle and right respectively). The y-axis is power (nT<sup>2</sup>/mHz) and the x-axis delta latitude (negative south and positive north). Green (blue) triangles are the mean north (south) ULF wave power and the green (blue) dashed line is the least absolute deviation fit to the triangles. The red (black) diamonds are the median north (south) ULF wave power and the solid black (red) line is the least absolute deviation fit to the diamonds.39

Figure 2.6: The longitudinal decay of the H-component ULF wave power in the Pi1\*, Pi1-2 and Pi2 wavebands (left, middle, right) as a function of delta longitude (negative west and positive east). Green (blue) triangles are the mean east (west) ULF wave power and the dashed green (blue) curve the least absolute deviation fit to the triangles. The red (black) diamonds are the median east (west) ULF wave power and the black (red) curve the fit to the diamonds. .... 40

Figure 2.7: The statistical ULF wave power spectra determined from all available magnetometer stations within  $|\Delta lat| \leq 3^\circ$  degrees and  $|\Delta long| \leq 25^\circ$  degrees. The top panel is mean (black), median (blue) and upper and lower quartile (dashed red) power spectra for the H-component magnetic field. The bottom panel is the same as the top for the D-component magnetic field. .... 42

Figure 2.8: The median two-dimensional distribution of the ULF wave angle of azimuth with respect to auroral onset in the Pi1\*, Pi1-2 and Pi2 wavebands (left, middle, right). The color bar depicts the angle of azimuth in radians bounded by  $[-\pi/2, \pi/2]$ . .... 43

Figure 2.9: The median two-dimensional distribution of ULF wave ellipticities in the Pi1\*, Pi1-2 and Pi2 (left, middle, and right) wavebands as a function of relative distance from auroral onset. The color bar denotes the value of ellipticity in each spatial bin..... 43

Figure 2.10: The distribution of the angle of azimuth between  $|\Delta lat| < 5^\circ$  just west of onset ( $-10^\circ < \Delta long < 0^\circ$ , left panels) and just east of onset ( $0^\circ < \Delta long < 10^\circ$ , right panels) in the Pi1\*, Pi1-2 and Pi2 wavebands (top, middle and bottom rows respectively). ..... 46

Figure 3.1:(a) The GSM x-component of the solar wind velocity (blue) and the GSM z-component of the solar wind magnetic field (black), the highlighted region denotes the time period during which the substorm is observed. (b) The G11 (blue) and G14 (red) inclination angle defined as the angle between the magnetic field and the vector sum of the x and y components in the local satellite ENP coordinate system. (c) G11 (blue) and G14 (red) total magnetic field strength. (d) FSIM ASI keogram; the keogram is constructed from a slice through the ASI perpendicular to the growth phase arc. (e) The H-, D-, and Z-component magnetic field variations from the FSIM magnetometer. .... 63

Figure 3.2: Auroral dynamics between 07:17:30-07:25:30 UT as observed by the FSIM (left) and FSMI (right) ASI and FSMI MSP. Top panel in each figure shows the mapped ASI data and the proton (blue) and electron (red) aurora from the FSMI MSP. The dotted blue line is a contour of constant CGM latitude at the peak in the proton aurora. The dotted red line marks the poleward edge of the electron aurora at constant CGM latitude. The poleward edge is determined by fitting the electron aurora intensity as a function of latitude to the functional form  $f(x) = A_0 \exp(-12 \times x - A_1 A_2^2)$ . The poleward boarder is then defined as  $A_1 + 1.5 A_2$  [Rae et al. 2004]. The bottom two images in each panel show the unmapped FSIM (left) and FSMI (right) ASI data. The yellow triangle in panel (a) marks the T96 traced north magnetic foot print of G11..... 64

Figure 3.3: The derived AMPERE FACs (red, upward and blue, downward) between 19 and 5 MLT during select ten minute quasi-stationary time periods and ground-based ECs at each station and interpolated onto a constant grid (green and purple, respectively) at the centre of each quasi-stationary period. The yellow triangles in (a) mark the location of G11 (west) and G14 (east) and the black circles denote the trajectory of a single AMPERE orbital track in the pre-midnight sector (~23 MLT). The green triangle in each panel marks the location of the FSIM ASI and magnetometer where auroral onset is observed. .... 65

Figure 3.4: (a) The AMPERE geomagnetic N-S and E-W magnetic field perturbations at 1 minute resolution from the pre-midnight orbital track (c.f. Figure 3(a)); the horizontal line marks the geomagnetic latitude of auroral onset at 66° CGM latitude. The vertical line in each panel marks auroral onset at 07:18:30 UT. (b) The AMPERE derived FACs in the auroral onset region at 23 MLT and from 65°-70° CGM latitude. (c) FSIM ASI keogram. (d) FSIM H-, D-, and Z-component magnetic field (blue, red and black respectively). (e) Integrated auroral intensity from select ASIs. .... 67

Figure 3.5: Derived FACs (red, upward and blue downward) for select times from substorms observed on 16 May 2011 (left) and 3 March 2011 (right). The diamond in each panel marks the location of the ASI in which the auroral onset was identified. On 16 May 2011 auroral onset was observed by the TPAS ASI at 08:25:30 UT and on 24 March 2011 auroral onset was observed by the FSIM ASI at 08:26:30 UT. Both events show a clear and localised decrease in the strength of the FACs just prior to auroral onset (row three of both columns). .... 68

Figure 4.1: The location of ground-based magnetometers (diamonds), ASI and MSP fields-of-view (purple and blue respectively). The north magnetic footprints of G11 and G13 are marked by blue triangles. .... 77

Figure 4.2: Summary of geosynchronous and ground-based observations for the 16 February 2010 substorm. (a) G11 total magnetic field (red) and inclination angle (blue). (b-d) H (blue), D (red), and Z (black) magnetic field variations from the DAWs, FSIM, and FSMI ground-based magnetometers, respectively. (e) FSIM keogram from the THEMIS ASI; the keogram is constructed from a slice through the ASI perpendicular to the growth phase arc and in the MLT sector of auroral onset. .... 79

Figure 4.3: AMPERE derived FACs for 16 February 2010 during selected ten minute time periods. Red denotes upward FAC and blue denotes downward FAC. The FACs are plotted as a function of corrected geomagnetic latitude and magnetic local time with noon towards the top and midnight towards the bottom. .... 80

Figure 4.4: A superposition of the THEMIS ASI aurora observations and night-side FACs during the substorm expansion phase on 16 February 2010. The left panel denotes the initial enhancement of the FAC system between 07:24-07:34 UT and the right panel the subsequent evolution of the FAC system between 07:36-07:46. In each column the three

rows overplot the aurora at the beginning, middle, and end of the ten minute window encompassing the AMPERE derived FACs (top, middle and bottom rows, respectively). 81

Figure 4.5: Summary of the geosynchronous magnetic field and ground-based magnetometer and ASI observations of a substorm on 24 March 2011. (a) The G13 total magnetic field (red) and inclination angle (blue). (b-c) DAWS, FSIM and FSMI magnetograms in the same format as Figure 2. (e) FSIM keogram in the same format as Figure 2. .... 83

Figure 4.6: AMPERE derived FACs during three time periods for the 24 March 2011 substorm. Red denotes upward FAC and blue downward FAC. .... 84

Figure 4.7: A superposition of the THEMIS ASI auroral observations and AMPERE derived FACs for the 24 March 2011 substorm between 08:32-08:42 UT in the same format as Figure 4. .... 85

Figure 4.8: A summary of the 16 May 2011 substorm. (a) The G13 geosynchronous magnetic field (red) and inclination angle (blue). (b-d) FSIM, FSMI and GILL magnetograms are in the same format as Figure 2. (e-f) Green line emissions from the FSMI and GILL NORSTAR MSPs. .... 86

Figure 4.9: AMPERE derived FACs for the 16 May 2011 substorm during selected periods in the same format as Figure 3. .... 87

Figure 4.10: Left column: Night-side AMPERE derived FACs during the substorm expansion phase for the three substorms. The Pi2 hodograms from selected auroral and low-latitude magnetometer stations are overplotted. The vertical color bar denotes the time sequence of each hodogram, such that the color evolution in the hodograms allows the polarization sense (clockwise or counter clockwise) to be inferred. Right column: The latitudinal summation of the AMPERE FACs as a function of MLT for each of the two-dimension AMPERE FAC topologies shown in the left column (black line). The strength of the H- and D-component auroral zone magnetic bays at the beginning (blue), middle (yellow) and end (red) of each ten minute window used to derive the AMPERE FACs are superimposed on each panel. In the bays positive H (north-south) points upward and positive D (east-west) points right as illustrated by the legend in the top right of each panel. .... 89

Figure 4.11: A schematic of the night-side FAC system during (a) the substorm growth phase,(b) prior to substorm onset, and (c) during the substorm expansion phase. In each

panel red denotes upward FAC and blue downward FAC. Panel (c) is a schematic of the fine structure of the upward and downward FAC seen by AMPERE and which on a large scale composes the SCW FAC current system. Higher longitudinal resolution studies are needed to resolve the onset region in panel (b). ..... 97

Figure 4.12: A schematic of the two dimensional FACs forming during the substorm expansion phase and the equivalent current system forming the SCW. The blue, green and red arrows represent the net upward FAC, the enhanced westward electrojet and the net upward FAC of the SCW. The azimuthal bands of upward and downward FAC, red and blue respectively, illustrate the complex structure of FACs forming during the expansion phase and comprising the SCW. .... 98

Figure 5.1: The location of ground-based instrumentation and in-situ spacecraft on 9th April 2011. The blue, orange, and red traces show the location of THEMIS A, E and D, respectively, between 4 and 7 UT, traced to the northern hemisphere. The THEMIS probes travel east to west and each circle marks a half hour interval. The purple and green triangles show the north magnetic footprints of GOES 15 and 13, respectively. The large black circles show the field of view of the GILL, SNKQ, and KUJ THEMIS ASIs. The black circles and pink outlines mark the location of ground-based magnetometer and riometers, respectively. .... 112

Figure 5.2: Overview of the in-situ and ground-based observations on 9th April 2011. The grey panels highlight the periods of interest. The first dashed line marks auroral onset during the first substorm. The second dashed line marks auroral onset in the second substorm and third dashed line mark a second auroral activation during the second substorm. (a) THEMIS A magnetic field strength (black) and magnitude the ion velocity (red). (b) THEMIS A ion flux. (c) GOES 15 magnetic field strength (black) and inclination angle (blue). (d) GOES 15 40 KeV electron flux (red) and 95 KeV ion flux (blue). (e) THEMIS ASI average intensity from the GILL (red) and KUJ (blue) ASIs. (f) Ground-based magnetometer observations of the H-component from the GILL and RANK magnetometers..... 115

Figure 5.3: Aurora observations from the GILL MSP and ASI during the initial substorm. (a) GILL MSP observations of the proton aurora H-beta (486 nm), overplotted as asterisks is the peak in the intensity of the proton aurora. (b) North-south keogram from the GILL ASI, overplotted as white and green circles are the latitude of the peak in the

proton aurora poleward edge of the electron aurora derived from data from the GILL MSP and the average intensity of the ASI (red). (c) East-West keogram from the GILL ASI showing the initial development of auroral beads at onset. The dashed white line marks auroral onset..... 117

Figure 5.4: (a) Select H-component magnetometer observations during the first substorm. Major tick marks represent 100 nT and minor tick marks 10 nT. (b) Riometer absorption from the RANK, ISLL and IQA riometers. Major tick marks represent 0.2 dB. The dashed line marks auroral onset..... 118

Figure 5.5: Select ground and in-situ observations during the first substorm. (a) North-south keogram from the GILL ASI overplotted with MSP boundaries in the same format as Figure 3b. (b) H-component magnetometer observations from the GILL (blue) and ISLL (red) magnetometers (left axis) and absorption from ISLL riometer (dotted red line, right axis). (c) Select energetic ion and electron fluxes from the GOES 15 MAGPD and MAGED instruments. (d) Same as (c) for GOES13. (e) Field aligned ion bulk flow from the THEMIS A probe. (f) ESA ion differential flux from THEMIS A probe. (g) Magnetic field strength from THEMIS A (blue), GOES 13 (orange), and GOES 15 (red). (h) Magnetic field inclination angle from THEMIS A (blue), GOES 13 (orange), and GOES 15 (red). ..... 119

Figure 5.6: Auroral observations during the second substorm. (a) North-south keogram from the KUUI ASI in the same format as Figure 3(b). (b) North-south keogram from SNKQ ASI in the same format as Figure 3(b). (c) Proton H-beta aurora from the GILL MSP in the same format as Figure 3(a). (d) and (e) East-west keograms from the KUUI and SNKQ ASIs during the initial auroral activation. (f) and (g) East-west keograms from KUUI and SNKQ during the secondary activation. The dashed white line marks auroral onset at SNKQ and the dashed yellow line marks the secondary auroral activation at KUUI..... 122

Figure 5.7: Select ground-based magnetometer and riometer observations during the second substorm. (a) H-component magnetometer, major ticks represent 500 nT. (b) Riometer absorption, major ticks represent 0.5 dB. The first dashed line marks auroral onset and the second dashed line marks the secondary auroral activation during the second substorm..... 123

Figure 5.8: Select ground-based and in-situ observations during the second substorm. The initial dashed line marks auroral onset and the second dashed line marks the time of the secondary auroral activation. (a) North-south keogram from the SNKQ ASI. (b) H-

component magnetometer traces. (c) Riometer absorption. (d) Select energetic ion and electron fluxes from GOES 15. (e) Same as (d) for GOES 13. (f) Field aligned plasma flow from THEMIS A. (g) Differential ion flux from THEMIS A. (h) Total magnetic field strength from THEMIS A, GOES 13, and GOES 15. (i) Magnetic field inclination angle from THEMIS A, GOES 13, and GOES 15..... 125

Figure 5.9: Observations of the ion plasma sheet from THEMIS A, E, D, GOES 15 and GOES 13 during the second substorm. The initial dashed line marks auroral onset and the second dashed line marks the time of the secondary auroral activation. (a-c) Energetic ion flux from THEMIS A, E and D, respectively. (d-f) GSM magnetic field at THEMIS A, E and D, respectively. (g) Energetic ion flux from GOES 15. (h) PEN magnetic field from GOES 15, see text for description of coordinate system. (i) Same as (g) for GOES 13. (j) Same as (h) for GOES 13. .... 126

## List of Tables

Table 2.1: CARISMA Stations.....	28
Table 2.2: CANMOS Stations.....	28
Table 2.3: The latitudinal decay scales ( $\Delta_{lat}$ ) of the mean and median summed ULF wave power in the Pi1*, Pi1-2 and Pi2 bands. ....	51
Table 2.4: The longitudinal decay scales ( $\Delta_{long}$ ) of the mean and median summed ULF wave power in the Pi1*, Pi1-2 and Pi2 bands.....	51

## Abbreviations, Nomenclature, and Symbols

1-40 second wave	Pi1
10-40 second wave	Pi1*
24-96 second wave	Pi1-2
40-150 second wave	Pi2
Active Magnetosphere and Planetary Electrodynamics Response Experiment	AMPERE
All Sky Imager	ASI
Auroral Electrojet Index	AE

Bursty Bulk Flow	BBF
Canadian Array for Realtime Investigations of Magnetic Activity	CARISMA
Canadian Magnetic Observatory System	CANMOS
Corrected Geomagnetic	CGM
Current Disruption	CD
Dawson City	DAWS
Earth Radii	$R_E$
Electron Gyro Frequency	$\Omega_e$
Electron-Neutral Collision Frequency	$\nu_{en}$
Electrostatic Analyser	ESA
Equivalent Currents	EC
Fast Fourier Transform	FFT
Field Aligned Current	FAC
Fort Simpson	FSIM
Fort Smith	FSMI
Geostationary Operational and Environment Satellites	GOES
GOES 11	G11
GOES 13	G13
GOES 14	G14
Gillam	GILL
Solar Magnetospheric	GSM
Imager for Magnetopause-to-Aurora Global Exploration spacecraft	IMAGE
Interplanetary Magnetic Field	IMF
Ion Gyro Frequency	$\Omega_i$
Ion-Neutral Collision Frequency	$\nu_{in}$
Iqaluit	IQA
Island Lake	ISLL
Kuujuuaq	KUUJ
Magnetic East	D
Magnetic North	H
Magnetic Vertical	Z
Magnetic Local Time	MLT

Magnetosphere-Ionosphere	M-I
Magnetospheric Electron Detector	MAGED
Magnetospheric Ion Detector	MAGPD
Meridian Scanning Photometer	MSP
Near-Earth Neutral Line	NENL
Near-Earth Geophysical Onset	NGO
Open-Closed Field Line Boundary	OCFLB
Pulsation, Continuous	Pc
Pulsation, Irregular	Pi
Power Spectral Density	PSD
Rankin Inlet	RANK
Sanikiluaq	SNKQ
Spectrographic Imager	SI-13
Substorm Current Wedge	SCW
The Pas	TPAS
Time History of Event and Macroscale Interaction	THEMIS
Ultra Low Frequency	ULF
Wide Imaging Camera	WIC
Westward Traveling Surge	WTS

# Chapter 1 Introduction

This thesis concerns the dynamics of the magnetospheric substorm, also referred to as a magnetic substorm, in the ionosphere as an auroral substorm, or just substorm for short. Magnetospheric substorms are characterised by an explosive release of energy accumulated in the night-side magnetosphere as a consequence of the coupling of the solar wind and interplanetary magnetic field (IMF) with the Earth's magnetosphere. This release of energy is most commonly associated with dynamic auroral displays in night sky. Primarily, this thesis concentrates on the ionospheric, and some related magnetospheric current dynamics around the onset of magnetospheric substorms.

The first Chapter of this thesis is an introduction to the magnetosphere and ionosphere, the coupling between these two regimes and an overview of the magnetospheric substorm. The second Chapter examines the nature of the spatial distribution of Ultra Low Frequency (ULF) waves through the substorm growth and expansion phases. Chapter 3 investigates the global field-aligned current (FAC) topology during the onset of a magnetic substorm and Chapter 4 provides a detailed analysis of the structure of these field-aligned currents following substorm onset. Chapter 5 utilises ground-based and in-situ observations of the substorm to determine the location of substorm onset in the magnetosphere. Finally, Chapter 6 provides a summary of the key results of each Chapter and details of future work. This thesis follows a papers format such that Chapters 2-5, inclusive, contain a self-contained, and in most cases, already published piece of research. Consequently references are included at the end of each chapter rather than combined into a single bibliography.

## 1.1 The Magnetosphere

The magnetosphere is the region of near-Earth space which is enclosed by the Earth's magnetic field. In near-Earth space, the Earth's magnetic field is a predominantly dipolar. However, interaction between the Earth's dipole field, the solar wind, and IMF leads to a more complex configuration of fields and plasma regimes. Figure 1.1 is a schematic of the Earth's magnetosphere and the dominant plasma regimes.

The Earth and its magnetic field act as an obstacle to the solar wind and IMF. Typical solar wind velocities are of the order of 300-500 km/s [Gosling et al., 1971], with

number densities of  $\sim 10^7 \text{ m}^{-3}$  with temperatures of  $\sim 10 \text{ eV}$  [Kivelson and Russell, 1995]. Typical values of the IMF are on the order of a few nanotesla. This gives an Alfvén speed on the order of 10 km/s and an acoustic speed of 100-300 km/s such that the solar wind is both super-Alfvénic and supersonic. Consequently, as the solar wind encounters the Earth’s magnetic field it is decelerated, forming a shock upstream called the bow shock. Inside of the bow shock is the magnetosheath where the bulk motion of the solar wind is decelerated and the kinetic energy of the plasma (acting like a fluid) is converted to heat leading to an increase in the temperature of the solar wind. The boundary of the magnetosphere forms inside the magnetosheath at an equilibrium position where the solar wind ram pressure and magnetic pressure are balanced by the Earth’s magnetic field pressure. The outer edge of the magnetosphere is referred to as the magnetopause and typically forms at a distance of  $\sim 10$  Earth radii ( $R_E$ ). When the solar wind impacts the magnetopause it compresses the day-side magnetic field and is diverted along the flanks towards the night-side. On the night-side of the Earth the diverted solar wind compresses the magnetic field forming the magnetotail, an elongated cavity which stretches away from the Earth. This complex geometry supports a variety of plasma regimes including: the plasmasphere, a dense region of plasma close to the Earth; the radiation belts, a region of relativistic ions and electrons; and the night-side plasma sheet, a region of warm plasma in the equatorial plane of the magnetotail (c.f., Figure 1.1). In addition to compressing the day-side field and elongating the night-side field, the solar wind can directly interact with the Earth’s magnetic field through the process of magnetic reconnection. This creates an “open” magnetosphere and allows mass, energy and momentum to be transferred from the solar wind into the magnetosphere [Dungey, 1961].

In general plasma and magnetic fields are coupled together such that they can be considered to move together, this is referred to as the frozen-in flux condition [e.g., Kivelson and Russell, 1995]. When two different frozen-in plasma and magnetic field regimes come together they form a boundary where they come into contact which separates the two plasma populations in two distinct regions. However, on small scales the frozen in flux condition breaks down and the plasma and magnetic field decouple such that the magnetic field is able to diffuse through the plasma and across the boundary [e.g., Baumjohann and Treumann, 1997]. In these regions, if the magnetic

fields are anti-parallel they are able to participate in magnetic reconnection whereby the magnetic field in one regime is cut and reconnected to the magnetic field from the distinct and separate plasma regime, forming an entirely new and inter-connected magnetic field topology. Further, in the vicinity of magnetic reconnection the new magnetic field topology allows plasma to diffuse across the previously closed boundary separating the two plasma regions. This allows the exchange of mass, energy and momentum between two previously separate systems [e.g., Baumjohann and Treumann, 1977].

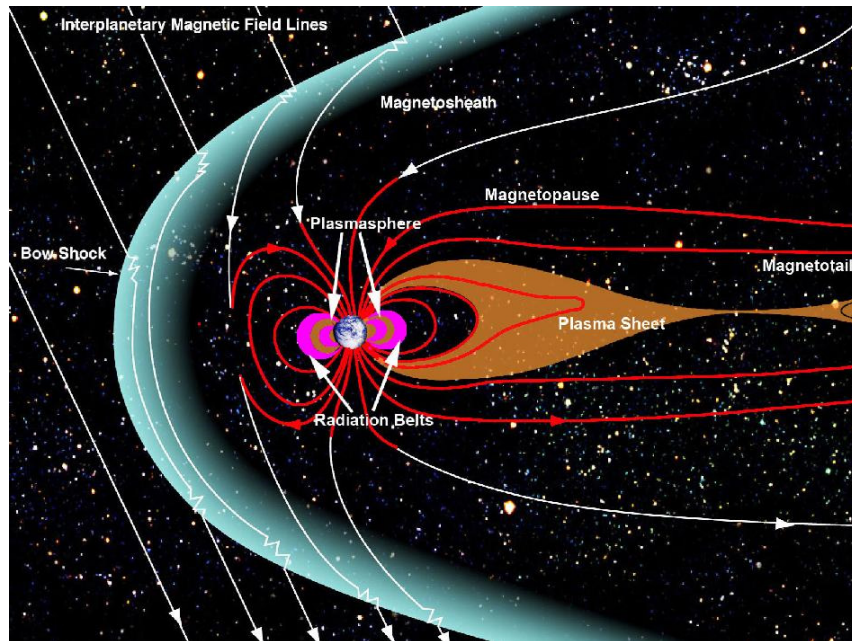


Figure 1.1: A schematic illustration of the Earth's magnetosphere. Image courtesy of the National Aeronautics and Space Agency (NASA).

Figure 1.2 is a schematic of an open magnetosphere [Dungey, 1961]. A predominantly southward IMF reconnects with the northward field of the dayside magnetosphere, illustrated by 1 and 1'. This creates two new open magnetic field lines; one emanating from the northern pole and the other from the south, shown as 2 and 2' respectively. The open magnetic field is then dragged by the solar wind from the day-side over the polar cap (region of open field lines) and onto the night-side (positions 3-5 and 3'-5') where the two open field lines once again may take part in reconnection, 6 and 6'. The now closed magnetic field convects into the inner magnetotail along the dawn and dusk flanks and then back to the day side where the process is repeated. The entire process is

referred to as the Dungey cycle or magnetospheric convection. The inset of Figure 1.2 depicts the motion of the footprints of magnetic field lines and plasma in the ionosphere, a region of imperfectly conducting plasma at altitudes between ~60 and 1000 km (see section 1.2). The shaded region is referred to as the auroral zone (or the auroral oval) where the quiescent aurora resides, and the boundary between the polar cap and auroral oval represents the boundary between open and closed magnetic field lines in the magnetosphere.

In general the rates of reconnection on the day- and night-side are unbalanced. This can lead to an accumulation of energy in the night-side magnetosphere as energy is transferred from the day-side to the night-side via day-side reconnection. When reconnection on the night-side initiates it can be abrupt, explosively releasing the stored energy whilst transitioning to a lower energy state. This transition is referred to as a magnetospheric substorm [McPherron, 1979] and is discussed in detail in section 1.4.

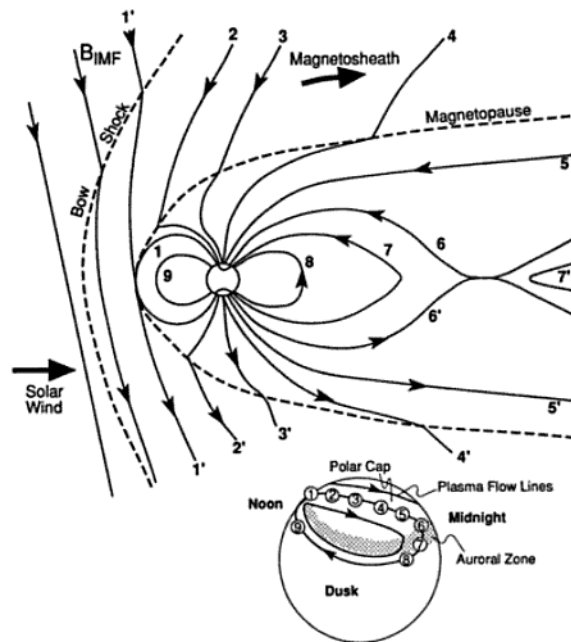


Figure 1.2: A schematic of the Dungey cycle and the resulting convection of plasma and magnetic field (magnetospheric convections). Inset, the motion of the magnetic field and plasma projected on the ionosphere. Figure from Kivelson and Russell [1995]

## 1.2 The Ionosphere

The region between the magnetosphere and neutral atmosphere is the ionosphere, a region of partially ionised plasma. The ionosphere is formed primarily by

photoionization by solar UV and EUV radiation [Kivelson and Russell, 1995] though the precipitation of energetic particles from the magnetosphere can also contribute to enhanced ionisation especially at higher latitudes [Baumjohann and Treumann, 1997]. In general the ionosphere lies between altitudes of 60-1000 km and is divided into three layers, the D-, E- and F-regions, and is where there are sufficient free electrons to influence the propagation of radio waves [e.g., Ratcliffe, 1972].

The D-region is characterized as the lower ionosphere. It exists predominantly on the day-side and consists of a weakly ionized plasma and is dominated by neutral gas [e.g., Kivelson and Russell, 1995]. The E- and F-regions comprise the upper ionosphere (altitudes above ~95 km) and in general exist on both the day- and night-side. The E-region is characterized by a highly but still partially ionized plasma and a local maximum in the number density of electrons. The F-region forms at altitudes above ~200 km and is characterized by the peak in the electron number density [Baumjohann and Treumann, 1997]. The E- and F-regions of the ionosphere are where ionospheric electrojet currents flow and where aurora are produced [e.g., Kivelson and Russell, 1995]. **Error! Reference source not found.** shows how the ionospheric free electron density varies with height and contains discrete transitions defining the D-, E- and F-regions.

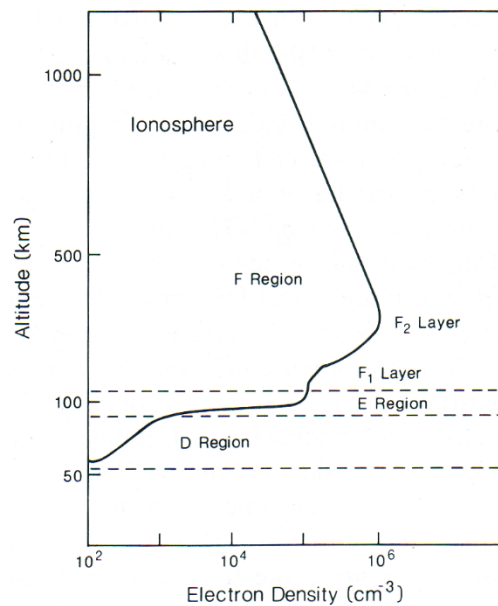


Figure 1.3: Altitude profile of the electron density in the ionosphere. Taken from Kivelson and Russell [1995].

### 1.3 Magnetosphere-Ionosphere Coupling

Magnetosphere-ionosphere coupling refers to the processes which connect the lower-altitude ionosphere and the higher-altitude magnetosphere potentially allowing the transfer of mass, energy and momentum between the two systems. This coupling can occur via field-aligned currents (FACs) [Sugiura, 1984], via particle precipitation from the magnetosphere [Cowley, 1993] or via outflow from the ionosphere [Schunk, 2013] which can be driven by pressure gradients [e.g., Vasyliunas 1970], waves [e.g., Watt and Rankin, 2012] as well as electric fields [e.g., Winningham and Gurgiolo, 1982]. Here we concentrate on FACs which are carried by the shear-Alfvén wave [Strangeway 2013] and the dominant process coupling the magnetosphere and ionosphere [Lu et al., 1995].

The FACs coupling the ionosphere and magnetosphere can broadly be characterized into two categories: (1) quasi-static currents driven by magnetospheric convection [e.g., Cowley, 1993 and Cowley 2013] and (2) dynamic FACs driven by spatially and temporally localized processes in the magnetosphere such as waves [e.g., Baumjohann and Glassmeier, 1984], pressure gradients [e.g., Vasyliunas 1970] as well as the formation of the substorm current wedge [e.g., Olson, 1999]. In this section we will qualitatively discuss magnetosphere-ionosphere coupling as a result of convection and will discuss the latter in the following section with reference to magnetospheric substorms. A detailed mathematical derivation of FACs can be found in Strangeway [2013] and Cowley [2013]. In addition a detailed overview of the shear-Alfvén was provided by Murphy [2008].

Many magnetospheric and ionospheric current systems are driven as a result of the interaction of the solar wind and IMF with the Earth's magnetic field and the resulting magnetospheric convection and motion of the solar wind across the magnetopause during predominantly southward IMF [e.g., Cowley, 2013]. Along the day-side magnetopause there exists a curl in the magnetic field (between the southward IMF and northward magnetic field of the Earth, c.f., Figure 1.1) which drives a current along the magnetopause [e.g., Cowley, 1993]. On the dayside the magnetopause current sheet closes in the high-latitude ionosphere as downward FACs on the dawn-side flank and upward FACs on the dusk-side flank [e.g., Cowley, 1993]. On the night-side the magnetopause current sheet closes via the cross-tail current [Baumjohann and

Treumann, 1997] which forms in the near-equatorial plane between regions of anti-parallel magnetic field (c.f., the magnetopause current), which itself forms as the result of magnetospheric convection and the consequent formation of the magnetotail [e.g., Kivelson and Russell, 1995].

The motion of magnetic field lines in the ionosphere (c.f., Figure 1.2) also leads to the formation of the eastward and westward electrojets, large scale ionospheric current systems [Cowley, 1993]. As magnetic field and plasma drifts over the poles and onto the dawn and dusk flanks and back to the day-side, an electric field is generated in the ionosphere perpendicular to both the magnetic field and motion of the magnetic field. In the presence of perpendicular electric and magnetic fields the plasma in the ionosphere undergoes E-cross-B drift. Typically, in a collisionless plasma, both ions and electrons undergo the same E-cross-B drift [e.g., Baumjohann and Treumann, 1997]. However, in the ionosphere, ions typically drift more slowly than electrons due to collisions with other ions and neutral elements. In general the ion motion in the ionosphere has two terms [Cowley, 2013]. The first term is in the E-cross-B direction. The second term is directed along the electric field  $E$  and proportional to  $v_{in}/\Omega_i$  where  $v_{in}$  is the ion-neutral collision frequency and  $\Omega_i$  is the ion gyro frequency. Above  $\sim 125$  km  $v_{in}/\Omega_i$  is small such that ion drift is predominantly the E-cross-B drift. Below  $\sim 125$  km  $v_{in}/\Omega_i$  becomes large such that the E-cross-B motion becomes negligible and the motion of the ions is predominantly aligned with the electric field. In general the same is true for electrons however the motion is governed by the electron-neutral collision frequency which is small such that  $v_{en}/\Omega_e$  can be neglected everywhere in the ionosphere. This leads to a decoupling of ions and electrons below altitudes of  $\sim 125$  km such that electrons move predominantly in the direction of E-cross-B and the ions in the directions of the electric field [Cowley, 2013]. This decoupling of the ions and electrons in the ionosphere creates a net current flow in the ionosphere. These currents can include the eastward and westward electrojets which are carried by the electrons as Hall currents flowing perpendicular to the electric field [e.g., Kivelson and Russell, 1995] as well as Pedersen currents which flow parallel to the ionospheric electric field and are carried by the ions. Figure 1.4 is an idealized schematic showing the formation of the eastward and westward auroral electrojets. The black lines depict the motion of magnetic field as the result of magnetospheric convection; note the magnetic field is directed into the page

(as in the northern hemisphere). The grey arrows show the direction of the electric field, a result of the motion of the magnetic field lines, and the thick black arrows show the subsequent E-cross-B drift of ions and electrons. The red and blue arrows depict the eastward and westward electrojets, respectively, the ionospheric current system being generated as a result of the differential motion of ions and electrons in the ionosphere. The FACs poleward of the auroral electrojets are the region 1 FACs and the equatorward FACs are the region 2 FACs [Iijima and Potemra, 1976] and are closed via ionospheric Pedersen currents.

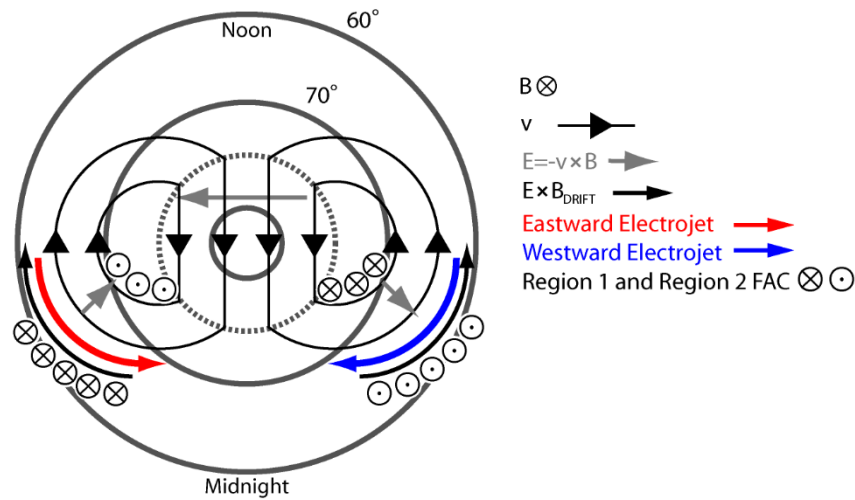


Figure 1.4: A schematic illustrating the generation of the eastward and westward electrojets in the ionosphere and the foot prints of the region 1 (poleward) and region 2 (equatorward) FACs in the ionosphere.

As the magnetic field convects from the magnetotail into the inner-magnetosphere it drags with it the magnetotail plasma, a result of the frozen in flux condition where the motion of the magnetic field and plasma are coupled together [e.g., Kivelson and Russell, 1995]. In the inner-magnetosphere, as plasma is convected from the tail it drifts around both flanks and is onto the dayside. The gradient-curvature drift of energetic particles in the inner magnetosphere leads to the formation of a westward azimuthal current referred to as the ring current [Kivelson and Russell, 1995]. Superimposed onto the gradient-curvature drift is the E-cross-B motion of the plasma due to the dawn-dusk electric field which displaces the entire system of plasma sunward. This creates a plasma distribution (or density profile) with a maximum at midnight and a minimum at noon. To maintain a quasi-neutral magnetosphere or current continuity within the

magnetosphere this requires current flow into the ionosphere at dusk and out of the ionosphere at dawn [Cowley, 2013]. These currents are the region 2 FACs.

Figure 1.5 is a schematic illustrating the current systems coupling the magnetosphere and ionosphere. Figure 1.5 shows the region 1 (poleward) and region 2 (equatorward) FACs and the Pedersen currents which connect the two sets of FACs allowing the currents to close in the ionosphere. The Hall currents illustrated in Figure 1.5 are the eastward and westward auroral electrojets.

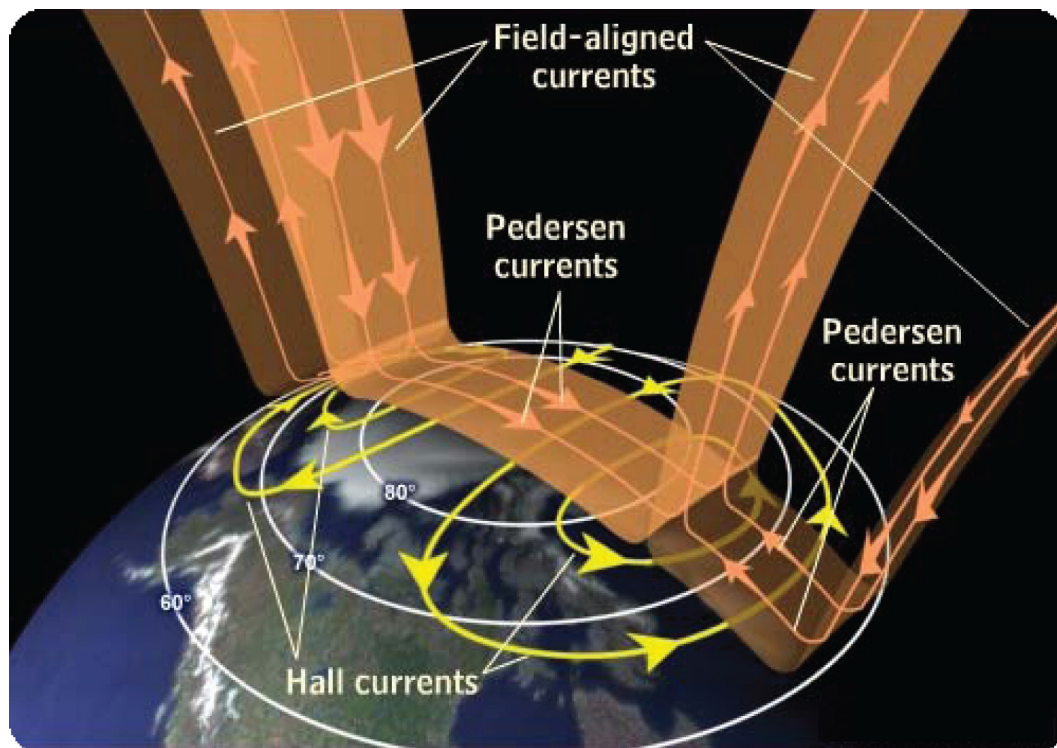


Figure 1.5: A schematic illustrating the region 1 and region 2 FACs and auroral electrojets, from <http://www.meted.ucar.edu/>.

## 1.4 Magnetospheric Substorms

### 1.4.1 Phenomenological Model of Substorms

The magnetic substorm has been studied in great detail for over a century. In the early 1900's Birkeland [1908 and 1913] noted auroral displays on the night-side were associated with large scale perturbations of the Earth's magnetic field. Birkeland [1908] postulated that these perturbations were the result of FACs coupling to an east-to-west current in Earth's upper atmosphere. Birkeland referred to these events as polar

storms. With the introduction of more advanced instrumentation and an increased understanding of magnetosphere, ionosphere and plasma physics, researchers began developing a more complete view of substorms. In 1958, Heppner [1958] demonstrated that the brightening and expansion of the most equatorward pre-midnight auroral arc was strongly associated with perturbations of the Earth's magnetic field. In 1964, Akasofu [1964] introduced the term "auroral substorm", which described three distinct phases of auroral morphology: the quiet phase, which was characterised by a bright but typically quiescent auroral oval. The expansion phase, characterised by a brightening of the most equatorward auroral arc followed by an explosive east, west and poleward expansion of the aurora on the night-side, and finally the recovery phase, characterised by a gradual dimming of the aurora and migration back toward the equator.

In the late 1960's, space-borne observations of the night-side magnetosphere demonstrated that the auroral substorm was not confined to the ionosphere. Vasyliunas [1968] observed the inward convection of electrons during the expansion phase and Cummings et al. [1968] noted there was a strong depression and stretching of the night-side magnetic field prior to expansion phase onset, followed by a rapid recovery to a dipole-like field closely coincident with the expansion phase of the auroral substorm. These results, along with ground-based observations of increased magnetic activity prior to the expansion phase of the auroral substorm [McPherron et al., 1968 and Rostoker, 1968] led to development of the magnetospheric substorm paradigm [McPherron, 1970 and 1979], a phenomenological framework describing a magnetic substorm as a sequence of events in the Earth's magnetosphere which are manifested in, and coupled to, the ionosphere.

Similar to Akasofu's auroral substorm [Akasofu, 1964], the process of the magnetospheric substorm is now characterised by three distinct phases; the growth, expansion and recovery phases [McPherron, 1979]. The growth phase is characterised by a storage of energy in the night-side magnetosphere. Energy is extracted from the solar wind on the day-side (via magnetic reconnection) and stored in the night-side magnetosphere as magnetic flux and plasma is convected from the day-side to the night-side [Dungey, 1961]. As energy is being stored and more flux and plasma is convected onto the night-side, the magnetic field becomes stretched and compressed,

and a current sheet forms in approximately the equatorial plane between regions of anti-parallel magnetic field (the cross tail current sheet). This region of the night-side magnetosphere is referred to as the magnetotail. In the ionosphere the substorm growth phase is manifested as a migration of the auroral oval to lower latitudes and an enhancement of the east and west ionospheric electrojets [McPherron, 1979].

The expansion phase is defined by the explosive release of energy stored during the growth phase. The cross-tail current is diverted into the ionosphere, the magnetosphere dipolarizes, and magnetic reconnection in the tail is initiated or further enhanced [McPherron, 1979]. The substorm current wedge (SCW) forms in the magnetotail carrying the diverted cross-tail current into and out of the ionosphere [Clauer and McPherron, 1974] enhancing the westward electrojet [Rostoker et al., 1975]. During the expansion phase the aurora brightens and becomes extremely dynamic (c.f., the expansion phase of the auroral substorm [Akasofu, 1964]). Following the expansion phase, the SCW begins to dissipate, the auroral expansion subsides, and the auroral oval retracts to lower latitudes. This phase is referred to as the recovery phase of the magnetospheric substorm [McPherron, 1979].

The phenomenological model of the magnetospheric substorm presented by McPherron [1979] is still widely accepted today; however there remain a number of aspects of the magnetospheric substorm which remain controversial and continue to be debated by researchers. In particular the physical mechanism leading to the initiation of the substorm expansion phase, the dynamics of the expansion phase and the resulting formation of the SCW and expansion of the aurora, has been fiercely debated since the initial phenomenological model of the substorm [see for instance Baker et al., 1996; Lui et al., 1996]. In the following sections we will discuss the substorm expansion phase and the controversy surrounding the expansion phase, ULF waves and their role in the dynamics of the substorm and magnetosphere-ionosphere coupling through the expansion phase and specifically the formation and development of the SCW.

## **1.4.2 Substorm Expansion Phase Onset**

In the ionosphere, the substorm expansion phase is manifested as the brightening of the aurora and subsequent auroral breakup, and in the magnetotail by the onset of reconnection and the disruption of the cross-tail current. The inability to adequately

determine the relative start time of these signatures in the ionosphere and in the magnetosphere has continued to be a major pitfall for unambiguously determining the physical mechanism responsible for triggering the onset of the substorm expansion phase and has led to considerable controversy [see, for example, the debate Angelopoulos et al., 2008a; Lui, 2009; Angelopoulos et al., 2009]. The expansion phase controversy largely relates to whether current disruption via a localized plasma instability [Lui, 1996], in the near-Earth magnetosphere ( $\sim 10 R_E$ ), precedes magnetic reconnection further down tail ( $\sim 25 R_E$ ) and is responsible for initiating the substorm expansion phase, or vice versa [Baker et al., 1996]. The reconnection driven model is referred to as the near-Earth neutral line (NENL) model and the near-Earth plasma instability model as the current disruption (CD) model.

In the NENL model, reconnection in the magnetotail at a distance of  $\sim 20 R_E$  (referred to as the Near-Earth Neutral Line) triggers the onset of the substorm expansion phase [e.g., Baker et al., 1996]. As reconnection in the magnetotail commences, open magnetic field lines are closed, the energy stored in the magnetotail is released and the night-side magnetotail dipolarizes. The energy released is believed to accelerate bursty bulk plasma flows (BBFs) toward the Earth [Angelopoulos et al., 1992]. As these flows propagate inward they encounter a stronger and more dipolar magnetic field and decelerate [Shiokawa et al., 1997]. The accumulation of plasma and the dipolarization of the Earth's magnetic field disrupts the cross-tail current, diverting it into the ionosphere and forming the SCW in the magnetotail [Shiokawa et al., 1997]. Following reconnection and current disruption in the magnetotail, auroral breakup is then observed in the ionosphere. The sequence of events hypothesized by the NENL model is referred to as "outside-to-in" as the expansion phase onset is triggered in the mid-distant magnetotail, and is subsequently followed by current disruption and then auroral break up closer to the Earth. Figure 1.6 is a schematic illustrating the location of auroral break up, current disruption and reconnection during the expansion phase onset. The inset panel (ii) depicts the sequence of events proposed in the NENL substorm paradigm. A modified NENL paradigm also exists which suggests that an inward transport of plasma by high velocity flows generated via reconnection may lead to a destabilization of the inner magnetotail, via a local plasma instability, and onset of the substorm expansion phase [Nishimura et al., 2010].

In the CD model, the expansion phase onset is triggered by a localized plasma instability which disrupts the cross-tail current [Lui, 1996]. The plasma instability has been hypothesized to be a ballooning mode [e.g., Roux et al., 1991], lower hybrid turbulence [e.g., Huba et al., 1977], or a cross-field current instability in the central plasma sheet [e.g., Lui et al., 1991] to name a few. The formation of the SCW and auroral breakup develop as a consequence of this current disruption. Following the initial disruption of the cross-tail current, a rarefaction wave is launched which propagates down the tail and subsequently triggers reconnection at the NENL [Angelopoulos, 2008a]. The CD model is referred to as “inside-to-out” as the expansion phase onset is triggered in the inner magnetotail. The top inset (i) of Figure 1.6 depicts the sequence of events observed in the CD model.

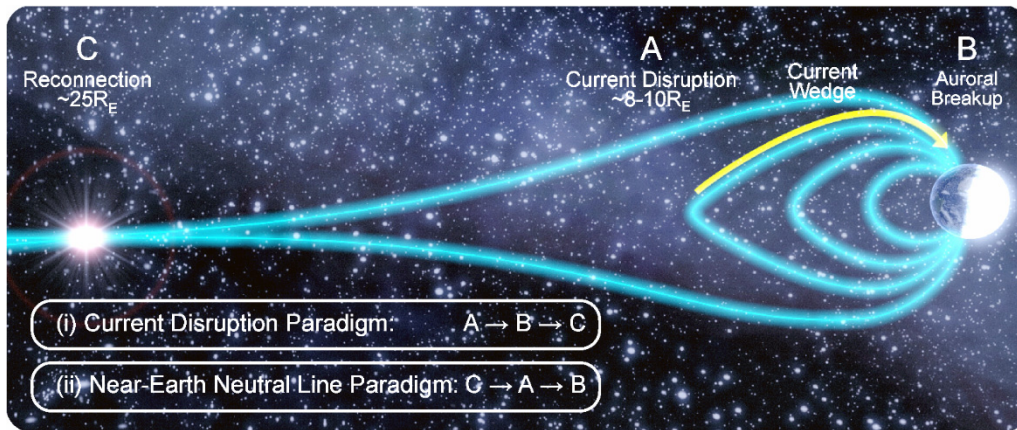


Figure 1.6: Schematic of the NENL and CD paradigms. Figure adapted from Rae et al. [2009].

Recent work utilizing the Time History of Events and Macroscale Interactions during Substorms (THEMIS) mission [Angelopoulos, 2008b] has shown strong evidence for both reconnection [Angelopoulos et al., 2008a; Nishimura et al. 2010] and the potential action of a near-earth instability [Rae et al., 2009] in triggering substorm expansion phase onset. The quantitative analysis of the sequence of events and morphology of the magnetospheric and ionospheric signatures of a substorm is essential in order to fully resolve this controversy. Research relating to the substorm expansion phase is presented in Chapters 2, 3, 4, and 5.

### 1.4.3 ULF Waves and Substorms

Ultra Low Frequency (ULF) waves, also called geomagnetic micropulsations, are waves classified with periods between about 1 and 1000s (1 mHz – 1 Hz) [Jacobs et al., 1964]. In the magnetosphere and ionosphere these wave can be observed in the aurora [e.g., Samson et al., 2003] in the electric [e.g., Takahashi et al., 2010] and magnetic fields [e.g., Lee et al., 2007]. These waves can be driven by the excitation of field line resonance [e.g., Rae et al., 2005], by solar wind impulses impacting the Earth's magnetosphere, or by the impulsive release of energy within the magnetosphere such as during the substorm expansion phase [e.g., Milling et al., 2008]. The former are referred to as continuous ULF waves [Jacobs et al., 1964]. These waves are typically relatively monochromatic and last for several wave periods [e.g., Mann et al., 2002]. The latter are referred to as impulsive ULF waves [Jacobs et al., 1964]. These impulsive ULF waves are typically short lived wavepackets observed during substorms [e.g., Bösinger et al., 1981; Olson, 1999]. The ULF waves observed and studied herein are impulsive ULF waves associated with onset of the substorm expansion phase.

The irregular and impulsive ULF waves observed during the substorm expansion phase are referred to as Pi pulsations [Jacobs et al., 1964] and are sub-categorized into three groups [e.g., Jacobs et al., 1964 and Bösinger et al., 1981]. These groups are, Pi2 pulsations with periods of 40-150s, Pi1 pulsations with periods 1-40s [Jacobs et al., 1964] and PiB pulsations (also referred to as Pi1B pulsations) with periods less than ~10s [e.g., Bösinger et al., 1981]. Pi2 pulsations are typically large amplitude pulsations associated with the formation of the SCW, cavity mode resonances [e.g., Olson, 1999], and large amplitude plasma flows in the magnetotail [e.g., Kepko et al., 1999 and Murphy et al., 2008]. Pi1 pulsations are typically smaller amplitude waves intimately connected with the substorm expansion phase and auroral breakup [Posch et al., 2007], though recent work has shown that Pi2 pulsations exhibit similar characteristics as the Pi1 waves during auroral breakup and preceding the formation of the substorm current wedge [e.g., Rae et al., 2009 and Murphy et al., 2009]. In the initial classification of Pi1 and Pi2 waves Jacobs et al. [1964] noted that the sub-classification into Pi1 and Pi2 waves was based only on period and not any distinction in physical drivers. Chapter 2 presents a detailed superposed epoch analysis of Pi1 and Pi2 wave power and

polarization through substorm expansion phase onset to determine whether there exists any statistical observational difference between the characteristics Pi1 and Pi2 waves.

### 1.4.4 FACs and the Substorm Current Wedge

The substorm current wedge (SCW) is an integral part of the substorm expansion phase, forming as a result of the disruption of the cross tail current and dipolarisation of the Earth's magnetosphere following substorm onset [McPherron, 1979]. A detailed model of the SCW was first presented by McPherron et al. [1973]. These authors used ground-based magnetometer observations to develop a model of the SCW coupling the ionosphere and magnetosphere during the substorm expansion phase [McPherron et al., 1973; see also Clauer and McPherron 1974]. This current system consisted of a downward FAC element in the morning sector, an enhanced westward electrojet, and an upward FAC in the dusk sector [McPherron, 1973]. Figure 1.7 is a schematic of the SCW, the left inset depicts the North/South and East/West deflections of the magnetic field observed by ground-based magnetometers and the right inset a simple equivalent current system used to model the ground-based deflections.

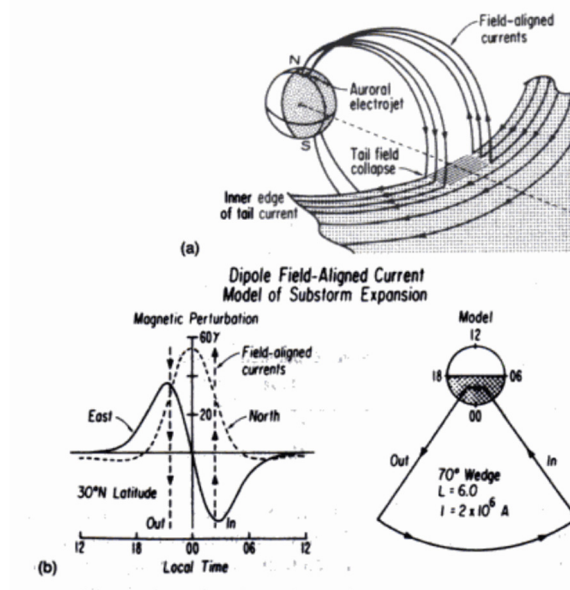


Figure 1.7: Schematic of the SCW. The top panel (a) illustrates the structure of an equivalent current system referred to as the substorm current wedge. The bottom panel (b) depicts the local-time and latitudinal structure of magnetic perturbations (left) in the presence of a modeled SCW (right). Figure from Clauer and McPherron [1974].

The generation of the SCW is widely believed to be the result of the disruption of the cross tail current sheet in the magnetotail following substorm onset regardless of whether onset occurs as a result of reconnection or a local plasma instability [e.g., Baker et al., 1996 and Lui 1996]. The substorm expansion phase is clearly associated with the injection of high energy particles [e.g., Vasyliunas, 1968], high speed plasma flows [e.g., Angelopoulos, 2008a] and reconfiguration of the magnetic field in the tail [e.g., Cummings et al., 1968] all of which can lead to the development of shear-Alfvén waves in the magnetotail and FACs coupling the ionosphere and magnetosphere [e.g., Strangeway, 2013]. The injection of plasma in the inner magnetosphere during substorms creates pressure gradients in the tail which subsequently leads to the establishment of FACs [Vasyliunas, 1970]. As high speed flows propagate into the inner magnetosphere they are decelerated as they encounter a stronger and more dipolar magnetic field which also leads to the generation of FACs [Shiokawa et al., 1997]. Finally, the reconfiguration of the magnetic field can lead to localised gradients in the magnetic field which in turn establish FACs coupling the ionosphere to the magnetosphere [e.g., Lui, 1996; Anderson et al., 2000; Iijima, 2013].

To date, developing a comprehensive model of the substorm current wedge in the ionosphere and magnetosphere has been limited by the availability of in-situ measurements and the limitations of ground-based observations. An array of ground-based magnetometers can provide a large-scale two-dimensional view of the equivalent currents in the SCW in the ionosphere [Smith et al., 2002]. However, in general, ground-based magnetometers cannot differentiate between FACs and ionospheric current sheets [Fukushima, 1969]. In addition, single point spacecraft measurements in the magnetosphere provide localized observations of the FACs and magnetic field deflections associated with the SCW [Nagai, 1982] or at best statistical distributions of FACs through multiple substorms [Iijima and Potemra, 1978].

Developing a detailed two-dimensional view of the FACs coupling the ionosphere and magnetosphere through the substorm growth and expansion phase and the formation of the SCW is the topic of Chapters 3 and 4. This is accomplished using the Active Magnetosphere and Planetary Electrodynamics Response Experiment (AMPERE) [Anderson et al., 2000; Waters et al., 2001] which utilizes magnetometer data from 66

satellites in low-Earth orbit to produce a global view of the FACs coupling the magnetosphere and ionosphere. AMPERE and the FACs coupling the ionosphere and magnetosphere are discussed in detail in subsequent chapters.

## 1.5 References

- Akasofu, S. I. (1964), The development of the auroral substorm, *Planet. Space Sci.*, 12, 273-282.
- Anderson, B. J., K. Takahashi, and B. A. Toth (2000), Sensing global Birkeland currents with iridium® engineering magnetometer data, *Geophys. Res. Lett.*, 27(24), 4045–4048.
- Angelopoulos, V., et al. (1992), Bursty Bulk Flows in the Inner Central Plasma Sheet, *J. Geophys. Res.*, 97(A4), 4027-4039.
- Angelopoulos, V., et al. (2008a), Tail reconnection triggering substorm onset, *Science*, 321(5891), 931-935, doi:10.1126/science.1160495.
- Angelopoulos, V. (2008b), The THEMIS Mission, *Space Sci. Rev.*, 141, 4-34.
- Angelopoulos, V., et al. (2009), Response to comment on “Tail reconnection triggering substorm onset,” *Science*, 324(5933), 1391-c., doi:10.1126/science.1168045.
- Baumjohann, W., and R. Treumann (1997), *Basic Space Plasma Physics*, Imperial College Press, London.
- Baumjohann, W., and K. H. Glassmeier (1984), The transient response mechanism and pi2 pulsations at substorm onset - Review and outlook, *Planet. Space Sci.*, 32, 1361.
- Baker, D. N., et al. (1996), Neutral line model of substorms: Past results and present view, *J. Geophys. Res.*, 101(A6), 12975-13010.
- Birkeland, K. (1908), *The Norwegian Polaris Expedition 1902-1903*, vol. 1, sect. 1, Aschhoug, Oslo.
- Birkeland, K. (1913), *The Norwegian Polaris Expedition 1902-1903*, vol. 1, sect. 2, Aschhoug, Oslo.

- Bösinger, T., et al. (1981), Correlation between Pi type magnetic micropulsations, auroras, and equivalent current structures during two isolated substorms, *J. Atmos. Terr. Phys.*, 43(9), 933-945.
- Clauer, C., and R. McPherron (1974), Mapping the Local Time-Universal Time Development of Magnetospheric Substorms Using Mid-Latitude Magnetic Observations, *J. Geophys. Res.*, 79(19), 2811-2820.
- Cowley, S. W. H., (1993) The Magnetosphere and Its Interactions with the Solar Wind and with the Ionosphere, in *The Behaviour of Systems in the Space Environment* (eds R. N. DeWitt, D. Dustin, A. K. Hyder), Springer, Netherlands, 245, 147-181.
- Cowley, S. W. H. (2013) Magnetosphere-Ionosphere Interactions: A Tutorial Review, in *Magnetospheric Current Systems* (eds S.-I. Ohtani, R. Fujii, M. Hesse and R. L. Lysak), American Geophysical Union, Washington, D. C.. doi: 10.1029/GM118p0091.
- Cummings, W., J. Barfield, and P. Coleman Jr. (1968), Magnetospheric Substorms Observed at the Synchronous Orbit, *J. Geophys. Res.*, 73(21), 6687-6698.
- Dungey, J. W. (1961), Interplanetary magnetic field and the auroral zones, *Phys. Rev. Lett.*, 47-48.
- Fukushima, N. (1969), Equivalence in ground geomagnetic effect of Chapman-Vestine's and Birkeland-Alfvén current systems for polar magnetic storms, *Rep. Ionos. Space Res. Jap*, 23, 219-227.
- Gosling, J. T., R. T. Hansen, and S. J. Bame (1971), Solar wind speed distributions: 1962–1970, *J. Geophys. Res.*, 76(7), 1811–1815, doi:10.1029/JA076i007p01811.
- Heppner, J. P. (1958), A study of the relationships between the aurora borealis and the geomagnetic disturbances caused by electric currents in the ionosphere, DR135, Defence Research Board of Canada, Ottawa, Ontario, Canada.
- Huba, J. D., N. T. Gladd, and K. Papadopoulos (1977), The lower-hybrid-drift instability as a source of anomalous resistivity for magnetic field line reconnection, *Geophys. Res. Lett.*, 4(3), 125-128.

- Iijima, T., and T. A. Potemra (1976), The amplitude distribution of field-aligned currents at northern high latitudes observed by Triad, *J. Geophys. Res.*, 81(13), 2165–2174, doi:10.1029/JA081i013p02165.
- Iijima, T., and T. Potemra (1978), Large-Scale Characteristics of Field-Aligned Currents Associated with Substorms, *J. Geophys. Res.*, 83(A2), 599-615.
- Iijima, T. (2013) Field-Aligned Currents in Geospace: Substance and Significance, in *Magnetospheric Current Systems* (eds S.-I. Ohtani, R. Fujii, M. Hesse and R. L. Lysak), American Geophysical Union, Washington, D. C.. doi: 10.1029/GM118p0107.
- Jacobs, J. A., et al. (1964), Classification of Geomagnetic Micropulsations, *J. Geophys. Res.*, 69(1), 180-181.
- Kepko, L., and M. G. Kivelson (1999), Generation of Pi2 pulsations by bursty bulk flows, *J. Geophys. Res.*, 104, 25021-25034.
- Kivelson, M. G., and C. T. Russell (1995), *Introduction to Space Physics*, Cambridge University Press, Cambridge.
- Lee, E. A., I. R. Mann, T. Loto'aniu, and Z. C. Dent (2007), Global Pc5 pulsations observed at unusually low L during the great magnetic storm of 24 March 1991, *J. Geophys. Res.*, 112, A05208, doi:10.1029/2006JA011872.
- Lu, G., A. D. Richmond, B. A. Emery, and R. G. Roble (1995), Magnetosphere-ionosphere-thermosphere coupling: Effect of neutral winds on energy transfer and field-aligned current, *J. Geophys. Res.*, 100(A10), 19643–19659, doi:10.1029/95JA00766.
- Lui, A., C.-L. Chang, A. Mankofsky, H.-K. Wong, and D. Winske (1991), A Cross-Field Current Instability for Substorm Expansions, *J. Geophys. Res.*, 96(A7), 11389-11401.
- Lui, A. T. Y. (1996), Current disruption in the Earth's magnetosphere: Observations and models, *J. Geophys. Res.*, 101, 13067-13088.

- Lui, A. T. Y. (2009), Comment on “Tail Reconnection Triggering Substorm Onset”, *Science*, 324(5993), doi:10.1126/science.1167726.
- Mann, I. R. et al. (2002), Coordinated ground-based and cluster observations of large amplitude global magnetospheric oscillations during a fast solar wind speed interval, *Ann. Geophys.*, 20, 4, 405-426.
- McPherron, R., G. Parks, F. Coroniti, and S. Ward (1968), Studies of the Magnetospheric Substorm, 2, Correlated Magnetic Micropulsations and Electron Precipitation Occurring during Auroral Substorms, *J. Geophys. Res.*, 73(5), 1697-1713.
- McPherron, R. (1970), Growth Phase of Magnetospheric Substorms, *J. Geophys. Res.*, 75(28), 5592-5599.
- McPherron, R. L., C. T. Russell, and M. P. Aubry (1973), Satellite studies of magnetospheric substorms on August 15, 1968: 9. Phenomenological model for substorms, *J. Geophys. Res.*, 78(16), 3131–3149, doi:10.1029/JA078i016p03131.
- McPherron, R. L. (1979), Magnetospheric Substorms, *Rev. Geophys. Space Phys.*, 17, 657-681.
- McPherron, R. L. (2013), Geomagnetic Field, *Encyclopædia Britannica*. Encyclopædia Britannica Online Academic Edition. Encyclopædia Britannica Inc.
- Milling, D. K., et al. (2008), Ionospheric localisation and expansion of long-period Pi1 pulsations at substorm onset, *Geophys. Res. Lett.*, 35(L17S20).
- Murphy, K. R. (2008), Ultra Low Frequency Waves and their Association with Magnetic Substorm and Expansion Phase onset, M.S. Thesis, Univ. of Alberta, Edmonton, Canada.
- Murphy, K. R., et al. (2009), Wavelet-based ULF wave diagnosis of substorm expansion phase onset, *J. Geophys. Res.*, 114, A00C16, doi:10.1029/2008JA013548.
- Murphy, K. R., et al. (2011), The dependence of Pi2 waveforms on periodic velocity enhancements within bursty bulk flows, *Ann. Geophys.*, doi:10.5194/angeo-29-493-2011.

- Nagai, T. (1982), Observed Magnetic Substorm Signatures at Synchronous Altitude, *J. Geophys. Res.*, 87(A6), 4405–4417.
- Nishimura, Y., L. Lyons, S. Zou, V. Angelopoulos, and S. Mende (2010), Substorm triggering by new plasma intrusion: THEMIS all-sky imager observations, *J. Geophys. Res.*, 115, A07222, doi:10.1029/2009JA015166.
- Olson, J. V. (1999), Pi2 pulsations and substorm onsets: A review, *J. Geophys. Res.*, 104(A8), 17499–17520, doi:10.1029/1999JA900086.
- Posch, J. L., et al. (2007), Statistical observations of spatial characteristics of Pi1B pulsations, *J. Atmos. Terr. Phys.*, 69(15), 1775-1796.
- Rae, I. J., et al. (2005), Evolution and characteristics of global Pc5 ULF waves during a high solar wind speed interval, *J. Geophys. Res.*, 110(A12211).
- Rae, I. J., et al. (2009), Near-Earth Initiation of a Terrestrial Substorm, *J. Geophys. Res.*, doi:10.1029/2008JA013771.
- Ratcliffe, J. A. (1972). *An Introduction to Ionosphere and Magnetosphere*. Cambridge University Press.
- Rostoker, G. (1968), Macrostructure of Geomagnetic Bays, *J. Geophys. Res.*, 73(13), 4217-4229.
- Rostoker, G., J. Armstrong, and A. Zmuda (1975), Field-Aligned Current Flow Associated With Intrusion of the Substorm-Intensified Westward Electrojet Into the Evening Sector, *J. Geophys. Res.*, 80(25), 3571-3579.
- Roux, A., et al. (1991), Plasma sheet instability related to the westward travelling surge, *J. Geophys. Res.*, 96, 17697-17714.
- Samson, J. C., R. Rankin, and V. T. Tikhonchuk (2003), Optical signatures of auroral arcs produced by field line resonances: comparison with satellite observations and modeling, *Annales Geophysicae*, 21, 933-945.
- Schunk, R. W. (2013) Ionospheric Outflow, in *Sun-Earth Plasma Connections* (eds J. L. Burch, R. L. Carovillano and S. K. Antiochos), American Geophysical Union, Washington, D. C.. doi: 10.1029/GM109p0195.

- Shiokawa, K., W. Baumjohann, and G. Haerendel (1997), Braking of high-speed flows in the near-Earth tail, *Geophys. Res. Lett.*, 24(10), 1179–1182.
- Smith, A. J., et al. (2002), VLF, magnetic bay, and Pi2 substorm signatures at auroral and midlatitude ground stations, *J. Geophys. Res.*, 107(A12).
- Strangeway, R. J. (2013) The Relationship Between Magnetospheric Processes and Auroral Field-Aligned Current Morphology, in *Auroral Phenomenology and Magnetospheric Processes: Earth And Other Planets* (eds A. Keiling, E. Donovan, F. Bagenal and T. Karlsson), American Geophysical Union, Washington, D. C.. doi: 10.1029/2012GM001211.
- Sugiura, M. (1984), A fundamental magnetosphere-Ionosphere coupling mode involving field-aligned currents as deduced from DE-2 observations. *Geophys. Res. Lett.*, 11: 877–880. doi: 10.1029/GL011i009p00877.
- Takahashi, K., et al. (2010), Multipoint observation of fast mode waves trapped in the dayside plasmasphere, *J. Geophys. Res.*, 115, A12247, doi:10.1029/2010JA015956.
- Vasyliunas, V. (1968), A Survey of Low-Energy Electrons in the Evening Sector of the Magnetosphere with OGO 1 and OGO 3, *J. Geophys. Res.*, 73(9), 2839-2884.
- Vasyliunas, V. M. (1970), Mathematical models of magnetospheric convection and its coupling to the ionosphere, *Particles and Fields in the Magnetosphere*, edited by B. M. McCormac, D. Reidel Publ. Co., Norwell, Mass., 60.
- Waters, C. L., B. J. Anderson, and K. Liou (2001), Estimation of global field aligned currents using the iridium® System magnetometer data, *Geophys. Res. Lett.*, 28(11), 2165–2168.
- Watt, C.E.J. and Rankin, R. (2012) Alfvén Wave Acceleration of Auroral Electrons in Warm Magnetospheric Plasma, in *Auroral Phenomenology and Magnetospheric Processes: Earth And Other Planets* (eds A. Keiling, E. Donovan, F. Bagenal and T. Karlsson), American Geophysical Union, Washington, D. C.. doi: 10.1029/2011GM001171.

Winningham, J. D. and C. Gurgiolo (1982), DE-2 photoelectron measurements consistent with a large scale parallel electric field over the polarcap, *Geophys. Res. Lett.*, 9, 977.

# Chapter 2 On the nature of ULF wave power during nightside auroral activations and substorms: Spatial Distribution<sup>1</sup>

## 2.1 Introduction

Impulsive Ultra Low Frequency (ULF) waves, referred to as Pi pulsations, have been shown to be an integral part of the substorm expansion phase onset. These pulsations have been associated with both upper atmospheric signatures associated with auroral phenomena and disturbances of the Earth's magnetic field in the nightside magnetosphere [Heppner, 1958; Akasofu, 1964]. Historically, Pi pulsations were divided by Jacobs et al. [1964] into two wavebands: the Pi1 waveband with periods of 1-40 s and the Pi2 waveband with periods of 40-150 s. Jacobs et al. [1964] described Pi2 pulsations as the dominant Pi waveform observed during substorms, while Pi1 waves were reported to have smaller amplitudes, compared to the longer period Pi2 waves, and rarely had periods exceeding ~20 s. Though both Pi1 and Pi2 pulsations are observed during substorm expansion phase onset, it is typically the Pi2 waveband that is primarily used to characterise substorms and thus has been extensively studied whilst Pi1 pulsations have traditionally received less consideration. Typically Pi2 pulsations are associated with the initial plasma sheet disturbance during substorm expansion phase onset and the subsequent formation of the substorm current wedge (SCW) in the ionosphere [e.g., Olson, 1999 and references therein]. However, it has also been postulated that Pi2 pulsations can be directly driven by large amplitude plasma flows in the magnetotail [Kepko et al., 1999] or indirectly driven by the same processes which drive the plasma flows [Murphy et al., in review]. Alternatively, Pi waves may also be the manifestation of field line resonances [Rae et al., 2006], or related to cavity modes [Olson, 1999 and references therein] or waveguide modes [Wright and Mann, 2006 and references therein] in the nightside magnetosphere.

Heacock [1967] adopted a similar classification scheme to Jacobs et al. [1964]; though he subcategorised Pi waves into continuous pulsations, PiC, and broadband pulsations,

---

<sup>1</sup> A version of this chapter has been accepted for publication. Murphy, K. R. et al. (2011), *J. Geophys. Res.*, 116, A00I21, doi:10.1029/2010JA015757.

PiB. The PiC pulsations described by Heacock [1967] were quasi-monochromatic waves associated with the auroral electrojets and the formation of magnetic bays during substorms, and therefore are similar to the Pi2 pulsations categorised by Jacobs et al. [1964]. PiB pulsations are typically observed in the midnight sector near the onset of a magnetic bay or substorm [Heacock, 1967]. Similar to Pi2 pulsations, the PiB pulsations have been the most extensively studied pulsation in the Heacock classification scheme. Arnoldy et al. [1987] found that PiB pulsations are highly correlated with particle precipitation and auroral fluctuations; these authors suggested that PiB pulsations were likely driven by the stepwise motion of the westward electrojet during substorm expansion phase onset. Lysak [1988] showed that PiB pulsations could be excited by current carrying Alfvén waves trapped in a resonant cavity formed by the inhomogeneity of the Alfvén speed at low altitudes in the ionosphere. In the model proposed by Lysak [1988], PiB pulsations could be driven whenever a strong field aligned current is present and indeed may be driven by the formation of the SCW during substorm expansion phase onset.

More recently, through the combination of an increased number of observations and a better understanding of the physics driving ULF wave pulsations observed during substorm expansion phase onset, the classification scheme of Pi pulsations has become increasingly more complex. For instance, short period and broadband ULF waves have been classified as Pi1B waves [Bösinger and Yahnin, 1987; Lessard et al., 2006; Posch et al., 2007] while long-period Pi1/short-period Pi2 waves with periods of ~24-96 s have recently been termed Pi1-2 waves [Rae et al., 2010a]. The short-period broadband Pi1B pulsations are typically excellent indicators of substorm onset [Bösinger and Yahnin, 1987] having been shown to develop conjugate to and contemporaneously with the global auroral intensification during substorm expansion phase onset [Posch et al., 2007]. Additionally, using conjugate spacecraft and ground-based observations, Lessard et al. [2006] demonstrated that Pi1B pulsations could be observed both on the ground and at geosynchronous orbit during substorm onset. At higher altitudes these authors showed that Pi1B pulsations observed after onset were largely compressional in nature, while at lower altitudes the pulsations were dominantly shear waves suggesting that the waves undergo mode conversion as they propagate toward the ionosphere. While not

fully understood, it is evident that Pi1B pulsations are intimately connected to the process or processes leading to and surrounding substorm expansion phase onset.

Though not specifically classified as Pi1-2 waves, long-period Pi1/short-period Pi2 pulsations were initially observed in space in conjunction with substorm expansion phase onset by Maynard et al. [1996]. During the expansion phase onset these authors observed signatures of drift waves in the nightside magnetosphere which developed a significant amount of parallel Poyting flux in the 30-100 s ULF wave period band. Maynard et al. [1996] suggested that the constructive interference of these drift waves was capable of initiating a magnetic substorm, whilst destructive interference initiated a pseudo-breakup. More recently Murphy et al. [2009a] demonstrated that ULF waves in the 24-96 s period band, referred to as Pi1-2 waves, were the first observable magnetic signature on the ground and are spatially conjugate to and occur prior to the global-scale auroral brightening of the aurora during magnetic substorms. Rae et al. [2009a; 2009b] further demonstrated that ULF pulsations in the 24-96s waveband occurred simultaneous to and conjugate with small scale auroral beads [Rae et al., 2009a] and fluctuations [Rae et al., 2009b] which developed prior to the poleward and westward expansion of the aurora during substorm expansion phase onset [Rae et al., 2009a] and as well during pseudo-breakups [Rae et al., 2009b]. These authors suggest that Pi1-2 waves play a fundamental role in the development and onset of a magnetic substorm and are likely the consequence of a near-Earth plasma instability resulting in the initiation of the auroral substorm expansion phase onset [Rae et al., 2009a; Rae et al., 2010a]. Obviously there are several ULF wavebands of interest observed during substorm expansion phase onset. In this study we seek to determine whether there are any statistical differences between the long period Pi1 (10-40 s), Pi1-2 (24-96 s) and Pi2 (40-150 s) waves observed during magnetic substorms and nightside auroral activations.

In this paper we present a detailed statistical study of the two dimensional distribution of the polarisation and power spectrum of ULF waves in the Pi1, Pi1-2 and Pi2 wave bands during substorm expansion phase onset with respect to substorm onset times and locations identified using the IMAGE satellite [Frey et al., 2004; Frey and Mende, 2006]. In a companion paper Rae et al. [2010b; this issue referred to as Paper 2] present a detailed superposed epoch analysis of the temporal evolution of ULF wave power in the

Pi1 (12-48 s), Pi1-2 and Pi2 wavebands during the substorm expansion phase onset as identified by Nishimura et al. [2010]. In their paper, Rae et al. [2010b] found that all three ULF wavebands underwent a similar relative increase in power during onset, suggesting that the temporal variation of all three bands during substorm and nightside activations is similar. By statistically characterising the two-dimensional spatial distribution of ULF wave power and polarisation as well as the evolution of ULF wave power (Paper 2) with respect to substorm onset times and locations, we seek to determine if the different bands of ULF waves possess statistically disparate characteristics. In particular we seek to determine if any differences exist between longer period Pi1 (10-40s) waves and Pi1-2 waves typically thought to characterise the spatial and temporal onset of substorm expansion phase onset and Pi2 pulsations generally associated with the formation of the substorm current wedge, bursty bulk flows and resonances in the nightside magnetosphere.

## **2.2 Methodology**

### **2.2.1 Data Sets**

This study utilises magnetic field data from 17 ground-based magnetometer stations from both the CARISMA [Canadian Array for Realtime Investigation of Magnetic Activity, Mann et al., 2008] and CANMOS (Canadian Magnetic Observatory System) magnetometer arrays over a five year period between May 2000-Dec 2005, together with the IMAGE auroral substorm onsets identified in the Frey substorm database [Frey et al., 2004; Frey and Mende, 2006], to statistically characterise the ULF wave power and polarisation parameters during substorm expansion phase onset. Both the CARISMA and CANMOS magnetometer arrays utilise three-axis fluxgate magnetometers to measure the geographic North-South (X-component), East-West (Y-component) and vertical magnetic fields at either one or five second cadence. Prior to 1st April 2005 the CARISMA magnetometer array was operated as CANOPUS [Canadian Auroral Network for the OPEN Program Unified Study magnetometer array, Rostoker et al., 1995] during which data was recorded at 8 Hz (0.125 s) and down-sampled and stored at a five second cadence due to bandwidth limitations. In the CARISMA era data is sampled at 8 Hz and down-sampled to a 1 s cadence and both the 8 Hz and 1 s data are stored. Similar to the CARISMA array, the CANMOS magnetometer array samples at 8 Hz and is

down-sampled and recorded at a one second cadence. In this statistical study we utilise both 5 s CANOPUS data and the 1 s CARISMA and CANMOS data. The corrected geomagnetic (CGM) and geographic locations of the CARISMA and CANMOS magnetometer stations employed in this study are shown in Tables 1 and 2, respectively, for the year 2003, the center of the time interval encompassing the Frey substorm database.

Table 2.1: CARISMA Stations

Station	Geographic		Geomagnetic		
	Latitude	Longitude	Latitude	Longitude	L-Shell
<b>CONT</b>	65.8	248.8	73.1	303.5	12.0
<b>DAWS</b>	64.1	220.9	66.0	272.8	6.1
<b>RANK</b>	62.8	267.9	72.6	335.1	11.3
<b>FSIM</b>	61.8	238.8	67.4	293.2	6.9
<b>FCHU</b>	58.8	265.9	68.7	332.6	7.7
<b>RABB</b>	58.2	256.3	67.1	318.1	6.7
<b>MCMU</b>	56.7	248.8	64.4	308.2	5.5
<b>GILL</b>	56.4	265.4	66.4	332.3	6.3
<b>ISLL</b>	53.8	265.3	63.9	332.5	5.2
<b>PINA</b>	50.2	264.0	60.3	331.0	4.1

Table 2.2: CANMOS Stations

Station	Geographic		Geomagnetic		
	Latitude	Longitude	Latitude	Longitude	L-shell
<b>CBB</b>	69.1	255.0	77.0	309.8	NA
<b>BLC</b>	64.3	264.0	73.7	328.0	12.8
<b>YKC</b>	62.5	245.5	69.4	301.1	8.2
<b>SNK</b>	56.5	280.8	66.7	356.6	6.5
<b>PBQ</b>	55.3	282.4	65.5	359.0	5.8
<b>MEA</b>	54.6	246.7	62.0	306.3	4.6
<b>OTT</b>	45.4	284.4	55.7	1.1	3.2

Frey et al. [2004; see also, Frey and Mende, 2006] identified the global auroral intensification of substorm onsets in both space and time from auroral images taken by the IMAGE-FUV camera which satisfied the following criteria: (1) a clear and localised brightening of the auroral oval, (2) the auroral brightening must expand to the poleward

boundary of the oval and expand azimuthally across twenty minutes of local time and (3) an auroral brightening was only characterised as a substorm onset if the brightening was separated by a minimum of thirty minutes from any prior onset. The substorm onset time was subsequently defined as the initial IMAGE-FUV frame depicting a clear brightening of the aurora and the geographic and geomagnetic onset location (in latitude and longitude) were defined by the location of the brightest pixel in the IMAGE-FUV onset frame. The IMAGE-FUV camera utilises two imagers, the Wideband Imaging Camera (WIC) and the Spectrographic Imager (SI-13), to observe the aurora for 5-10 s during every 2 minutes spin period. At apogee the WIC instrument offers the best spatial resolution with a pixel size of approximately  $\sim 50 \times 50 \text{ km}^2$  while the pixel size of the SI-13 instrument is  $\sim 100 \times 100 \text{ km}^2$  [Frey et al., 2004]. The temporal resolution of the IMAGE-FUV instrument and spatial resolution of the SI-13 imager hence give upper estimates for the error in the auroral onset location and time identified by Frey et al. [2004] and Frey and Mende [2006]. In latitude and longitude the error in the onset location corresponds to  $\sim 1^\circ$  and  $\sim 2^\circ$ , respectively, at an auroral latitude of  $66^\circ$  and to an error of up to approximately 2 minutes in time. It is important to note that due to tracking errors, the IMAGE-FUV instrument can at certain times lose sight of the aurora oval. Thus for some of the substorms identified in the Frey substorm database the accuracy in the onset time of identifying auroral intensifications can be of the order of tens of minutes as demonstrated by Murphy et al. [2009; see also Liou and Zhang 2009 and Murphy et al., 2009b]. The Frey substorm database identifies over 4000 substorms observed by the IMAGE-FUV camera between 16th May 2000 and 18th December 2005, subsequent to which communications between the satellite and ground-based operations were lost.

In this study we restrict the Frey substorm database to a subset of substorms conjugate to the CARISMA and CANMOS magnetometer arrays and conduct a superposed epoch analysis. Conjugate substorms are identified as substorms observed in the northern hemisphere lying between  $220^\circ$ - $310^\circ$  geographic longitude and occurring close to the midnight meridian (between 22-2 MLT). A total of 885 substorms satisfy this criteria, and span the interval 20th May 2000 – 12th December 2005. The geographical onset locations of the 885 conjugate substorms from the Frey substorm database used in this study are illustrated in Figure 2.1 (purple asterisks) along with the location of the

CARISMA (red triangles) and CANMOS (red squares) magnetometer stations (c.f., Table 2.1 and Table 2.2, respectively).

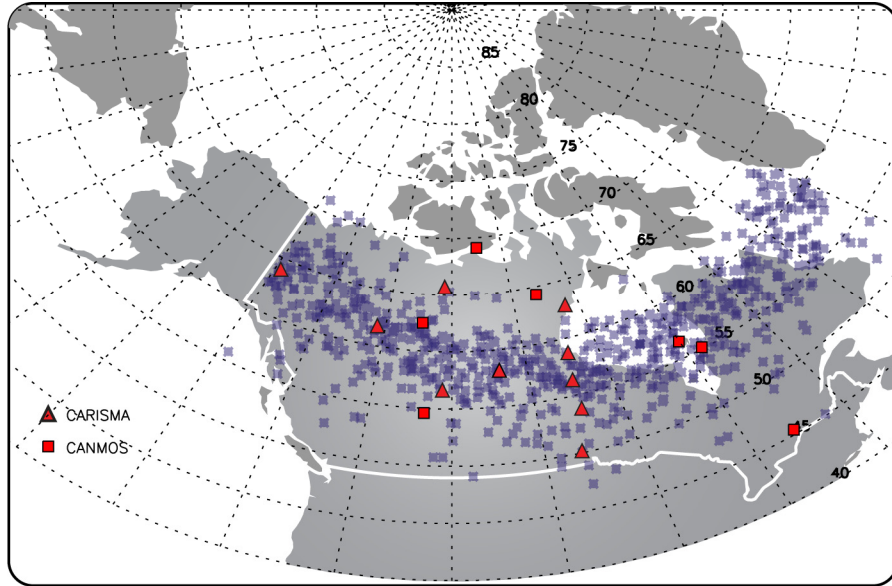


Figure 2.1: The locations of 885 substorms (purple asterisk) identified in the Frey substorm database conjugate to the CARISMA (red triangles) and CANMOS (red squares) magnetometer stations.

## 2.2.2 Data Processing

A statistical study characterising the power and polarisation parameters of ULF waves is most effectively done in the spectral domain. Hence, we utilise the Fast Fourier Transform (FFT) to estimate the power spectra as well as the angle of azimuth and ellipticity of ULF waves in the long period Pi1 (10-40s), Pi1-2 (24-96s) and Pi2 (40-150s) wave bands during substorm expansion phase onset as described below. It is important to note that we must restrict the Pi1 ULF wave band to the 10-40s period band rather than the historical 1-40s period band [Jacobs et al., 1964] out of necessity given that a subset of the dataset has a 5 s cadence. As such, for the remainder of this manuscript we refer to the Pi1 band studied herein as the Pi1\* band to clearly differentiate between the historical 1-40 s waveband and the 10-40 s waveband studied herein.

Recent work has clearly demonstrated that ULF waves and the aurora are intimately connected during substorm expansion phase onset, the onset of both phenomena being closely conjugate in both space and time [Murphy et al., 2009a; Murphy et al., 2009b; Rae et al., 2009a; Rae et al., 2009b; Rae et al., 2010a; Rae et al. 2010b]. As such the

onset times identified in the Frey substorm database provide an excellent epoch time with which to statistically characterise ULF pulsations during the substorm expansion phase. It is important to note however that the onsets identified in the Frey substorm database are global auroral intensifications and can at times occur several minutes following the onset of ULF waves during any particular substorm [Murphy et al., 2009a]. In order to account for any potential time lag between the onset of ULF waves and the auroral intensifications or any data gaps surrounding auroral onsets identified by Frey et al. [2004] and Frey and Mende [2006] we analyze a 40 minute time-series centered on the Frey onset time. Prior to calculating the ULF wave power spectrum, the magnetic field data from all magnetometers are transformed from geographic coordinates (X, Y, Z; geographic north-south, east-west, and vertical) to corrected geomagnetic coordinates (H, D, Z; geomagnetic north-south, east-west, and vertical). The mean was then removed from the H and D time series and the data were highpass filtered at 500 s using Lanczos squared zero-phase 300 point and 1500 point filters for the 5 and 1 second time-series, respectively, to remove the slowly varying background perturbation of the magnetic field as well as any bays or longer period magnetic field variations resulting from the formation of the substorm current wedge in the ionosphere. A Hanning window was then applied to the 40 minute H- and D-component time series and the resulting signal is transformed into the spectral domain using the FFT. Finally the power (or power spectral density, PSD) was calculated as described by Press et al. [1992] with the appropriate Hanning window correction applied. Note that if the magnetic bay variations contain frequency components which lie in any of the Pi2, Pi1-2, or Pi1\* bands then these will also be captured in the bandpassed time series in addition to the ULF waveforms. Since the Pi1\* band contains ULF waveforms with the smallest amplitudes, this band might be most susceptible to these effects especially for sharp bays.

Any magnetometer time series with a data gap or erroneous values were discarded. Note that the fluxgate magnetometers have an amplitude resolution of 1/40 nT. As such any of the power estimates for any of the three ULF wavebands that do not have an amplitude peak whose root mean squared amplitude is larger than twice the amplitude resolution of the magnetometers (2/40 nT) is not considered in the statistics. This thresholding ensures that this statistical database includes only those events with

waveforms in each of the three ULF wave bands with amplitudes larger than the amplitude resolution of the magnetometers.

The polarisation parameters are calculated from a 40 minute H and D time-series centered on the Frey auroral onset time similar to the time series used to quantify PSD. However, rather than utilising a single highpass filtered series, three bandpass series are used to quantify the angle of azimuth and ellipticity in each of the three ULF wave bands observed during substorm expansion phase onset (Pi1\*, Pi1-2 and Pi2). For each conjugate substorm three bandpassed time-series are constructed from each available magnetometer in both the H and D magnetic field components again using a Lanczos squared zero-phase filter. The three bandpasses utilised, and the number of points constructing each bandpass filter for the 5 and 1 s time-series are: the Pi1\* band (10-40 s, 12 and 60 points) the Pi1-2 band (24-96s, 57 and 289 points) and the Pi1-2 band (40-150 s, 45 and 225 points). A Hanning window is then applied to the time series which are then transformed from the time domain to the frequency domain and the azimuth angle and ellipticity in the horizontal plane are calculated from the transformed H and D signals and the H-D coherency matrix as described in Fowler et al. [1967 equation 1; see also Arthur et al., 1976 equations 1, 4 and 5]. In the coordinate system used herein, the angle of azimuth represents the angle between the major axis of the polarisation ellipse in the H-D plane relative to the H-axis and has a range between  $[-\pi/2, \pi/2]$ . The ellipticity defines the ratio of the minor axis to the major axis of the polarisation ellipse in the H-D plane as well as the handedness of the ellipse; right-handed or clockwise if the ellipticity is greater than zero and left-handed or counter clockwise if the ellipticity is less than zero.

It is important to note that Fowler et al. [1967] describe a method for the calculation of the polarisation parameters in the time domain for a time-averaged quasi-monochromatic two-component vector. However, as mentioned above the frequency domain is better suited for a statistical study than the time domain. Using Parseval's theorem [Press et al., 1992] the method described by Fowler et al. [1967] for a time-averaged quasi-monochromatic two-component vector signal can be performed in the frequency domain rather than the time domain and the time-averaged coherency matrix [c.f., equation 1 Fowler et al., 1967] can be transformed to a smoothed frequency space

coherency matrix. In particular, Parseval's theorem states that the time-averaged amplitude of a signal is equal to twice the sum of the squares of the spectral coefficients over a limited frequency range. In our analysis the summation in the frequency domain is defined in each of the Pi1\*, Pi1-2 and Pi2 wavebands by three points centered on the H-D cross-power peak calculated from the FFT of the H and D time-series. The cross-power peak in each waveband will in general describe the frequency at which a coherent and large amplitude waveform is observed in both the H and D magnetic field components. This is the frequency range over which the polarisation parameters of the wave will be most accurately determined from the methods described by Fowler et al. [1967]. The angle of azimuth and ellipticity for each of the three ULF wave bands is then calculated from the Fourier transform of the H and D time-series and the smoothed H-D coherency matrix. We apply an amplitude threshold to the Fourier transform in each of the three ULF wavebands to remove any signal which has an amplitude smaller than twice the amplitude resolution of the fluxgate magnetometers in a similar manner to that described above to include only resolvable amplitudes and waveforms in the statistics. Note that in this instance the thresholding is applied separately to each of the three bandpassed ULF time-series, Pi1\*, Pi1-2 and Pi2.

We have validated the methodology described herein to determine the azimuth and ellipticity of ULF waves observed at substorm onset by comparing the location of the substorm current wedge (SCW) as inferred by the angle of azimuth of Pi2 waves [c.f., Lester et al., 1983] to the location determined by Milling et al. [2008] during an isolated substorm on 1st November 2006. Milling et al. [2008] determined the location of the SCW by comparing the H and D magnetic bay perturbations to those determined by Cramoysan et al. [1995] for a modeled SCW and as well from the angle of azimuth of Pi2 waves as determined by complex demodulation [Beamish et al., 1979]. The inferred location of the SCW determined from the Pi2 angle of azimuths calculated by the methodology described above is in good agreement (to within error of a single magnetometer station in longitude) with that determined by Milling et al. [2008]. Furthermore the method described in Fowler et al. [1967] has also been previously utilised by Samson et al. [1971] to characterise the polarisation of both nightside and day-side ULF pulsations. In addition, similar methods described by Arthur et al. [1976] have been utilised by Lester et al. [1983; 1984; 1989] to characterise the polarisation of

Pi2 waves observed during substorm expansion phase onset. Note that if there are bays or sharp changes in the background magnetic field which contain power in the frequency bins selected for the polarisation analysis then this may contaminate the calculation of the azimuth and ellipticity. These effects might be expected to be most noticeable in the Pi1\* band, due to its lower power, in cases where the bays are sufficiently sharp. However, in cases where the time variation of the background field is sufficiently slow compared to the period of band of the ULF waves analysed then these effects will be small.

In order to conduct a superposed spatial analysis of ULF wave characteristics the locations of the CARISMA and CANMOS magnetometers during each substorm are binned with respect to their relative distance from the auroral intensification identified by Frey et al. [2004] and Frey and Mende [2006] in geomagnetic degrees of latitude and longitude. The distance away from onset was calculated as the station geomagnetic latitude (longitude) minus the onset geomagnetic latitude (longitude) referred to as delta latitude,  $\Delta lat$  (delta longitude,  $\Delta long$ ). A negative (positive) difference in geomagnetic latitude indicates that the station was south (north) of the auroral intensifications and a negative (positive) difference in geomagnetic longitude implies that the station was west (east) of the auroral intensification. The two-dimensional spatial distribution of stations with valid data with respect to distance in CGM latitude and longitude away from auroral onset is shown in Figure 2.2, where colour indicates the total number of events with valid magnetometer data within the spatial bin for each of the three ULF wave bands. The latitude bins span  $2^\circ$  and longitude bins span  $10^\circ$  and the grid of event occurrence is centered with respect to the onset location at  $\Delta lat = 0$ ,  $\Delta long = 0$ . The most dense distribution in each of the three ULF wavebands is located within approximately  $45^\circ$  west ( $\Delta long = -45^\circ$ ) and  $35^\circ$  east ( $\Delta long = 35^\circ$ ) of the onset location. Latitudinally, Figure 2.2 shows a high concentration of stations with valid data between approximately  $5^\circ$  south of onset and  $9^\circ$  north of onset. Note that in Figure 2.2 both the Pi1-2 and Pi2 wavebands have a large number of occurrence statistics (or valid magnetometer data) whereas the Pi1\* waveband has a significantly fewer number of occurrence statistics. This is because in general the Pi1\* amplitudes are smaller than the Pi1-2 and Pi2 amplitudes and thus fewer events satisfy the threshold criteria described above. This is discussed in more detail in subsequent sections.

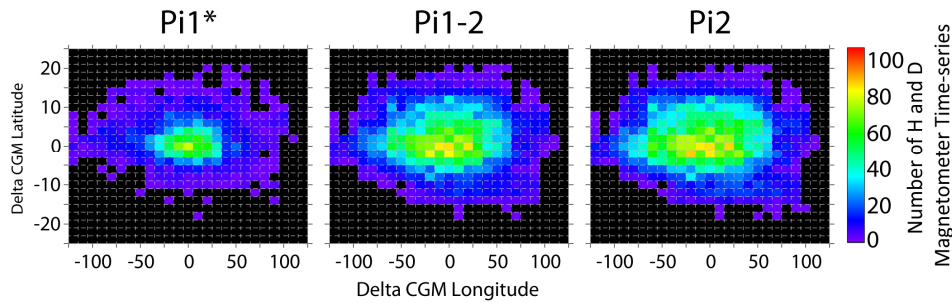


Figure 2.2: The two-dimensional Pi1\*, Pi1-2 and Pi2 waveband distribution of event occurrence with respect to the relative distance in CGM latitude and longitude of an individual station away from auroral onset for any particular substorm. Negative (positive) indicates the station is west/south (east/north) of auroral onset. The color bar indicates the number of magnetometer time-series in each spatial bin utilised to quantify both the ULF wave power and polarisation parameters.

### 2.3 Analysis and Results

Figure 2.3 illustrates the two-dimensional spatial distribution of the log of the median summed power in each of the three ULF wave bands (Pi1\* – left; Pi1-2 – middle; Pi2 – right) as a function of delta latitude and delta longitude (c.f., Figure 2.2) for both the H (top row) and D (middle row) magnetic field components. For each of the spatial bins depicted in Figure 2.2 the median summed power is calculated by summing the power in each of the Pi1\*, Pi1-2 and Pi2 frequency (or period) bands for each magnetometer station within that bin. The median value is then determined in each band in both the H and D magnetic field components and plotted in the corresponding spatial bin. The color in each bin represents the log of the amplitude of the summed ULF wave power; green corresponding to a small power, blue medium and pink high. The bottom row of Figure 2.3 is the two dimensional distribution of the median AE for each the three ULF wavebands. The median AE is determined from the distribution of values of the maximum AE within the 40 minutes centered on the Frey onset location for each of the spatial bins for each of the Pi1\*, P1-2 and Pi2 occurrence distributions (Figure 2.2). Note that because each of the three ULF wavebands have a different occurrence distributions, the AE distribution is not the same across all wavebands. Apparent in Figure 2.3 is a clear localisation of ULF wave power in all three of the ULF wave bands (Pi1\* – left; Pi1-2 – middle; Pi2 – right) near the region of global auroral onset in both the H and D magnetic field components (top and bottom rows respectively). Moving away from the auroral onset location, the median summed power in each ULF wave

band in both H and D decreases by approximately an order of magnitude in both the latitudinal and longitudinal directions within  $\sim 35^\circ$  of longitude and  $\sim 9^\circ$  of latitude from the origin. Additionally there is a clear increase in the median summed power as the period of the ULF wave band increases. That is, the power of the median summed power is smallest in the Pi1\* wave band and largest in the Pi2 wave band, the Pi1-2 wave band lying between the Pi1\* and Pi2 bands. This is observed in both the H- and D-components. Figure 2.3 also illustrates that in general the amplitude of the summed ULF wave power is larger in the H-component than in the D-component and as such extends further in both latitude and longitude.

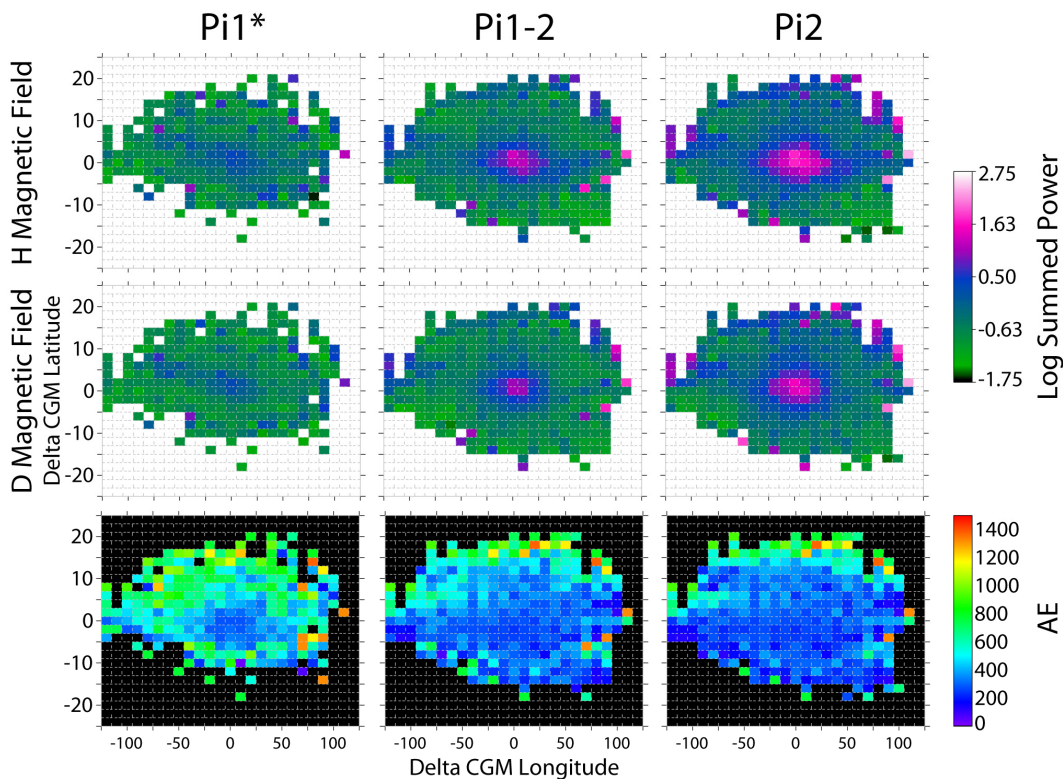


Figure 2.3: The two-dimensional spatial distribution of the logged median summed ULF wave power and median AE with respect to the location of auroral onset, c.f., Figure 2. Top row is the H-component ULF wave power middle row the D-component wave power and bottom the median AE for the respective event distributions. The left column is the summed Pi1\* power, middle the summed Pi1-2 power and right the summed Pi2 power. The color bar denotes the log of the median summed power where the median summed power is in units of  $\text{nT}^2/\text{mHz}$ .

It is also important to note the distribution of AE with regard to each of the three ULF wavebands. Near the auroral onset location ( $|\Delta lat| \lesssim \pm 3^\circ$  and  $|\Delta long| \lesssim \pm 15^\circ$ ) the three ULF wave bands have a similar distribution of AE values around  $\sim 300$  nT.

However, further away from the auroral onset location ( $|\Delta lat| \gtrsim \pm 3^\circ$  and  $|\Delta long| \gtrsim \pm 15^\circ$ ) there is a distinct difference between the distribution of the median AE for the Pi1\* waveband and those of the Pi1-2 and Pi2 wavebands. In this region the median AE of the Pi1\* occurrence distribution dramatically increases to values of  $>600$  nT whereas the Pi1-2 and Pi2 AE values are similar to those near the auroral onset location. Note at the very edge of the occurrence distribution of the Pi1-2 and Pi2 wavebands the AE distributions the median AE is larger than those near the center of the distribution suggesting that even larger events are required for Pi waves to be observed this far from the onset region although this may partly result from limited count statistics in this region.

Figure 2.4 illustrates the mean of the summed power in the H- and D-components in the Pi1\*, Pi1-2 and Pi2 wave bands as well the two-dimensional distribution of the mean AE in the same format as Figure 2.3. The mean summed power is very similar to the median summed power. The largest ULF wave power is observed near the global auroral intensification (at the origin) and quickly decays as the distance from the origin increases in both H and D and in each of the three ULF wave bands. Additionally, the mean summed ULF wave power is again larger in the H-component as compared to the D-component. However in general the mean summed power is larger than that of the median. Moreover the mean distribution shows a clear expansion of ULF wave power west of the auroral onset (as far as  $\Delta long \cong -100^\circ$ ) in each of the ULF wave bands and in both the H- and D- magnetic field components. This can be compared to the median summed spectra in Figure 2.3 where ULF wave power is concentrated near the global auroral intensification. Similar to the median AE distribution for the Pi1\* occurrence statistics (bottom row Figure 2.2) the mean AE distribution in the Pi1\* waveband shows a localisation of smaller AE values near auroral onset ( $\sim 300$  nT) and larger values further away from the onset region ( $> 600$  nT). Also similar to the median AE distributions, the mean AE distributions of the Pi1-2 and Pi2 occurrence statistics have a more consistent distribution, only at the very edges of the occurrence distribution does the mean AE value differ from that near the auroral onset location.

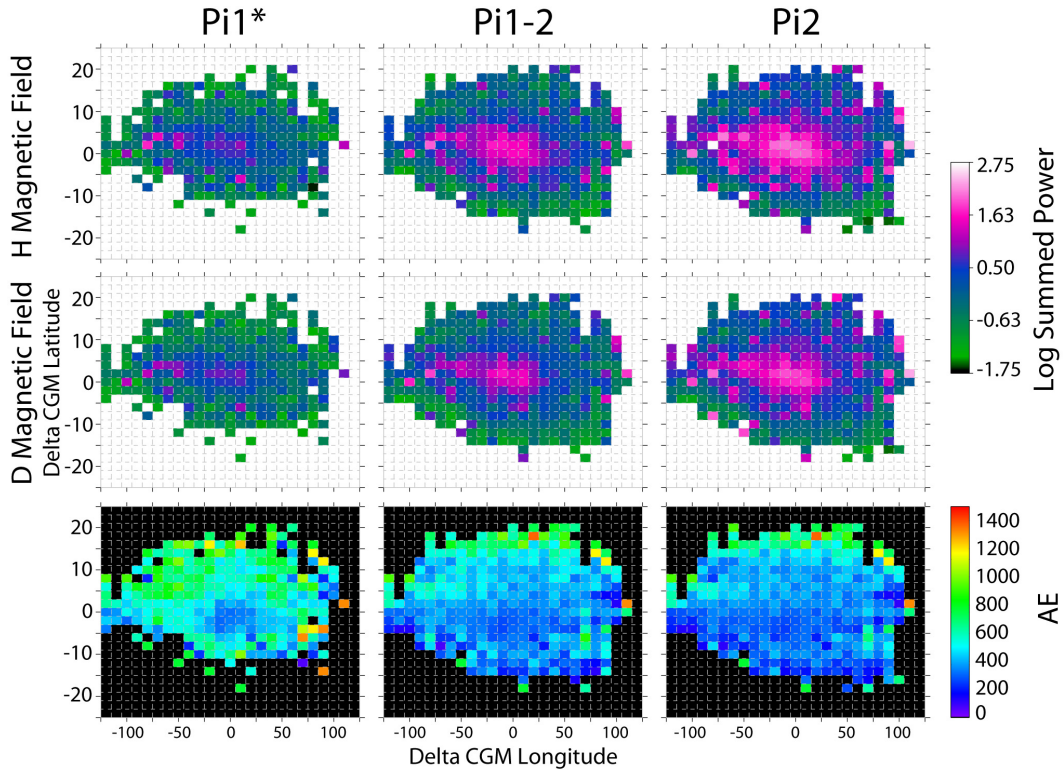


Figure 2.4: The two-dimensional spatial distribution of the logged mean summed ULF wave power and mean AE with respect to the location of auroral onset. The figure is organised in the same format as Figure 3. Top middle and bottom rows are the H-component power, D-component power and mean AE respectively. The left, middle and right columns are the mean summed ULF wave power in the Pi1\*, Pi1-2 and Pi2 wavebands, respectively. The color bar denotes the log of the mean summed ULF wave power where the summed power is in units of  $nT^2/mHz$ .

The 2-D power distributions illustrated in Figure 2.3 and Figure 2.4 show that the amplitude of ULF wave power varies as function of magnetic field component, ULF wave band and distance from the auroral onset location. By characterising the longitudinal and latitudinal decay scales of ULF wave power we are able to quantify the dependence of ULF wave amplitude as a function of distance away from onset for each magnetic field component. Note that we use the Pi1\* occurrence distribution (c.f., Figure 2.2) to determine the two dimensional distribution of ULF wave power (c.f., Figure 2.3 and Figure 2.4) in each of the three ULF wave bands and restrict the analysis to the region surrounding substorm onset where the distribution of AE is nearly constant. This allows a direct comparison of the decay scales between the three ULF wave bands and ensures that the decay scales are determined from a subset of substorm events with similar AE.

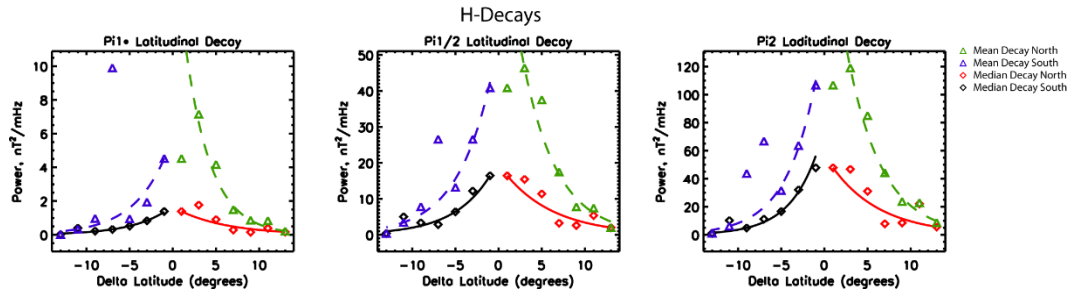


Figure 2.5: The latitudinal decay of the mean and median summed H-component ULF wave power as a function of delta latitude in the Pi1\*, Pi1-2 and Pi2 wavebands (left, middle and right respectively). The y-axis is power ( $nT^2/mHz$ ) and the x-axis delta latitude (negative south and positive north). Green (blue) triangles are the mean north (south) ULF wave power and the green (blue) dashed line is the least absolute deviation fit to the triangles. The red (black) diamonds are the median north (south) ULF wave power and the solid black (red) line is the least absolute deviation fit to the diamonds.

Figure 2.5 shows the spatial decay of the H-component magnetic field as a function of  $\Delta lat$  along the meridian characterising the auroral intensification, defined by  $|\Delta long| < 15$  degrees (and thus spanning three bins in delta longitude). Both the median (diamonds) and mean power (triangles) are shown in Figure 2.5. Note that three longitudinal bins are used to characterise the latitudinal decay of ULF wave power, hence Figure 2.5 plots the average of each of the mean and median summed power over the three delta longitude bins. For each of the Pi1\*, Pi1-2, and Pi2 wave bands the spatial decay scales of the mean summed power in the north and in the south directions (green and blue triangles, respectively) and the decay scales of median summed power in the north and south directions (red and black diamonds, respectively) directions are determined by fitting the power profiles to a function of the form  $(-|\Delta lat|/\lambda_{lat})$  using a least absolute deviation method. The coefficient  $Q$  is a constant and  $\lambda_{lat}$  is the e-folding length, in degrees. We use the least absolute deviation method to characterise the decays scales instead of a minimum Chi-square fit because the least absolute deviation method is less sensitive to variations arising from statistical outliers that may be introduced where the occurrence statistics are small. The latitudinal decay length ( $\lambda_{lat}$ ) for both the H and D magnetic field components and the three ULF spectral bands is summarised in and the respective fits are also plotted in Figure 2.5. Apparent in is that the north and south spatial decay scales of ULF waves in both H and D are very similar and more interestingly there is little difference in the decay scales of Pi1\*, Pi1-2 and Pi2 waves. Also note that Figure 2.5 shows a clear enhancement of ULF wave power north

of auroral onset at  $\Delta lat=3^\circ$ . From the fitted curves it is clear that the north and south spatial decay rates in both the median and mean ULF power are in general very similar, generating a latitudinally symmetric power distribution.

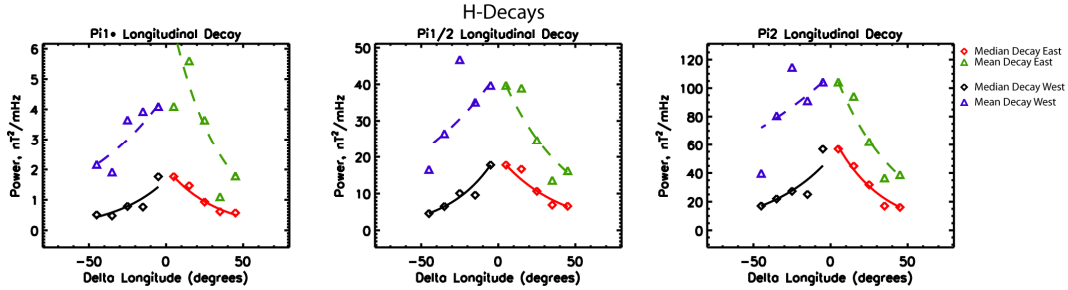


Figure 2.6: The longitudinal decay of the H-component ULF wave power in the Pi1\*, Pi1-2 and Pi2 wavebands (left, middle, right) as a function of delta longitude (negative west and positive east). Green (blue) triangles are the mean east (west) ULF wave power and the dashed green (blue) curve the least absolute deviation fit to the triangles. The red (black) diamonds are the median east (west) ULF wave power and the black (red) curve the fit to the diamonds.

Figure 2.6 shows the longitudinal decay scales in the same format as Figure 2.5. Figure 2.6 illustrates the mean east and west (green and blue triangles, respectively) and median east and west (red and black diamonds, respectively) summed power as a function of  $\Delta long$ . The mean and median values are calculated in the same as were those in Figure 2.5, except the averages are taken over the three latitudinal bins centered on the auroral intensification, defined by  $|\Delta lat| < 3$  degrees. The longitudinal decays are again fitted using a least absolute deviation method to a curve characterising the spatial decay of PSD with respect to longitude,  $\lambda_{long}$ . The longitudinal decay scales are summarised in Table 2.4 and the fitted curves are overplotted in Figure 2.6. In general the median spatial decay rate of power away from the onset region is smaller and more symmetric in the east/west directions than the mean spatial decay rate. The mean longitudinal decay rate is very asymmetric in the east/west directions where the westward spatial decay scale is larger than the eastward spatial decay. The asymmetry in the mean longitudinal decay rates is consistent with the additional localisation of mean summed power observed westward of the location of the Frey auroral intensification, c.f., Figure 2.4, which is not observed in the median summed power distributions, c.f., Figure 2.3. Moreover, Table 2.4 shows that the H- and D-component mean longitudinal decay scales of the Pi1\*, Pi1-2 and Pi2 to the west may be ULF waveband dependent such that shorter period waves (i.e. Pi1\* band) are more localised

to auroral onset and longer period waves (i.e. the Pi2 band) can be observed further from the auroral brightening. Conversely, the mean longitudinal decay scales to the east and the median decay scales to the east and west appear to be comparable across all wavebands varying at most by  $\sim 15^\circ$  (1 hr of local time) which is comparable to the longitudinal grid resolution used in this statistical study.

Figure 2.3 and Figure 2.4 both show evidence that the amplitude of ULF wave power appears to be dependent on period band, i.e. higher ULF wave power is observed in longer period bands. However, and Table 2.4 illustrate that the spatial decay scales of Pi1\*, Pi1-2 and Pi2 waves can be very similar. To determine whether there is a clear difference between the Pi1\*, Pi1-2 and Pi2 power spectra we can look at the statistical ULF wave PSD observed surrounding substorm onset. Figure 2.7 shows the mean (black), median (blue) and the upper and lower quartile (dashed red) ULF wave power spectra on a log-log scale for both the H and D magnetic field components (top and bottom, respectively). Each of the statistical power spectra in Figure 2.7 are determined from all magnetometer power spectra between  $|\Delta lat| \leq 3^\circ$  and  $|\Delta long| \leq 25^\circ$ , an area corresponding to approximately the north/south and east/west e-folding lengths of ULF wave power surrounding substorm onset, c.f., and Table 2.4. In Figure 2.7 the mean, median and upper and lower quartile ULF wave power spectra, in both the H and D magnetic field components, are characterised by a power law with a slope of approximately -3.7. The continuous and linear power law spanning the Pi1\*, Pi1-2 and Pi2 bands illustrated in Figure 2.7 strongly suggests that there is no statistical evidence of any preferred ULF wave frequency band during the forty minute period surrounding magnetic substorms. Figure 2.7 also clearly shows that the mean power is larger than the median, and is in fact comparable in amplitude to the upper quartile spectra. A detailed analysis of the distribution of ULF wave power at each individual frequency in the Pi1\*, Pi1-2 and Pi2 wavebands (not shown) reveals that the disparity between the median and mean ULF wave power is the result of ULF wave power adhering to an approximately exponential distribution with a long tail toward high amplitude ULF wave power events. Hence for this particular distribution of events the mean value of ULF wave power at each frequency is larger than the median value.

Finally, we present the statistical distribution of the angle of azimuth and ellipticity of Pi1\*, Pi1-2 and Pi2 ULF waves to determine if any differences exist in the polarisation of ULF pulsations in the three wavebands. It is important to note that the occurrence distribution of ULF wave azimuth in spatial bins surrounding the onset locations (c.f., Figure 2.2) can be characterised by a double peaked distribution, with one peak at a negative azimuth and the other at a positive azimuth. In general, a larger number of events are observed in one peak as compared to the other. In this type of distribution the mean can be close to zero, though skewed towards the dominant peak. The median value on the other hand will tend to represent a value contained within the dominant peak, that is the one with a larger number of events. In this section we concentrate on the median values for both the azimuths and ellipticities as it provides a better characterisation of the distributions. We do however note that although the median and mean azimuth and ellipticities can have different values, the two-dimensional spatial patterns of the mean and median values display very similar trends.

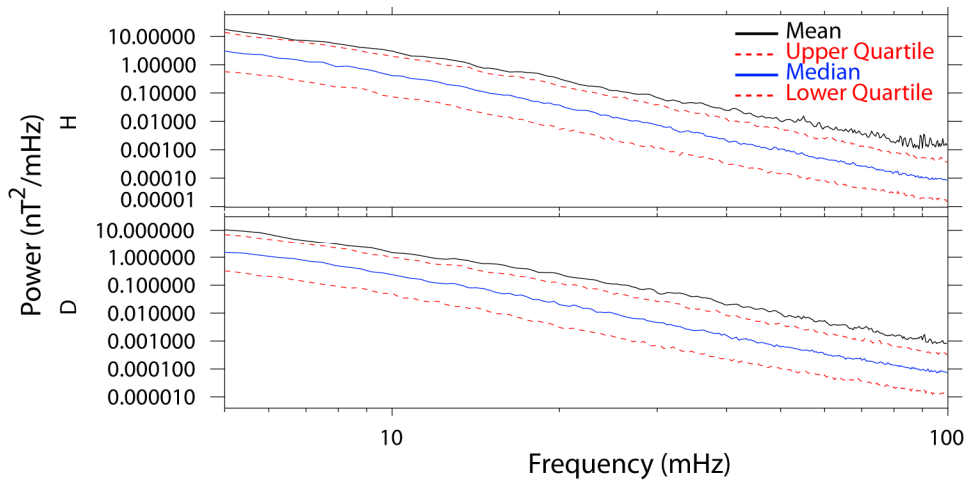


Figure 2.7: The statistical ULF wave power spectra determined from all available magnetometer stations within  $|\Delta lat| \leq 3^\circ$  degrees and  $|\Delta long| \leq 25^\circ$  degrees. The top panel is mean (black), median (blue) and upper and lower quartile (dashed red) power spectra for the H-component magnetic field. The bottom panel is the same as the top for the D-component magnetic field.

Figure 2.8 shows the two dimensional distribution of the median angle of azimuth of the Pi1\*, Pi1-2 and Pi2 ULF waves (left, middle and right columns) observed during substorm expansion phase onset in the same format as Figure 2.3. In both the Pi1-2 and Pi2 wavebands between approximately  $-5^\circ$  and  $5^\circ \Delta lat$  and at  $\Delta long$  distances smaller than  $-65^\circ$  the angle of azimuth is predominantly negative and at  $\Delta long$  distances greater than

65° the angle of azimuth is predominantly and largely positive. Between  $-65^\circ < \Delta long < 65^\circ$  and  $-5^\circ < \Delta lat < 5^\circ$  the median angle of azimuth is typically small though predominantly positive. Additionally above (below)  $\Delta lat = 5^\circ$  ( $\Delta lat = -5^\circ$ ) the angle of azimuth is primarily positive (negative). Unlike the Pi1-2 and Pi2 azimuth distributions the Pi1\* azimuths do not have such a clear pattern. At distances smaller than  $\Delta long = -65^\circ$  and below  $\Delta lat = -5^\circ$  the azimuths are predominantly positive; however, in the center of the Pi1\* distribution the azimuths are both positive and negative whereas the Pi1-2 and Pi2 distributions are predominantly positive.

Figure 2.9 shows the median ellipticity in the same format as Figure 2.8. The median Pi1\* ellipticity is predominantly positive throughout the entire distribution. In the Pi1-2 and Pi2 wavebands a clear pattern exists in the distribution of both the median ellipticities. In the region between  $-1^\circ < \Delta lat < 1^\circ$  and  $-65^\circ < \Delta long < 65^\circ$  the ellipticity is predominantly positive (right-handed or clockwise) and outside of this region the ellipticity is predominantly negative (left-handed or counter clockwise).

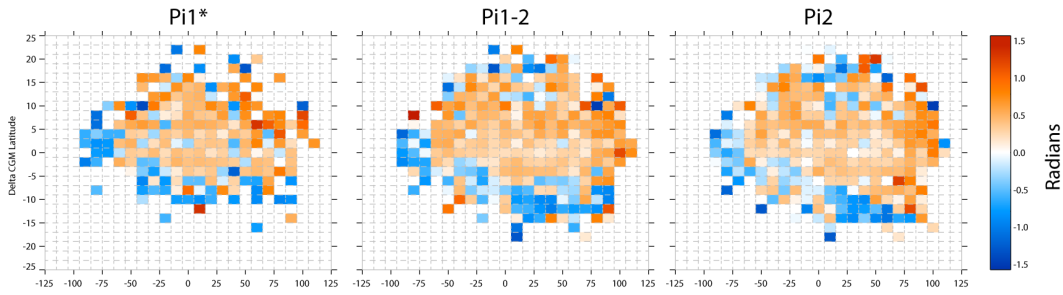


Figure 2.8: The median two-dimensional distribution of the ULF wave angle of azimuth with respect to auroral onset in the Pi1\*, Pi1-2 and Pi2 wavebands (left, middle, right). The color bar depicts the angle of azimuth in radians bounded by  $[-\pi/2, \pi/2]$ .

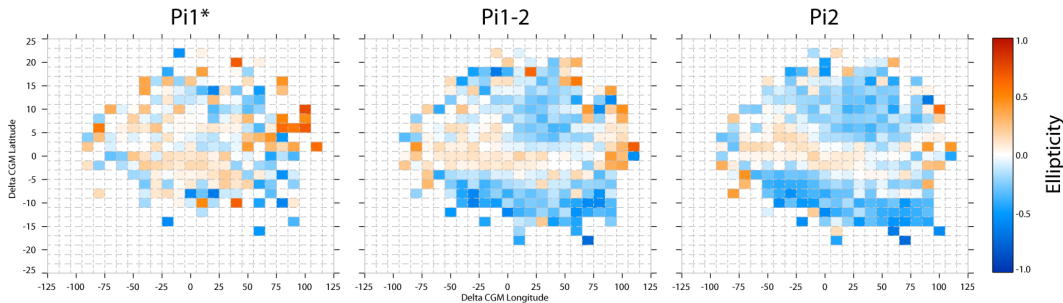


Figure 2.9: The median two-dimensional distribution of ULF wave ellipticities in the Pi1\*, Pi1-2 and Pi2 (left, middle, and right) wavebands as a function of relative distance from auroral onset. The color bar denotes the value of ellipticity in each spatial bin.

## 2.4 Discussion

In this study we have utilised a subsection of the Frey substorm database [Frey et al., 2004; Frey and Mende, 2006] magnetically conjugate to the CARISMA and CANMOS magnetometer arrays during a 4.5 year period to statistically characterise the ground magnetic wave power and polarisation parameters of impulsive ULF waves in the long-period Pi1 (10-40s, referred to here as Pi1\*), Pi1-2 (24-96s) and Pi2 (40-150s) during substorm expansion phase onset. Historically impulsive ULF waves observed at substorm onset have been classified as either Pi1 or Pi2 pulsations with a clear demarcation between the two wavebands at 40 s based on the classification by Jacobs et al. [1964]. More recently, an increasingly complicated classification scheme has been adopted by researchers. Heacock [1967] classified the ULF waves observed during substorm onset as either broadband (PiB) or continuous pulsations (PiC). Bösinger et al. [1981] used a mixed scheme classifying broadband low period waves associated with the aurora and substorms as Pi1B waveforms. Additionally, Murphy et al. [2009a; see also, Murphy et al., 2009b; Rae et al., 2009a; Rae et al., 2009b; Rae et al., 2010a] introduced Pi1-2 waves (24-96s) with periods encompassing long period Pi1 waves and short period Pi2 waves, which are associated with auroral waveforms and the initial magnetic disturbance during the substorm expansion phase onset [Maynard et al., 1996; Rae et al., 2009a; Rae et al., 2009b]. Currently, Pi1B [Bösinger and Yahnin, 1987], Pi1-2 [Murphy et al., 2009a] and Pi2 [Jacobs et al., 1964] pulsations have become common wavebands for characterising the substorm expansion phase. Hence the statistical analysis of the long-period Pi1 (referred to here as Pi1\*), Pi1-2 and Pi2 ULF wavebands during substorm expansion phase onset will help to determine whether the waveband classification scheme for impulsive ULF pulsations is appropriate or whether in fact any significant difference exists across the impulsive Pi type pulsations observed in these wavebands during magnetic substorms .

Olson and Rostoker [1975] presented a number of case studies demonstrating that strong Pi2 wave activity is linked to the enhanced westward electrojet forming during the substorm expansion phase. Additionally, Posch et al. [2007] have shown that Pi1B wave activity is localised to within  $\pm 5^\circ$  magnetic latitude and  $\pm 2$  hr of MLT ( $\sim \pm 23^\circ$  magnetic longitude) of the global auroral intensification defined in the Frey substorm

database. The results presented in this paper of the two-dimensional distribution of the median and mean summed ULF wave power in the Pi1\*, Pi1-2 and Pi2 wave bands and median angle of azimuth are consistent with both these studies, specifically Figure 2.3, Figure 2.4 and Figure 2.9 respectively. However our results additionally show that the isolation of ULF wave power is not limited to Pi2 or Pi1B waves but rather it is characteristic of the 10-150 s ULF wave spectrum studied herein.

Figure 2.3 and Figure 2.4 show that statistically the largest power in the three ULF wavebands (Pi1\*, Pi1-2 and Pi2) is spatially located near auroral onset in both the H- and D-components, similar to that for Pi2 waves as shown by Olson and Rostoker [1975] and Pi1B waves as demonstrated by Posch et al. [2007]. Interestingly the mean summed ULF wave power also shows a clear westward extension of high amplitude power along the latitude defining auroral onset (within  $\Delta lat = \pm 5^\circ$ ). To a lesser extent, high-amplitude ULF wave power is also observed directly poleward, equatorward and east of auroral onset. Note, that in general the mean ULF wave power in all three wave bands is larger than the median and that the amplitude of ULF wave power appears to be a function of period band; that is, there is more power in the longer period ULF wave bands (power in the Pi2 band > power in the Pi1-2 band > power in the Pi1\* band). This will be discussed in more detail below.

The extended region of high-amplitude ULF wave power westward of the auroral onset along the latitude of the onset electrojet (Figure 2.4) is characteristic of the region where the SCW and WTS form following auroral onset [McPherron, 1979]. Lester et al. [1983] demonstrated that the angle of azimuth of Pi2 waves can be used to identify the longitudinal extent of the SCW and the location of the upward and downward FAC elements. East (west) of the downward (upward) FAC the angle of azimuth of Pi2 waves is positive (negative); the azimuth pointing away from the downward (upward) FAC element. Between the downward and upward FAC elements the angle of azimuth of Pi2 waves points towards the center of the enhanced westward electrojet, rotating through negative values east of the center, through zero at the center of the electrojet and having positive values west of the center. In addition, Gelpi et al. [1987] demonstrated that the angle of azimuth of Pi2 pulsations points toward the head or leading edge of the WTS. There is evidence of both the azimuthal pattern described by Lester et al.

[1983] and that described by Gelpi et al. [1987] in the two-dimensional spatial distribution of the median angle of azimuth presented here (Figure 2.8). This demonstrates that the westward extension of ULF wave power occurs consistently along the electrojet latitude inside the SCW and in the region of the development of the WTS. In contrast to previous studies however, we demonstrate that the azimuthal patterns described by Lester et al. [1983] and Gelpi et al. [1987] can be observed not only in the Pi2 waveband but also in the Pi1-2 waveband and to a lesser extent in the Pi1\* waveband. This raises an interesting possibility that the temporal evolution of ULF waves during onset can be better understood by additionally using shorter period Pi ULF wave bands.

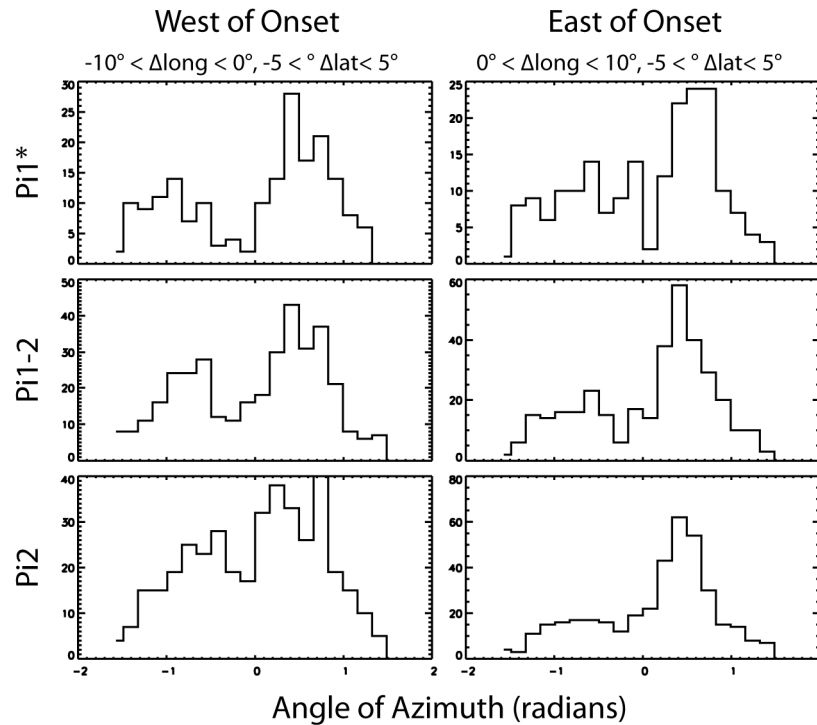


Figure 2.10: The distribution of the angle of azimuth between  $|\Delta lat| < 5^\circ$  just west of onset ( $-10^\circ < \Delta long < 0^\circ$ , left panels) and just east of onset ( $0^\circ < \Delta long < 10^\circ$ , right panels) in the Pi1\*, Pi1-2 and Pi2 wavebands (top, middle and bottom rows respectively).

Near the latitude of auroral onset ( $|\Delta lat| < 5^\circ$ ) and sufficiently east of auroral onset ( $\Delta long \gtrsim 65^\circ$ ) the angle of azimuth of ULF waves in the Pi1-2 and Pi2 ULF wave bands is positive. Similarly, sufficiently west of auroral onset ( $\Delta long \lesssim -65^\circ$ ) the angle of azimuth is negative, c.f., Lester et al. [1983]. Closer to the onset location  $|\Delta long| \lesssim 65^\circ$  the pattern described by Lester et al. [1983] is not clearly observed in our statistical

polarisations. In this region the azimuths are predominantly positive. This is likely the result of the superposition of substorms of varying size and intensity in the statistical study. For example if the longitudinal extent of the SCW varies on an event by event basis then it is likely that the pattern described by Lester et al. [1983] will only be observed in regions where the ULF wave azimuth is consistently oriented as positive or negative, i.e., east of the downward FAC element and west of the upward FAC element where the azimuths are consistently positive and negative, respectively. Within the SCW where the azimuth rotates through negative to positive values (from east to west) it will be more difficult to observe the pattern described by Lester et al. [1983] due to the varying size of the SCW in individual events. This is confirmed by Figure 2.10 which shows the occurrence distribution of the angle of azimuths 0-10° west of onset (left panels) and 0-10° east of onset (right panels) in the Pi1\*, Pi1-2 and Pi2 wavebands (top, middle and bottom rows respectively). Apparent in Figure 2.10 is that both east and west of the Frey auroral onset location the overall distribution of the angle of azimuth is characterised by two reasonably distinct distributions; one peaked at a negative angle of azimuth ( $\sim-\pi/4$ ) and the other at a positive angle of azimuth ( $\sim\pi/4$ ). East of the auroral onset (Figure 2.10, right panels) the occurrence distribution of positive azimuth values in all three ULF wave bands is significantly larger than that of the negative azimuths suggesting that this region may typically lie east of the downward FAC element of the SCW where the angle of azimuth is positive. West of auroral onset (Figure 2.10, left panels) the occurrence distribution of the angle of azimuth is still dominated by positive values; however, the occurrence of negative azimuths is larger in this region as compared to the region east of auroral onset. This suggests that the region west of the Frey auroral onset location can be both east and west of the downward FAC element of the SCW which develops during the expansion phase onset, where the angles of azimuth are positive and negative, respectively. The presence of a two peaked occurrence distribution of angle of azimuths both east and west of auroral onset clearly illustrates the superposition of SCWs of varying size and relative location with respect to the location of the Frey auroral onset. Further work is required analysing the temporal evolution of the SCW to determine whether there are systematic relationships between the relative location of the upward and downward FAC elements and the Frey auroral onset location. It is also interesting to note that typical size of a SCW identified using

the statistical superposition in this study is  $\sim 8.5$  hours of local time, which is consistent with the widths of individual SCW as characterised by Lester et al. [1983] who found that the width of the was typically between  $\sim 4$  and  $\sim 12$  hours of local time with an average of  $\sim 6$  hrs. Note however that the SCW width reported here may correspond to an upper estimate of the width of the SCW as a result of the statistical superposition of many events. Similarly, Figure 2.8 also illustrates that the ULF wave azimuths in the Pi1-2 and Pi2 bands are consistent with those described by Gelpi et al. [1987]. At values of  $\Delta lat$  greater than  $5^\circ$  (less than  $-5^\circ$ ) the angle of azimuth in each of the Pi1-2 and Pi2 ULF wave bands is consistently positive (negative) pointing west toward the region which should be characterised by the head of the westward traveling surge.

The Pi1\* band shows some evidence of the patterns described by Lester et al. [1983] and Gelpi et al. [1987]. At distances smaller than  $\Delta long = -65^\circ$  the azimuth is predominantly negative consistent with the location of the upward FAC element [Lester et al., 1983] and at lower latitudes the azimuth is also negative pointing to the region characteristic of the WTS [Gelpi et al., 1987]. In the middle of the distribution near the auroral onset location the Pi1\* azimuths are more variable. Posch et al. [2007] showed that shorter period Pi1B ULF waves are well correlated with the spatial and temporal location of auroral onset. If the Pi1\* waves characterised herein are similar to the Pi1B pulsations studied by Posch et al. [2007] then it is likely that the Pi1\* pulsations will show no coherent azimuthal structure due to their broadband nature. However it is also possible that the Pi1\* waves may be localised in time near auroral onset also similar to Pi1B pulsations [Posch et al., 2007]. If that is the case then the forty minute window used to characterise the ULF wave azimuth may be too long compared to the period of Pi1\* waves thus making it difficult to accurately determine the orientation of the onset related Pi1\* azimuths. Future studies using a more well defined auroral onset time and thus allowing for the use of a smaller analysis window will help to determine whether Pi1\* waves exhibit a similar azimuthal pattern at onset to those found for Pi1-2 and Pi2 pulsations. The two-dimensional statistical summed power distributions and azimuth distributions of the Pi1-2 and Pi2 wavebands and potentially the Pi1\* waveband with respect to auroral onset are hence mostly consistent with previous studies which concentrated on a single ULF wave band and individual case studies [Gelpi et al., 1987; Lester et al., 1983]. Indeed the evidence above clearly illustrates that ULF wave power in

the Pi1\*, Pi1-2 and Pi2 wavebands is intimately connected with the substorm expansion phase and auroral onset and that both the Pi1-2 and Pi2 (and potentially the Pi1\* band) are linked to development of the SCW and WTS.

In general, it is believed that the ULF waves in the Pi1 band are confined to the location of substorm onset [Bösinger and Yahnin, 1987] whereas Pi2 waves are a global phenomenon which can at times be observed both in the night-side and day-side magnetosphere [Olson, 1999 and references therein]. The median (Figure 2.3) and mean (Figure 2.4) two dimensional distributions of ULF wave power show some evidence of this since Pi2 wave power is generally higher than that of the Pi1-2 and the Pi1\* waves studied in this paper and typically the Pi2 ULF wave power extends further in both latitude and longitude away from the Frey onset location than does the Pi1\* and Pi1-2 power. Similarly, Figure 2.3 and Figure 2.4 both demonstrate that Pi1\* wave power extends to larger latitudinal and longitudinal distances during substorms which are characterised by a large AE. Hence for smaller substorms Pi1 power may be more localised to the onset region. However, this localisation of ULF wave power may not be a result of the physical or spatial characteristics of Pi1\*, Pi1-2, and Pi2 waves but rather be a result of an observational limitation of the instrumentation used in this study and the amplitude of ULF wave at higher frequencies (e.g. Pi1\* waves) often having amplitudes comparable to the noise floor of the fluxgate magnetometers.

Figure 2.7 shows that the ULF wave power spectrum observed at substorm expansion phase onset is characteristic of a power law, so that higher frequency waves have inherently lower power. Additionally Figure 2.3 and Figure 2.4 (see also Figure 2.5 and Figure 2.6) show that the north/south and eastward decay of Pi1\*, Pi1-2, and Pi2 summed ULF wave power are symmetric in H and D and relatively similar. Taken together this suggests that the localisation of Pi1 power and global expansion of Pi2 power may simply be a result of the amplitude of Pi1 waves being inherently smaller than the amplitude of Pi2 waves, at least for the frequency range studied herein (10-150s period). Furthermore a single power law characterising the ULF wave power spectra during substorm expansion phase onset (Figure 2.7) demonstrates that there is no discernable change in the power spectrum at 40 s period delineating the formal boundary between the Pi1 and Pi2 wave bands. This suggests that statistically no

preferential frequency or frequency band exists during substorm expansion phase onset though this does not preclude a dominant ULF wave frequency existing during any particular substorm event.

It is however clear from this study that during any particular substorm the entire 10-150 s ULF waveband contains useful information about the onset process. It is important to note that the expansion and two-dimensional distribution of the shorter period (1-10 s) Pi1 wave power may differ significantly from the Pi1\* waveband (10-40 s) characterised herein, and may indeed be a ULF waveband with expansion limited to the auroral onset location [e.g., Posch et al., 2007]. Future studies will concentrate on utilising the high-cadence CARISMA search coil magnetometers that are more sensitive to lower amplitude higher frequency ULF waves, in conjunction with the fluxgate magnetometers. Such studies will determine whether the Pi1\* (10-40 s) wave power characteristics are representative of the entire Pi1 waveband (1-40 s), or whether the more natural break between the Pi1 and Pi2 ULF wave bands resides at periods of ~10s as opposed to the traditionally defined boundary at 40s.

Though not apparent in the latitudinal decay scales ( ) it is interesting to note that the summed ULF wave amplitude as a function of latitude (Figure 2.5) shows evidence of a localised peak in ULF wave power ~3° north of the auroral intensification identified optically by Frey et al. [2004] and Frey and Mende [2006]. Additionally, as mentioned in the analysis, an asymmetry exists in the mean east/west spatial decay scales such that the decay scales are larger to the west than to the east, with the westward spatial decay appearing to be a function of the specific Pi ULF waveband. In particular, the Pi2 waveband typically expands further west than the Pi1-2 waveband which typically expands further west than the Pi1\* waveband (Table 2.4). Without analysis of the temporal development of ULF wave power it is difficult to explain this increase of ULF wave power at higher latitudes and the asymmetry in the decay scales. However, in a companion paper Rae et al. [2010b] have shown that during isolated substorms a second activation or increase of ULF wave power at higher latitudes can be observed ~ 8-12 minutes following the initial onset of an isolated substorm. These authors argue this may be evidence of either a delayed response of ULF waves at higher latitudes or a secondary onset of ULF wave activity due to additional auroral intensifications. Similarly

Elphinstone et al. [1995a, see also Elphinstone et al., 1995b] showed that secondary activations of the poleward branch of the auroral oval (poleward boundary intensifications, PBIs) can occur in the pre-midnight sector following substorm expansion phase onset. Certainly, Figure 2.4 shows that there is enhanced mean ULF wave power to the north and west of auroral onset, a region that will likely encompass the poleward branch of the auroral oval. The peak in ULF wave power above the optical onset latitude observed here and the disparity in the mean and median westward decay scales may be a result of secondary activations of ULF wave power following onset [Rae et al., 2010b] which, in turn, may or may not represent PBIs observed during the substorm recovery phase [Elphinstone et al., 1995a,b]. Clearly, additional work is required to characterise the temporal development of ULF wave power during substorm expansion and recovery phases in order to fully understand the enhancement in ULF wave power at higher latitudes and the asymmetries in the mean longitudinal decays.

Table 2.3: The latitudinal decay scales ( $\Lambda_{lat}$ ) of the mean and median summed ULF wave power in the Pi1\*, Pi1-2 and Pi2 bands.

ULF Band	Mean - $\Lambda_{lat}$				Median - $\Lambda_{lat}$			
	H		D		H		D	
	North	South	North	South	North	South	North	South
Pi1*	2.94	3.85	3.15	3.60	5.75	4.20	6.67	3.75
Pi1-2	3.94	3.98	3.60	3.59	5.72	4.26	7.09	4.54
Pi2	4.00	3.48	4.50	3.04	5.61	3.29	7.12	4.79

Table 2.4: The longitudinal decay scales ( $\Lambda_{long}$ ) of the mean and median summed ULF wave power in the Pi1\*, Pi1-2 and Pi2 bands.

ULF Band	Mean - $\Lambda_{long}$				Median - $\Lambda_{long}$			
	H		D		H		D	
	East	West	East	West	East	West	East	West
Pi1*	30.45	61.41	34.60	43.59	32.11	33.77	24.40	25.54
Pi1-2	43.14	70.75	30.87	52.37	39.26	29.67	23.91	24.20
Pi2	39.59	108.72	29.03	58.74	30.99	41.04	25.10	26.91

Of note is that the median and mean summed ULF wave power and power spectra (see Figure 2.3, Figure 2.4, and Figure 2.9) reveal that the mean ULF wave power is larger than the median ULF wave power. This may be a natural consequence of the Frey

substorm database selection criteria, whereby more intense substorms are more easily and hence preferentially selected. Indeed Frey et al. [2004] and Frey and Mende [2006] use the criteria that to be identified as a substorm in their database the auroral brightening must expand both past the poleward boundary of the auroral oval and at least twenty minutes in azimuth. These selection criteria thus have the potential to exclude smaller substorm events from their substorm database. This will ultimately lead to the distribution of substorms identified in the Frey substorm database being skewed toward larger amplitude substorms associated with a larger expansion of the aurora. Moreover the distribution of wave power at each spectral estimate is characteristic of an exponential distribution. With an increased number of large amplitude substorm events and a consequent exponential distribution of ULF wave power, the distribution of ULF wave power may be skewed such that the mean is larger than the median.

With regards to ULF wave polarisation characteristics, Lester et al. [1983] and Gelpi et al. [1987] both demonstrated that the angle of azimuth of Pi2 waves is organized with respect to the formation of the SCW and WTS, respectively. Similarly Samson et al. [1971] showed that the ellipticity of ULF waves varied systematically as a function of local time and latitude. Using three consecutive days of magnetometer data Samson et al. [1971] showed that the ellipticity of night-side waves with periods between 50-1000s typically have a counter clockwise ellipticity at high latitudes ( $\text{CGM latitude} \geq 70^\circ$ ). Near auroral latitudes ( $60^\circ \geq \text{CGM latitude} \leq 70^\circ$ ) the ellipticity rotates to a clockwise orientation. At lower latitudes, near the latitude characterising the peak amplitude of ULF waves in the night-side magnetosphere ( $\text{CGM latitude} \leq 60^\circ$ ), the ellipticity rotates once again to a counter clockwise orientation. This pattern of ellipticity is consistent with the two-dimensional distribution of both the Pi1-2 and Pi2 ellipticities shown in Figure 2.9. In the region characterising the highest amplitude waves, near auroral onset ( $|\Delta\text{lat}| \leq \pm 5^\circ$ ), the ellipticity is predominantly clockwise (positive). Both to the north and south of this region the ellipticity is counter clockwise (negative) consistent with the pattern described by Samson et al. [1971]. Southwood and Hughes [1985] demonstrated that the wave ellipticity and azimuth observed by Samson et al. [1971] can be described as the superposition of a large amplitude westward propagating wave and a smaller amplitude eastward propagating wave. Our results are generally consistent with this hypothesis and the observations of Samson et al. [1971] in both the Pi1-2 and Pi2 bands.

Similar to the spatial distribution of the Pi1\* azimuths, the Pi1\* ellipticities show some similarities to the Pi1-2 and Pi2 ellipticities as well as the pattern described by Samson et al. [1971]. Near the location of auroral onset the Pi1\* ellipticity is predominantly positive consistent with both the Pi1-2 and Pi2 distributions. However, there is no clear rotation of the Pi1\* ellipticities to negative values at higher and lower latitudes. In these regions the Pi1\* ellipticities are more variable and can be both positive and negative. If the Pi1\* band is similar in nature to the broadband shorter period Pi1B ULF waves [Lessard et al., 2006; Posch et al., 2007] observed at substorm onset then it is possible that no clear pattern in the Pi1\* ellipticities exists. However it is clear from the results presented in this study that the amplitude of Pi1\* waves is in general small (Figure 2.3, Figure 2.4 and Figure 2.7). Additionally the period of Pi1\* waves compared to the analysis window is also small and similar to the Pi1B waves [Posch et al., 2007] may also be localised in time with respect to auroral onset. These factors may make it difficult to accurately characterise the ellipticity of the Pi1\* waveband especially away from the onset location where the amplitude of Pi1\* waves can be an order of magnitude smaller than those near onset. Future work using more sensitive higher cadence magnetometer instruments and auroral onset times with smaller uncertainties such that a smaller analysis window can be utilised, will help to determine whether the Pi1\* waves characterised herein are similar to the shorter period broadband Pi1B waves observed at substorm onset. For instance the high cadence CARISMA searchcoil magnetometers [Mann et al., 2008] and the recently published Polar-Ultra Violet Imager substorm database [Liou, 2010] which identifies substorms at a higher cadence and better spatial resolution than IMAGE-FUV, will be ideal for future work concentrating on Pi1\* pulsations. More importantly, searchcoil data will allow for the full 1-40 s Pi1 waveband to be characterised during the substorm expansion phase onset.

Though the Pi1\* polarisations show different structuring with respect to auroral onset as compared to the Pi1-2 and Pi2 polarisations, there remains strong evidence to suggest that statistically the three ULF wavebands comprise parts of a continuous power-law spectrum with similar two-dimensional distributions of power. Thus during substorm expansion phase onset it is imperative to study the entire ULF wave spectrum rather than focus on any particular wave band so that the results of any analysis are not biased to a pre-determined wave band. Hence we caution researchers to consider the

entire gamut of Pi ULF wave frequencies when studying the period surrounding auroral substorm expansion phase onset.

## 2.5 Summary and Conclusions

ULF waves have been associated with magnetic substorms for over 40 years [Jacobs et al., 1964]. In general the ULF waveforms observed during the onset of the substorm expansion phase are impulsive in nature and have been typically associated with the initial plasma sheet disturbance and the earthward propagation of Alfvén waves during the development of the SCW during expansion phase onset [e.g., Arnoldy et al., 1987; Olson, 1999]. In this manuscript we have statistically demonstrated that ULF wave power spectra during substorms and night-side activations can be described by a power-law in which the Pi1\*, Pi1-2 and Pi2 ULF wavebands have similar characteristics.

Statistically we find that during expansion phase onset:

- The highest Pi1\*, Pi1-2 and Pi2 ULF wave power is concentrated near auroral onset.
- High amplitude ULF wave power is more likely to be observed to the west of onset than to the east, for a give longitudinal distance from onset, in all wave bands.
- The statistical spectrum of ULF waves in the region close to auroral onset is characteristic of a power-law. No identifiable wave frequency dominates this statistical spectrum, for example in the Pi1\* or Pi2 wavebands, or at the boundary between these two wavebands, e.g. at 40s.
- The angle of azimuths in the Pi1-2 and Pi2 ULF wave bands with respect to the auroral intensification is the same and in agreement with the angle of azimuth of Pi2 pulsations characterised by Lester et al. [1983] and Gelpi et al. [1987].
- Both the Pi1-2 and Pi2 wavebands have similar ellipticity distributions which are consistent with the distribution of Pi2 ellipticities described by Samson et al. [1971].
- The azimuth and ellipticity of Pi1\* pulsations differs from that of the Pi1-2 and Pi2 pulsations. More work is required to determine whether the observed polarisation of the Pi1\* waveband is a result of the waves being broadband and similar in nature to the Pi1B waves studied by Posch et al. [2007] or a result of the temporal localisation of Pi1\* power. Future work will use more sensitive high cadence instrumentation to characterise the polarisation of the entire Pi1 waveband.

In the original classification of Pi1 and Pi2 pulsations, Jacobs et al. [1964] noted that “In any decisions on notation and classification, compromise is inevitable. Since the physical processes involved are not well understood it is pointless to introduce a highly sophisticated scheme”. With an ever increasing body of work characterising the physical driving mechanism of ULF waves observed at substorm expansion phase onset [see for instance Kepko and Kivelson, 1999; Lessard et al., 2006; Lysak, 1988; Olson, 1999; Rae et al., 2009a; Rae et al., 2010a] it is clear that a more appropriate classification scheme based on the driver of a specific ULF wave observed during substorm expansion phase onset is required. Both the temporal evolution of ULF waves presented in Paper 2 and the spatial distribution of ULF wave power and polarisation presented herein demonstrate that the entire ULF wave spectrum should be considered during substorm expansion phase onset. If the substorm community is to continue to use the Jacobs et al. [1964] classification of impulsive ULF we stress the importance that the entire ULF wave spectrum be taken into account when studying ULF pulsations observed during magnetic substorms.

## 2.6 References

- Akasofu, S. I. (1964), The development of the auroral substorm, *Planet. Space Sci.*, 273-282.
- Arnoldy, R. L., et al. (1987), Simultaneous Measurement of Aurora-Related, Irregular Magnetic Pulsations at Northern and Southern High-Latitudes, *J. Geophys. Res.*, 92, 12221-12232.
- Arthur, C. W., et al. (1976), A comparative study of three techniques for using the spectral matrix in wave analysis, *Radio Science*, 11, 833-845.
- Beamish, D., et al. (1979), Complex demodulation applied to Pi2 geomagnetic pulsations, *Geophys. J. R. astr. Soc.*, 58, 471-493.
- Bösinger, T., et al. (1981), Correlation between Pi type magnetic micropulsations, auroras, and equivalent current structures during two isolated substorms, *J. Atmos. Terr. Phys.*, 43(9), 933-945.

- Bösinger, T., and A. G. Yahnin (1987), Pi1b Type Magnetic Pulsation as a High Time Resolution Monitor of Substorm Development, *Ann. Geophys.*, 5, 231-237.
- Cramoysan, M., et al. (1995), The use of a model current wedge in the determination of the position of substorm current systems, *Ann. Geophys.*, 13(6), 583-594.
- Elphinstone, R. D., et al. (1995), The Double Oval UV Auroral Distribution, 1. Implications for the Mapping of Auroral Arcs, *J. Geophys. Res.*, 100(A7), 12,075–12,092, doi:10.1029/95JA00326.
- Elphinstone, R. D., et al. (1995), The Double Oval UV Auroral Distribution, 2. The Most Poleward Arc System and the Dynamics of the Magnetotail, *J. Geophys. Res.*, 100(A7), 12, 093–12, 102.
- Fowler, R. A., et al. (1967), Polarization Analysis of Natural and Artificially Induced Geomagnetic Micropulsations, *J. Geophys. Res.*, 72(11), 2871-2883.
- Frey, H. U., et al. (2004), Substorm onset observations by IMAGE-FUV, *J. Geophys. Res.*, 109.
- Frey, H. U., and S. B. Mende (2006), Substorm onsets as observed by IMAGE-FUV, *Proceeding of ICS8*, 71-75.
- Gelpi, C., et al. (1987), A comparison of magnetic signatures and DMSP auroral images at substorm onset: Three case studies, *J. Geophys. Res.*, 92(A3), doi:10.1029/JA1092iA1003p02447.
- Heacock, R. R. (1967), Two Subtypes of Type Pi Micropulsations, *J. Geophys. Res.*, 72, 3905-3917.
- Heppner, J. P. (1958), A study of the relationships between the aurora borealis and the geomagnetic disturbances caused by electric currents in the ionosphere, *Defence Research Board Canada*, DR135.
- Jacobs, J. A., et al. (1964), Classification of Geomagnetic Micropulsations, *J. Geophys. Res.*, 69(1), 180-181.
- Kepko, L., and M. G. Kivelson (1999), Generation of Pi2 pulsations by bursty bulk flows, *J. Geophys. Res.*, 104, 25021-25034.

- Lessard, M. R., et al. (2006), Nature of Pi1B pulsations as inferred from ground and satellite observations, *Geophys. Res. Lett.*, 33.
- Lester, M., et al. (1984), Longitudinal Structure in Pi 2 Pulsations and the Substorm Current Wedge, *J. Geophys. Res.*, 89(A7), 5489-5494.
- Lester, M., et al. (1989), Pi 2 Pulsations and the Substorm Current Wedge: Low-Latitude Polarization, *J. Geophys. Res.*, 92(A12), 1133-1141.
- Lester, M. R., et al. (1983), Polarization patterns of Pi 2 magnetic pulsations and the substorm current wedge, *J. Geophys. Res.*, 88, 7958-7966.
- Liou, K. (2010), Polar Ultraviolet Imager Observation of Auroral Breakup, *J. Geophys. Res.*, doi:10.1029/2010JA015578.
- Lysak, R. L. (1988), Theory of Auroral Zone PiB Pulsation Spectra, *J. Geophys. Res.*, 93, 5942-5946.
- Mann, I. R., et al. (2008), The Upgraded CARISMA Magnetometer Array in the THEMIS Era, *Space Sci. Rev.*, 141, 413-451.
- Maynard, N. C., et al. (1996), Magnetosphere-ionosphere coupling during substorm onset, ESA Publications Div., Noordwijk, The Netherlands.
- McPherron, R. L. (1979), Magnetospheric Substorms, *Rev. Geophys. Space Phys.*, 17, 657-681.
- Mende, S. B., et al. (2000), Far Ultraviolet Imaging from the Image Spacecraft. 1. System Design, *Space Sci. Rev.*, 91, 243-270.
- Milling, D. K., et al. (2008), Ionospheric localisation and expansion of long-period Pi1 pulsations at substorm onset, *Geophys. Res. Lett.*, 35(L17S20).
- Murphy, K. R., et al. (2009a), Wavelet-based ULF wave diagnosis of substorm expansion phase onset, *J. Geophys. Res.*, 114.
- Murphy, K. R., et al. (2009b), Reply to the comment by K. Liou and Y.-L. Zhang on "Wavelet-based ULF wave diagnosis of substorm expansion phase onset", *J. Geophys. Res.*, 114, A10207, doi:10.1029/2009JA014351.

- Murphy, K. R., et al. (2011), The dependence of Pi2 waveforms on periodic velocity enhancements within bursty bulk flows, *Ann. Geophys*, 29, 493-509
- Nishimura, Y., L. Lyons, S. Zou, V. Angelopoulos, and S. Mende (2010), Substorm triggering by new plasma intrusion: THEMIS all-sky imager observations, *J. Geophys. Res.*, 115, A07222, doi:10.1029/2009JA015166.
- Olson, J. V., and G. Rostoker (1975), Pi 2 Pulsations and the Auroral Electrojet, *Planet Space Sci.*, 23, 1129-1139.
- Olson, J. V. (1999), Pi2 Pulsations and substorm onsets: A review, *J. Geophys. Res.*, 104, 17499-17520.
- Posch, J. L., et al. (2007), Statistical observations of spatial characteristics of Pi1B pulsations, *J. Atmos. Terr. Phys.*, 69(15), 1775-1796.
- Press, W. H., et al. (1992), *Numerical Recipes in C: The Art of Scientific Computing* Second Edition Cambridge University Press.
- Rae, I. J., et al. (2006), Pi2 pulsations: Field Line resonances of a Driven Response, *Proceeding of ICS8*, 253-258.
- Rae, I. J., et al. (2009a), Near-Earth Initiation of a Terrestrial Substorm, *J. Geophys. Res.*, doi:10.1029/2008JA013771.
- Rae, I. J., et al. (2009b), Timing and localization of ionospheric signatures associated with substorm expansion phase onset, *J. Geophys. Res.*, 114(A00C09).
- Rae, I. J., et al. (2010a), Optical characterisation of the growth and spatial structure of a substorm onset arc, *J. Geophys. Res.*, doi:10.1029/2010JA015376.
- Rae, I. J., et al. (2010b), On the nature of ULF wave power during nightside auroral activations and substorms: 2. Temporal Evolution, *J. Geophys. Res.*, doi:10.1029/2010JA015762.
- Rostoker, G., et al. (1995), Canopus - A ground-based instrument array for remote sensing the high latitude ionosphere during the ISTP/GGS program, *Space Sci. Rev.*, 41, 743-760.

- Sakaguchi, K., et al. (2009), Fine structures and dynamics in auroral initial brightening at substorm onset, *Ann. Geophys.*, 27, 623-630.
- Samson, J. C., et al. (1971), Latitude-Dependent Characteristics of Long-Period Geomagnetic Pulsations, *J. Geophys. Res.*, 76, 3675-3683.
- Southwood, D. J. (1974), Some Features of Field Line Resonances in the Magnetosphere, *Planet. Space Sci.*, 22, 483-491.
- Southwood, D. J., and W. J. Hughes (1985), Concerning the Structure of Pi 2 Pulsations, *J. Geophys. Res.*, 90, 386-392.
- Wright, A. N., and I. R. Mann (2006), Global MHD Eigenmodes of the Outer Magnetosphere, in *Magnetospheric ULF Waves, Synthesis and New Directions*, edited by K. Takahashi, et al., pp. 51-72.

## Chapter 3 Reduction in Field-Aligned Currents

### Preceding and Local to Auroral Substorm Onset<sup>2</sup>

#### 3.1 Introduction

Magnetic substorms are marked in the ionosphere by a well-defined sequence of events: a brightening of either the most equatorward growth-phase arc or a newly formed equatorward arc, the poleward motion of this arc and subsequent explosive break-up of the aurora [Akasofu, 1977, and references therein]. However, despite being well characterised in the ionosphere there is no consensus among researchers on the physical mechanism leading to the initiation of substorm onset in the magnetosphere [see for instance the debate in Science - Angelopoulos et al., 2008; Lui, 2009; Angelopoulos et al., 2009].

Two of the more commonly-debated substorm paradigms are the near-Earth neutral line (NENL) and current disruption (CD) models. Each of these phenomenological models describes a sequence of events in the magnetosphere which are suggested to directly relate magnetospheric phenomena to auroral activity in the ionosphere. In the NENL paradigm, magnetic reconnection initiates on stretched field lines at a distance of ~20-25 RE triggering magnetospheric substorm expansion phase onset [e.g., Baker et al. 1996; Angelopoulos et al., 2008]. In the CD paradigm magnetospheric expansion phase onset is triggered by a localised plasma instability in the inner magnetosphere [Lui, 1996], potentially by a ballooning mode [e.g., Roux et al., 1991; Samson et al. 1996], lower hybrid turbulence [e.g., Huba et al., 1977], or a cross-field current instability in the central plasma sheet [e.g., Lui et al., 1995; Rae et al., 2010]. Other models including the near-Earth geophysical onset (NGO) [Maynard et al., 1996] and global Alfvénic interaction [Song and Lysak, 2001] have also been postulated, although these latter scenarios typically receive less attention in the literature. Though each substorm paradigm hypothesises a link between the sequence of events in the magnetosphere and the well-defined sequence of auroral events observed in the ionosphere [Akasofu, 1964], the connection between the magnetosphere and ionosphere remains a critical

---

<sup>2</sup>A version of this chapter has been accepted for publication. Murphy, K. R., et al. (2012), *Reduction in field-aligned currents preceding and local to auroral substorm onset*, *Geophys. Res. Lett.*, 39, L15106, doi:10.1029/2012GL052798.

element in all substorm models that is not well understood. In this Chapter we use detailed estimates of the field aligned currents (FACs) and ionospheric equivalent currents to show that there is a localised change in M-I coupling in advance of and in a region coincident with auroral onset.

### **3.2 Instrumentation**

We present the first in-situ observations of the structure and evolution of the FACs associated with a magnetic substorm from the Active Magnetosphere and Planetary Electrodynamics Response Experiment (AMPERE), together with supporting conjugate auroral images and ground-based and geosynchronous magnetometer data. The global FAC structure can be estimated with AMPERE using the vector magnetic field measured on the Iridium constellation of low-Earth orbiting satellites [Anderson et al., 2000; Waters et al., 2001]. Using over seventy spacecraft a part of the Iridium constellation and distributed in 6 orbital tracks, FACs can be determined on the scale of the MLT separation of the Iridium orbital planes at an altitude of  $\sim 780$  km. Reliable FACs estimates from AMPERE are derived when the system is quasi-stationary on the timescale of the satellite separation in each orbital track,  $\sim 10$  minutes so that temporal changes in the system between satellite passes can be neglected.

Estimates of ionospheric equivalent current structures can be determined using a network of closely spaced ground-based magnetometers, to complement the AMPERE derived FACs. In this study, ground-based equivalent currents (ECs) are determined using the H- and D-component magnetometer data from the CARISMA [Mann et al., 2008] and THEMIS [Russell et al., 2008] magnetometer arrays. After a quiet day curve is removed from each magnetometer time series the entire dataset is interpolated onto a uniform grid and the ECs are calculated based on the infinite current sheet assumption [Lühr and Schlegel, 1994].

In the following section we present a detailed picture of ground-based auroral and magnetic observations, as well as in-situ observations of the AMPERE FAC system and geosynchronous magnetic field perturbations during an isolated and very clearly characterised substorm observed on the 16 February 2010 between 06:00 and 08:00 UT. Auroral observations are provided by the THEMIS white light All-sky Imagers (ASIs) [Mende et al., 2008] at a 3 second resolution and the NORSTAR Forth Smith (FSMI)

meridian scanning photometer at 486 and 630 nm wavelengths (the proton and electron aurora, respectively) at a 30 second cadence [Donovan et al., 2003]. The geosynchronous magnetic field is provided by the GOES 11 and GOES 14 satellites (G11 and G14, respectively) at 60 second cadence [Singer et al., 1996]. Higher resolution GOES 11 is not available for this event.

### 3.3 Observations

Figure 1a shows the prevailing solar wind and IMF conditions propagated to the magnetosphere from the OMNI-2 database at 5 minute resolution [King and Papitashvili, 2005]. The highlighted region depicts the time period of interest during which the substorm is observed. During this period the GSM Bz is consistently small (mean of -3.4 nT) and directed southward and shows little variation and the solar wind velocity is relatively slow and constant (mean of -321 km/s). Figure 3.1 panels (b) through (e) show an overview of the substorm from 0600-0800 UT on the 16 February 2010 from geosynchronous orbit (Figure 3.1 b and c) and from ground-based THEMIS Fort Simpson (FSIM) all-sky imager (d) and CARISMA FSIM magnetometer (e) at the location of auroral substorm onset. At onset G11 was located in the pre-midnight sector and conjugate to both the FSIM station and auroral onset and G14 was located around local midnight.

A clear dipolarisation is observed at G11 and G14 at ~07:25 UT, characterised by the sharp increase in the magnetic field strength and inclination angle observed at G14, typical of a magnetospheric substorm [McPherron, 1979]. Earlier there is a localised reduction in the G11 magnetic field strength of ~5 nT for about 3 minutes around 07:19 UT-07:22 UT. A clear substorm growth phase is evident in the FSIM ASI keogram between ~06:30-07:15 UT, characterised by the equatorward motion of the auroral oval [Akasofu, 1964]. Also apparent in the keogram is the formation of an equatorward arc at 07:06 UT which briefly fades and subsequently brightens and expands poleward at 07:18:30 UT marking auroral substorm onset [Akasofu, 1977]. This brightening and expansion is coincident in time with the reduction in magnetic field strength at the conjugate G11 satellite (to within the 60s resolution of the GOES data). Auroral break-up at 07:25:30 UT is coincident in time with the dipolarisation at G14 and G11. Finally note the formation of the positive D-component and negative H- and Z-component magnetic bays at FSIM which are typical of the enhancement of ionospheric electrojets and

formation of the substorm current wedge (SCW) following onset [Clauer and McPherron 1974].

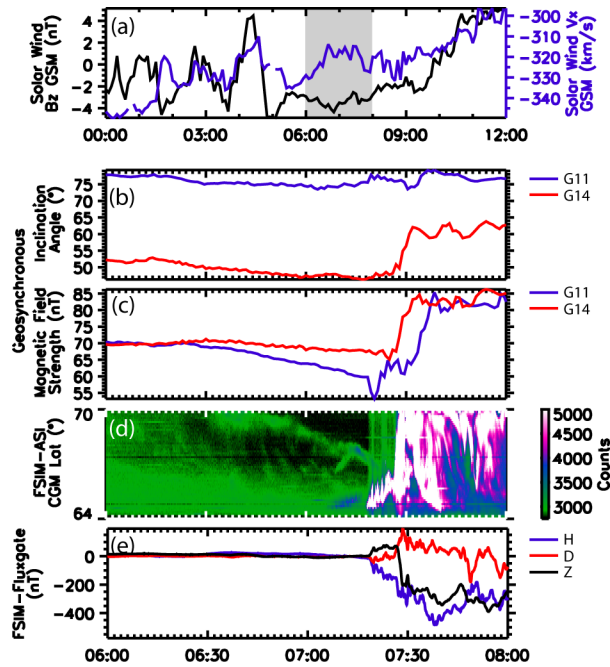


Figure 3.1:(a) The GSM x-component of the solar wind velocity (blue) and the GSM z-component of the solar wind magnetic field (black), the highlighted region denotes the time period during which the substorm is observed. (b) The G11 (blue) and G14 (red) inclination angle defined as the angle between the magnetic field and the vector sum of the x and y components in the local satellite ENP coordinate system. (c) G11 (blue) and G14 (red) total magnetic field strength. (d) FSIM ASI keogram; the keogram is constructed from a slice through the ASI perpendicular to the growth phase arc. (e) The H-, D-, and Z-component magnetic field variations from the FSIM magnetometer.

Figure 3.2 shows the evolution of the aurora from the FSMI and FSIM ASIs and the FSIM MSP at selected times. The dotted blue line denotes the geomagnetic latitude of the peak in the proton auroral intensity at FSMI which marks the inner edge of the ion plasmashet and the transition from dipole to tail-like magnetic field [Samson et al., 1992]. The dotted red line marks the poleward border of the electron aurora at FSMI characterising the open closed field line boundary (OCFLB) in the magnetosphere [Blanchard et al., 1995] determined using the method of Rae et al. [2004] (see Figure caption). Both the peak in the proton aurora and poleward boundary of the electron aurora have been extended along lines of constant geomagnetic latitude to guide the eye and for reference to auroral forms in the FSIM ASI. At 07:17:30 UT, Figure 3.2a, the proton aurora reaches its minimum latitude, characteristic of the maximum stretching in

the magnetotail and end of the growth phase. The yellow triangle marks the location of G11 traced magnetically to the northern hemisphere using T96 [Tsyganenko, 1995]. Figure 3.2b depicts auroral onset at 07:18:30 UT in the lower part of the FSIM ASI at 66° CGM latitude, which corresponds to the first brightening of the equatorward arc clearly occurring on closed field lines equatorward of the OCFLB. Note that no poleward auroral streamers [Nakamura et al., 2001] are seen within 6 hours of magnetic local time surrounding onset. Figure 3.2c shows the aurora at the time G11 observes a localised decrease in the magnetic field strength and Figure 3.2d depicts auroral breakup at 07:25:30 UT.

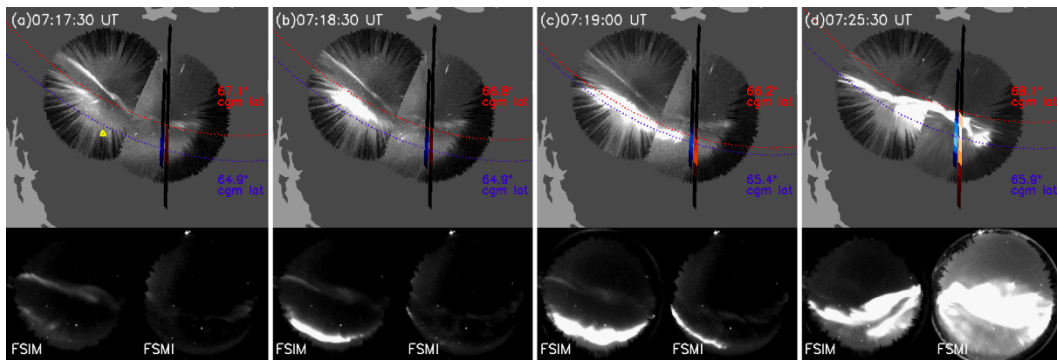


Figure 3.2: Auroral dynamics between 07:17:30-07:25:30 UT as observed by the FSIM (left) and FSMI (right) ASI and FSMI MSP. Top panel in each figure shows the mapped ASI data and the proton (blue) and electron (red) aurora from the FSMI MSP. The dotted blue line is a contour of constant CGM latitude at the peak in the proton aurora. The dotted red line marks the poleward edge of the electron aurora at constant CGM latitude. The poleward edge is determined by fitting the electron aurora intensity as a function of latitude to the functional form  $f(x) = A_0 \exp\left(\frac{-1}{2} \times \left(\frac{x-A_1}{A_2}\right)^2\right)$ . The poleward boarder is then defined as  $A1+1.5A2$  [Rae et al. 2004]. The bottom two images in each panel show the unmapped FSIM (left) and FSMI (right) ASI data. The yellow triangle in panel (a) marks the T96 traced north magnetic foot print of G11.

Figure 3.3 shows the evolution of the FACs (red and blue shading) derived from AMPERE during available ten minute quasi-stationary periods and ground magnetometer derived ionospheric ECs from each station, interpolated onto a regular grid (green and purple arrows respectively). A high latitude eastward electrojet in the dusk sector and lower latitude westward electrojet in the pre-midnight sector is apparent during the growth phase in Figure 3.3a in addition to an upward FAC system in the pre-midnight sector at  $\sim 70^\circ$  CGM latitude and a downward FAC system just equatorward. As the growth phase progresses an enhancement in the eastward and westward electrojets [McPherron et al., 1973] and upward and downward FACs are observed, Figure 3.3b. Just prior to

auroral onset, Figure 3.3c, a localised decrease in the ionospheric ECs and AMPERE FAC system is observed in a region coincident with the subsequent auroral onset (green diamond). The perpendicular ionospheric EC do not appear to change significantly in the night-side regions of the dawn and dusk convection cells. However, local to the subsequent onset region the perpendicular ground magnetic perturbations are smaller at this time. Finally, following auroral onset, Figure 3.3d shows a clear and strong enhancement of the ionospheric ECs and the development of a complicated system of upward and downward FAC sheets spanning from 20 MLT to 2 MLT. Although more complex in detail, this FAC structure is likely related to the SCW [Murphy et al., 2011] and will be discussed in detail in a separate Chapter.

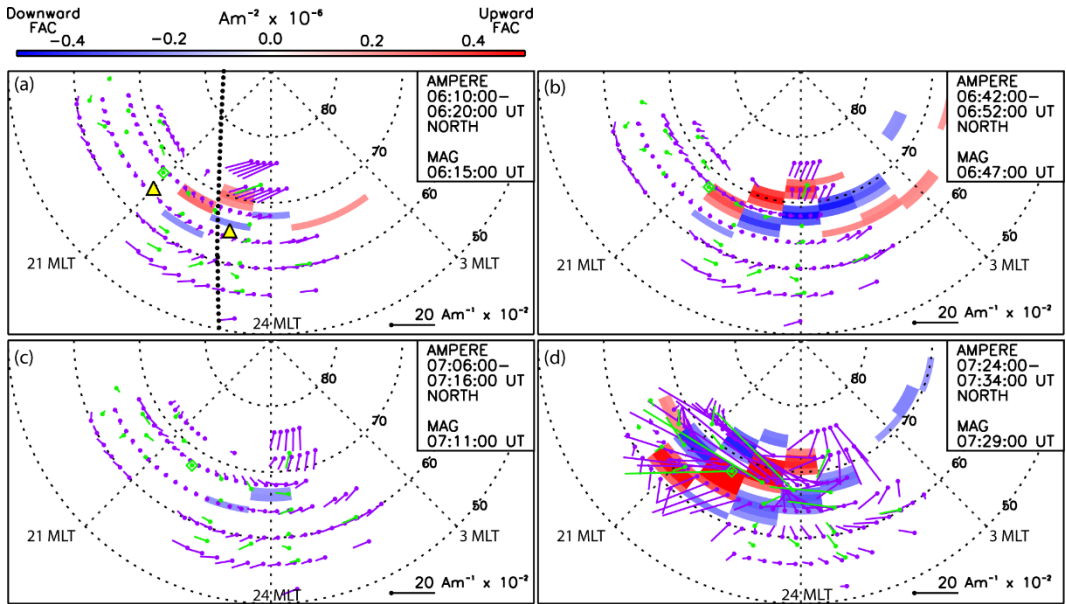


Figure 3.3: The derived AMPERE FACs (red, upward and blue, downward) between 19 and 5 MLT during select ten minute quasi-stationary time periods and ground-based ECs at each station and interpolated onto a constant grid (green and purple, respectively) at the centre of each quasi-stationary period. The yellow triangles in (a) mark the location of G11 (west) and G14 (east) and the black circles denote the trajectory of a single AMPERE orbital track in the pre-midnight sector (~23 MLT). The green triangle in each panel marks the location of the FSIM ASI and magnetometer where auroral onset is observed.

Figure 3.4 is a stack plot of the AMPERE geomagnetic North-South (N-S) and East-West (E-W) magnetic field perturbations (a) from the pre-midnight orbital track (dots in Figure 3.3a) that corresponds closely to the MLT of auroral onset, together with the derived FACs at 23 MLT (b) the FSIM ASI keogram (c) and magnetometer (d) observations as well as the summed auroral intensity from the Gillam (GILL), FSIM and FSIM ASIs (e). The

dashed line at 07:18:30 UT and solid line at 66° mark the auroral onset time and geomagnetic latitude, respectively. A clear decrease in the magnetic field perturbations is evident in the pre-midnight AMPERE track at 07:12 UT at the latitude of auroral onset. Between 07:02-07:12 UT (the time between AMPERE passes) the distinctly eastward magnetic field feature between 63°-68° CGM latitude disappears. Similar to the pre-midnight AMPERE track the derived AMPERE FACs in Figure 3.4b show a clear decrease in the FAC strength prior to auroral onset. The asterisks in Figure 3.4b mark the end of the select quasi-stationary 10 minute intervals shown in Figure 3.3, and the change in the FACs between these points is consistent with the overall conclusion that the FACs are reduced immediately prior to onset. Note in panel (b) that large increases in the FACs following onset are only evident once the next AMPERE satellite along the 23 MLT track traverses the onset region, approximately ten minutes later. Evident in the ASI keogram and summed ASI intensities is the formation of an equatorward arc which propagates west (GILL to FSMI to FSIM) and dims at FSIM minutes prior to auroral onset. As the equatorward auroral arc forms at FSIM the observed magnetic field begins to diverge; a positive deflection is observed in the D- and Z-components and a negative deflection is seen in the H-component, consistent with a change in local field aligned and ionospheric currents. Interestingly, at the time of the arc dimming a second change in the magnetic field is seen in the FSIM magnetometer data, especially in the D- and Z-components.

Two additional substorms observed on 24 March 2011 08:26:30 UT at the FSIM ASI and 16 May 2011 08:25:30 UT at The Pas ASI (see Figure 3.5) also show a clear reduction in the AMPERE derived FACs in a region local to and preceding auroral onset. Significantly, the reduction in AMPERE FAC prior to auroral onset and at the same location suggests that there may be a role for M-I coupling in preconditioning the inner magnetosphere prior to auroral substorm onset.

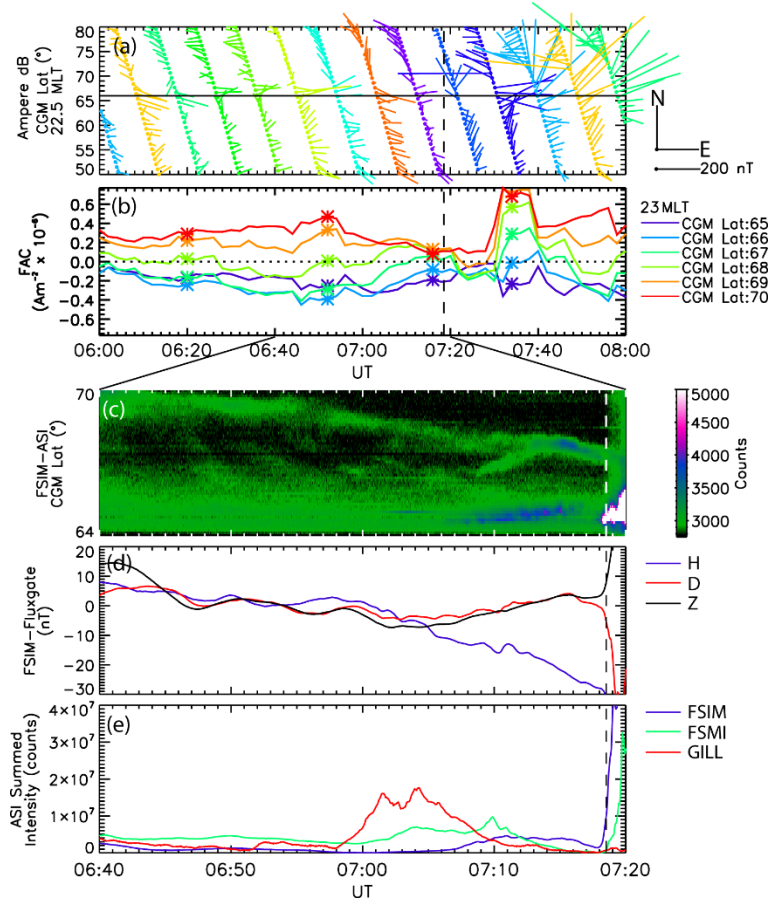


Figure 3.4: (a) The AMPERE geomagnetic N-S and E-W magnetic field perturbations at 1 minute resolution from the pre-midnight orbital track (c.f. Figure 3(a)); the horizontal line marks the geomagnetic latitude of auroral onset at 66° CGM latitude. The vertical line in each panel marks auroral onset at 07:18:30 UT. (b) The AMPERE derived FACs in the auroral onset region at 23 MLT and from 65°-70° CGM latitude. (c) FSIM ASI keogram. (d) FSIM H-, D-, and Z-component magnetic field (blue, red and black respectively). (e) Integrated auroral intensity from select ASIs.

### 3.4 Discussion and Conclusions

In this paper, we present detailed observations of an isolated substorm event on 16 February 2010. A clear growth phase is marked by the equatorward propagation of the auroral oval and a clear and localised brightening of the aurora on the most equatorward arc is observed at 07:18:30 UT in the FSIM ASI denoting auroral substorm onset. This brightening occurs on closed field lines in the inner magnetosphere near the transition between dipole and tail field lines [Samson et al., 1992] and coincident in time and closely conjugate with a decrease in the G11 geosynchronous magnetic field. No poleward auroral activations, such as the north-south auroral streamers described for example by Nakamura et al. [2001], are observed prior to this onset and thus there is no

clear evidence in the THEMIS white light ASI data to suggest such distant magnetotail activity immediately precedes the auroral onset depicted in Figure 3.2b [c.f. Nishimura et al., 2010].

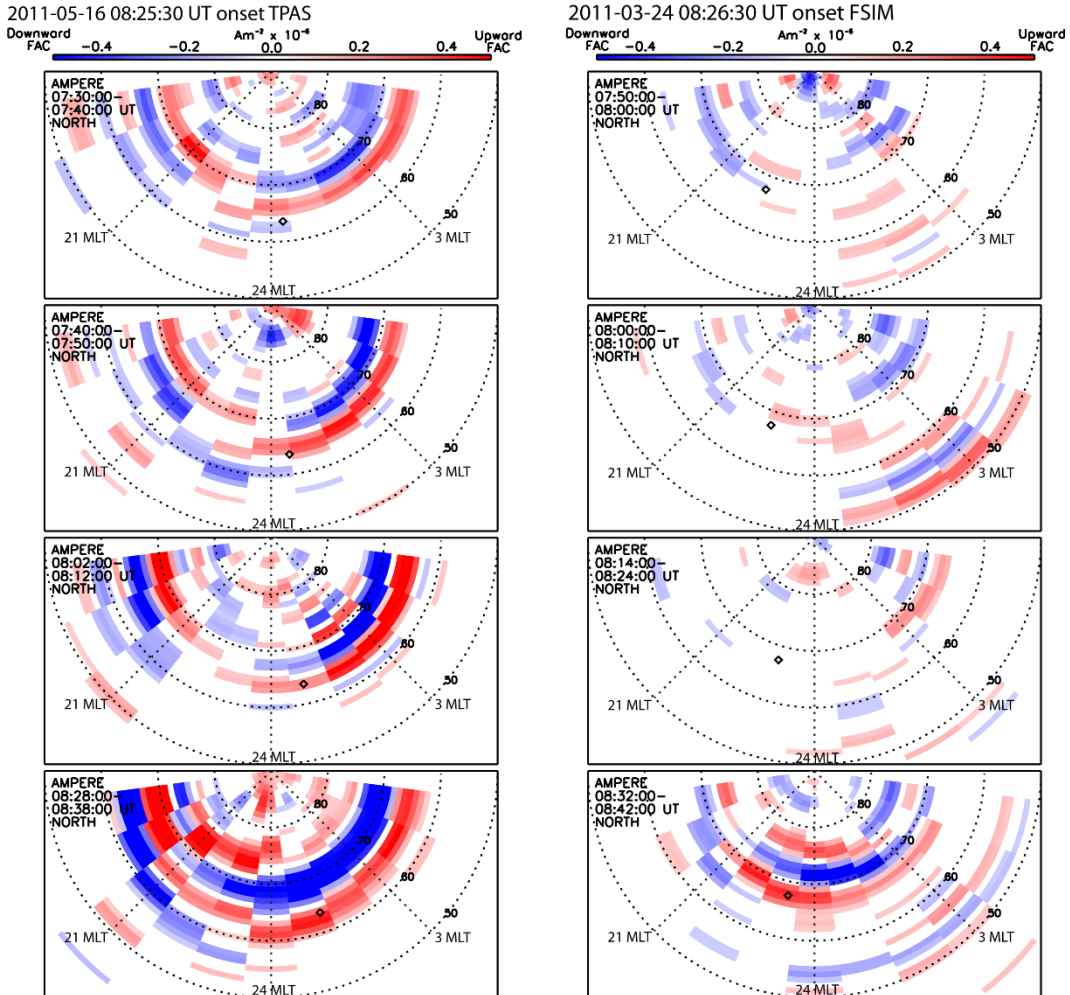


Figure 3.5: Derived FACs (red, upward and blue downward) for select times from substorms observed on 16 May 2011 (left) and 3 March 2011 (right). The diamond in each panel marks the location of the ASI in which the auroral onset was identified. On 16 May 2011 auroral onset was observed by the TPAS ASI at 08:25:30 UT and on 24 March 2011 auroral onset was observed by the FSIM ASI at 08:26:30 UT. Both events show a clear and localised decrease in the strength of the FACs just prior to auroral onset (row three of both columns).

However, there is a distinct change in the FACs observed by both AMPERE and ground-derived ionospheric ECs at the end of the substorm growth phase. The AMPERE FACs show a significant reduction in a region coincident with auroral onset and the pre-midnight AMPERE track shows a clear reduction in the N-S and E-W magnetic field perturbations between 07:06-07:12 UT. Coincident in both time and space with this FAC

reduction is the formation and westward propagation of a newly formed equatorward arc. Shortly thereafter, the equatorward arc dims such that the intensity of the auroral emissions along the entire arc in the field of view of the FSIM camera is clearly reduced on the ~1-2 minute time scales observed by Pellinen and Heikkila [1978]. Subsequently, the same arc then brightens and begins to move poleward at 07:18:30 UT characterising the beginning of the auroral onset in the same region which is precisely local to the prior reduction in FACs. During this entire period both the solar wind Bz and vx (GSM) remain nearly constant and the day-side FAC system (not shown) undergoes little change. Additionally, the westward electrojet continues to enhance for the entire duration of the growth phase. Thus it is unlikely that the change in the night-side FAC and ionospheric EC systems local to the auroral onset region occurs as the result of changes in large scale magnetospheric convection. More likely, there is a change in a localised region of the pre-midnight inner magnetotail which influences the processes leading to auroral substorm onset. We contend that the localised night-side reduction in FACs is the result of a change in magnetosphere-ionosphere coupling in a region conjugate to auroral onset. Determining how changes in magnetospheric and/or ionospheric processes and morphology lead to this FAC reduction and its potential role in the release of energy during onset is critical for understanding substorm onset.

Localised reductions in the in-situ magnetic field are observed by AMPERE at least 6.5 minutes (and perhaps as long as 16.5 minutes) prior to auroral onset consistent with the reduction in FACs inferred by AMPERE during the same time period. This clearly demonstrates that there is a significant change in M-I coupling that precedes substorm onset. Certainly in this event, our observations clearly indicate that M-I coupling played a very significant role in the substorm onset process, perhaps by preconditioning the system prior to onset [c.f., Milan et al., 2010]. The exact role of this magnetosphere-ionosphere coupling process local to the onset remains to be determined. However, it is clear from these observations that any substorm model or paradigm must address the localised reduction in M-I coupling prior to onset within its framework. For example, perhaps the change in M-I coupling is responsible for the localised auroral dimming prior to onset [Pellinen and Heikkila, 1978] which subsequently leads to a destabilization of local near-Earth plasmashet instabilities such as cross-tail current disruption [Lui, 1996] or ballooning at the edge of the equatorial plasma sheet [e.g., Roux 1985; Samson

et al., 1996] leading to onset, or perhaps onset occurs as a result of the near-Earth geophysical onset (NGO) mechanism as described by Maynard et al. [1996]. The local reduction in magnetic field magnitude at onset seen at G11 may be very significant since it could be consistent with both the CD and NGO models as described for example by Ohtani [1998] and Erickson et al. [2000], respectively.

The fact that the FAC reduction only occurs in a localised region, local to and 6.5 minutes before the subsequent auroral onset has important ramifications for the substorm paradigm. Our observations on 16 February 2010 (as well as those on 24 March 2011 and 16 May 2011, c.f., Figure 3.5) clearly demonstrate the necessity of including the role of M-I coupling processes in the minutes preceding auroral onset in any substorm onset mechanism. Indeed these FAC changes could potentially be mediated via the exchange of Alfvén waves between the magnetosphere and ionosphere and therefore could represent a critical component of the onset process. In that case, not only would M-I coupling play a role in selecting the subsequent auroral onset location, but also the FAC could provide a basis for diagnosing the magnetospheric processes which must explain the well-known Akasofu sequence of auroral onset morphology in the ionosphere.

### **3.5 References**

- Akasofu, S. I. (1964), The development of the auroral substorm, *Planet. Space Sci.*, 273-282.
- Akasofu, S.-I., (1977) *Physics of Magnetospheric Substorms*, p. 274, D. Reidel, Hingham, Mass.
- Anderson, B. J. et al. (2000), Sensing global Birkeland currents with iridium® engineering magnetometer data, *Geophys. Res. Lett.*, doi:10.1029/2000GL000094.
- Angelopoulos, V., et al. (2008), Tail reconnection triggering substorm onset, *Science*, doi:10.1126/science.1160495.
- Angelopoulos, V., et al. (2009), Response to comment on “Tail reconnection triggering substorm onset,” *Science*, doi:10.1126/science. 1168045.

- Baker, D. N., et al. (1996), Neutral line model of substorms: Past results and present view, *J. Geophys. Res.*, 101(A6), 12975-13010.
- Blanchard, G. T. et al. (1995), Locating the Polar Cap Boundary from Observations of 6300 Å Auroral Emission, *J. Geophys. Res.*, doi:10.1029/94JA02631.
- Clauer, R. C., and R. L. McPherron (1974), Mapping the Local Time-Universal Time Development of Magnetospheric Substorms Using Mid-Latitude Magnetic Observations, *J. Geophys. Res.*, 2811-2820.
- Donovan, E. F. et al. (2003), All-sky imaging within the Canadian CANOPUS and NORSTAR projects, *Sodankyla Geophys. Obs. Publ.*, 92, 109–112.
- Erickson, G. M., et al. (2000), Electromagnetics of substorm onsets in the near geosynchronous plasma sheet, *J. Geophys. Res.*, doi:10.1029/1999JA000424.
- Huba, J. D., et al. (1977), The lower-hybrid-drift instability as a source of anomalous resistivity for magnetic field line reconnection, *Geophys. Res. Lett.*, 4, 125-128.
- King, J. H., and N. E. Papitashvili (2005), Solar wind spatial scales in and comparisons of hourly Wind and ACE plasma and magnetic field data, *J. Geophys. Res.*, doi:10.1029/2004JA010649.
- Lühr, H., and K. Schlegel (1994), Combined Measurements of EISCAT and the EISCAT Magnetometer Cross to Study  $\Omega$  Bands, *J. Geophys. Res.*, 99(A5), 8951–8959.
- Lui, A. T. Y., et al. (1995), Preliminary nonlocal analysis of cross-field current instability for substorm expansion onset, *J. Geophys. Res.*, 100, 19147-19154.
- Lui, A. T. Y. (1996), Current disruption in the Earth's magnetosphere: Observations and models, *J. Geophys. Res.*, 101, 13067-13088.
- Lui, A. T. Y. (2009), Comment on “Tail reconnection triggering substorm onset” *Science*, 324(5933), doi:10.1126/science.1167726.
- Mann, I. R., et al. (2008), The Upgraded CARISMA Magnetometer Array in the THEMIS Era, *Space Sci. Rev.*, 141, 413-451.

- Maynard, N. C. et al. (1996), Dynamics of the inner magnetosphere near times of substorm onsets, *J. Geophys. Res.*, doi:10.1029/95JA03856.
- McPherron, R. L. (1979), Magnetospheric Substorms, *Rev. Geophys. Space Phys.*, 17, 657-681.
- McPherron, R. L. et al. (1973) Substorms in space: The correlation between ground and satellite observations of the magnetic field, *Radio Sci.*, 8-11,1059-1076.
- Mende, S., et al. (2008), The THEMIS array of ground based observatories for the study of auroral substorms, *Space Sci. Rev.*, doi: 10.1007/s11214-008-9380-x.
- Milan, S. E., et al. (2010), A superposed epoch analysis of auroral evolution during substorms: Local time of onset region, *J. Geophys. Res.*, 115, A00I04, doi:10.1029/2010JA015663.
- Murphy, K. R., et al. (2011), A multi-point and multi-instrument characterisation of the formation and evolution of the substorm current wedge, Abstract SM54A-04 presented at 2011 Fall Meeting, AGU, San Francisco, Calif., 5-9 Dec.
- Nakamura, R., et al. (2001), Earthward flow bursts, auroral streamers, and small expansions, *J. Geophys. Res.*, doi:10.1029/2000JA000306.
- Nishimura, Y., et al. (2010), Substorm triggering by new plasma intrusion: THEMIS all-sky imager observations, *J. Geophys. Res.*, doi:10.1029/2009JA015166.
- Ohtani, S. (1998), Earthward expansion of tail current disruption: Dual-satellite study, *J. Geophys. Res.*, doi:10.1029/98JA00013.
- Pellinen, R. J., and W. J. Heikkila (1978), Observations of Auroral Fading Before Breakup, *J. Geophys. Res.*, 83(A9), 4207–4217, doi:10.1029/JA083iA09p04207.
- Rae, I. J. et al. (2004), Comparison of photometer and global MHD determination of the open-closed field line boundary, *J. Geophys. Res.*, doi:10.1029/2003JA009968.
- Rae, I. J., et al. (2010), Optical characterization of the growth and spatial structure of a substorm onset arc, *J. Geophys. Res.*, doi:10.1029/2010JA015376.

- Russell, C. T., et al. (2008), THEMIS Ground-based Magnetometers, *Space Sci. Rev.*, 141, 389-412.
- Roux, A., et al. (1991), Plasma sheet instability related to the westward travelling surge, *J. Geophys. Res.*, 96, 17697-17714.
- Samson, J. C., et al. (1992), Proton aurora and substorm intensifications, *Geophys. Res. Lett.*, doi:10.1029/92GL02184.
- Samson, J. C., et al. (1996), Substorm intensifications and resistive shear flow-ballooning instabilities in the near-Earth magnetotail, in *Proc third International Conference on Substorms (ICS-3)*, ESA SP-389, 399.
- Singer, H. J., et al. (1996), Monitoring space weather with the GOES magnetometers, *SPIE Conf. Proc.*, 2812, 299–308.
- Song, Y., and R. L. Lysak (2001), Towards a new paradigm: From a quasisteady description to a dynamical description of the magnetosphere, *Space Sci. Rev.*, 95, 273–292.
- Tsyganenko, N. A. (1995), Modeling the Earth's magnetospheric magnetic field confined within a realistic magnetopause, *J. Geophys. Res.*, doi:10.1029/94JA03193.
- Waters, C. L. et al. (2001), Estimation of global field aligned currents using the iridium® System magnetometer data, *Geophys. Res. Lett.*, doi:10.1029/2000GL012725.

## Chapter 4 The detailed spatial structure of field aligned currents comprising the substorm current wedge<sup>3</sup>

### 4.1 Introduction

The substorm current wedge is an integral feature of the substorm expansion phase [McPherron et al., 1973]. Following auroral substorm onset [Akasofu, 1964], the night-side magnetotail dipolarizes [Cummings et al., 1968] and the westward electrojet enhances [Rostoker et al., 1975] leading to the formation of current systems in the ionosphere and magnetosphere which are known as the substorm current wedge (SCW). Typically the SCW is viewed as an equivalent line current system consisting of a downward field-aligned current (FAC) in the east, an enhanced westward electrojet and an upward FAC in the west [McPherron et al., 1973; Clauer and McPherron, 1974; Yao et al., 2012], although significant deviations from this line current have been proposed [e.g., Birn et al., 1999].

Two-dimensional statistical views of the upward and downward FAC topology during substorms were originally compiled by Iijima and Potemra [1978] using magnetometer data from single satellite passes of the Triad satellite, situated in a low-altitude 90 minute polar orbit. These authors demonstrated that enhanced region 1 and region 2 current systems [Iijima and Potemra, 1976; Iijima and Potemra 1978] contributed to the large scale FAC currents associated with substorms. However, for individual events Iijima and Potemra [1978] noted that small scale current structures not observed in the statistical schematic were superimposed on the larger scale region 1 and 2 current systems. They also reported that during larger events (large auroral electrojet index, AE) a more complex pattern of FACs existed near the edge of the enhanced westward electrojet, being more structured than the typical non-substorm time region 1 and region 2 current systems. This more complicated current system was thought to be comprised of an upward FAC surrounded by downward FACs to the north and south. A

---

<sup>3</sup> A version of this chapter has been submitted for publication to the *Journal of Geophysical Research*. Murphy, K. R. et al. (2011), submission number 2013JA18979.

similar FAC topology was also observed by Rostoker et al., [1975] utilising the Triad satellite magnetometer.

In general, statistical studies of FACs compiled from single satellites can only develop an average picture of the large scale and predominant FACs which couple the ionosphere and magnetosphere. By their very nature, statistical studies smooth over fine scale structures in the FAC topology. This smoothing out of the fine structure of FACs is important when considering the spatial and temporal variability of these currents through the substorm growth and expansion phase. More importantly, the assumption needed to infer FACs from single satellite measurements is often invalid [Peria et al., 2000] leading to erroneous results, both in terms of the inferred FAC magnitude, but more importantly, FAC direction [Zheng et al., 2003]. Specifically, single spacecraft magnetometer measurements are subject to a space-time ambiguity which introduces an uncertainty into any derived FAC which can only be avoided utilising multi-spacecraft measurements [Peria et al., 2000].

In this paper we use detailed multi-spacecraft estimates of FACs from the Iridium constellation of satellites and the Active Magnetosphere and Planetary Electrodynamics Response Experiment (AMPERE) [Anderson et al., 2000; Waters et al., 2001] to develop a comprehensive two-dimensional view of the FACs preceding substorm onset and the structure of the FACs comprising the SCW during the expansion phase. To date, the multi-spacecraft Iridium constellation and AMPERE provide the most comprehensive view of the FAC systems comprising the SCW. In this paper we exploit this in order to establish both the two-dimensional topology and the temporal evolution of these FACs through substorm onset. Such structure was previously unknown as this fine scale structure was not detectable using single satellite measurements. Further, we supplement the AMPERE FACs with auroral observations provided by the Time History of Events and Macroscale Interaction During Substorms (THEMIS) all-sky imagers (ASIs; Mende et al., 2008) and ground-based magnetic field observations from the Canadian Array for Realtime Investigations of Magnetic Activity (CARISMA; Mann et al., 2008) and THEMIS magnetometer arrays [Russell et al., 2008]. Using these combined data sets we demonstrate that the FACs associated with the SCW are highly structured and filamented with discrete regions of both upward and downward FACs spanning up to 8

hours of MLT on the night-side. When spatially averaged (as a function of MLT) these discrete regions of upward and downward FACs resemble the equivalent line current system of the SCW described for example by McPherron et al. [1973]. Finally, using the AMPERE data we are able to confirm that regions of upward FAC are typically associated with discrete auroral forms.

## **4.2 Instrumentation**

Multi-point observations of the magnetic field are required in order to separate the spatial variations from the temporal fluctuations of the current systems coupling the ionosphere and magnetosphere. Specifically, a multi-spacecraft study is capable of identifying quasi-stationary time periods during which temporal changes in the magnetic field can be neglected. When estimating FAC densities this enables the validation of the assumption that variations in the magnetic field along a spacecraft trajectory can be interpreted as spatial variations and hence be used as an estimate for the curl of the magnetic field for determining FAC structure.

AMPERE utilises over seventy spacecraft as part of the Iridium constellation to infer the global structure of FACs from vector measurements of the magnetic field at a twenty second cadence [Anderson et al., 2000; Waters et al 2001]. The Iridium satellites are distributed in 6 circular orbital planes at an altitude of ~780 km and a nominal separation of 4 hours of local time. Utilising the entire Iridium constellation of satellites AMPERE is able to determine the FAC topology in both the southern and northern hemispheres in ten minute intervals, the time required for the constellation to sample the entire northern or southern hemisphere. The on-board magnetometers have a temporal resolution of 20 seconds and a noise level on the order of 10 nT. The FAC maps derived from fitted magnetic field data on ten minute intervals. These maps have a spatial resolution in geomagnetic coordinates of 1° in latitude and 1 hour of magnetic local time (MLT; 15° in longitude) a temporal resolution of two minutes (by sliding the ten minute window each two minutes), and FAC resolution of ~0.1  $\mu\text{A}$  (FAC amplitudes below this value or set to zero) [Anderson et al., 2000; Waters et al., 2001; Murphy et al., 2012]. Note that the 6 orbital planes do not pass directly over the North Pole and precess with time such that nominal resolution in MLT can vary between approximately 1 and 3 hours.

In addition to FAC estimates provided by AMPERE, ground-based observations of the aurora and magnetic field perturbations during the substorm expansion phase provide complementary observations with which to infer the topology of ionospheric current systems. The THEMIS ASIs provided detailed observations of the aurora through the substorm expansion phase at three second cadence and measure auroral intensity as a function of counts [Mende et al., 2008]. In this particular study we utilise the NORSTAR meridian scanning photometers (MSPs) to determine substorm onset times [Donovan et al., 2003] at times when ASI observations of the aurora were not available. The MSPs have a 30s cadence and measure auroral intensity in counts.

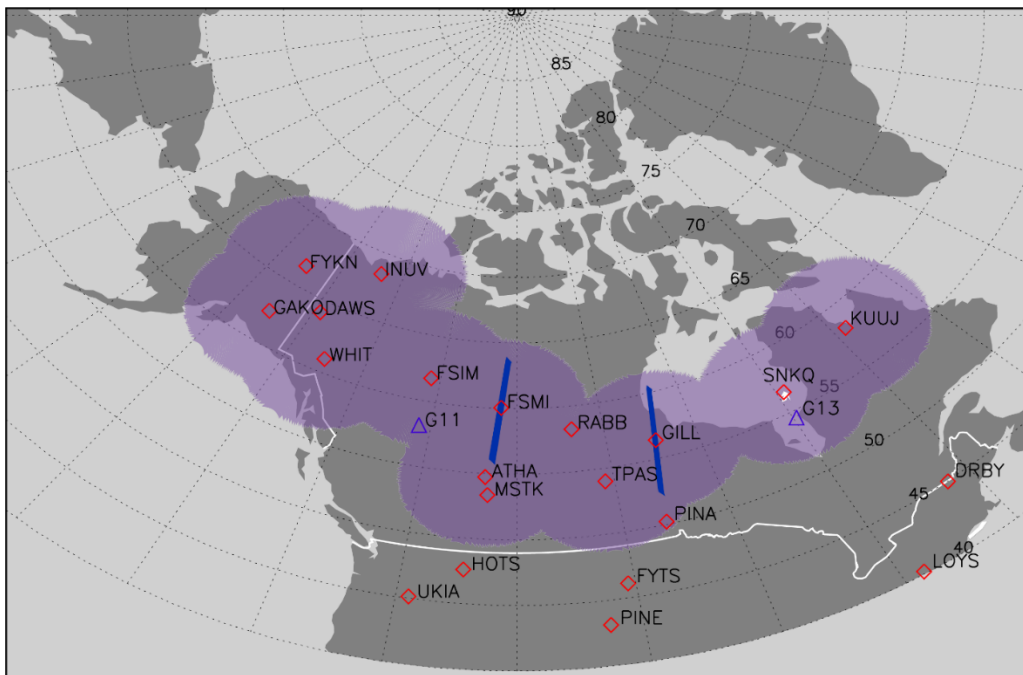


Figure 4.1: The location of ground-based magnetometers (diamonds), ASI and MSP fields-of-view (purple and blue respectively). The north magnetic footprints of G11 and G13 are marked by blue triangles.

Ground-based magnetometers can also be used to infer the location of regions of net upward and downward FAC in the ionosphere and the location and direction of ionospheric electrojets [Clauer and McPherron, 1974]. In this study we use auroral zone and low-latitude magnetometer data from the THEMIS [Russell et al., 2008] and CARISMA [Mann et al., 2008] magnetometer arrays to infer the azimuthal extent of the SCW and location of the upward and downward FAC elements [c.f., Lester et al., 1983 and Smith et al., 2002]. Ground-based magnetic field measurements are further

supplemented by geosynchronous magnetic field measurements from GOES 11 and GOES 13 (G11 and G13) [Singer et al., 1996]. Figure 4.1 shows the locations of the ground-based magnetometers, the fields-of-view of the ASIs and MSPs mapped to an altitude of 110 km used in this study and the north magnetic foot-prints of G11 and G13 traced with the T96 magnetic field model [Tsyganenko, 1995].

### **4.3 Observations**

In this section we use three substorm case studies to characterise the development of the ionospheric currents and FAC systems coupling the ionosphere and magnetosphere through the substorm growth and expansion phases. Using data from the THEMIS ASIs, and for one case the NORSTAR MSPs, to define auroral substorm onset we characterise the FAC topology associated with the SCW as inferred by AMPERE and develop a comprehensive two-dimensional view of the SCW. In addition we demonstrate that regions of upward FAC are consistently associated with discrete auroral forms as viewed by the THEMIS ASIs and the azimuthal extent of the SCW inferred from AMPERE is consistent with ground-based magnetometer observations.

#### **4.3.1 The 16 February 2010 Event**

Figure 4.2 is an overview of an isolated substorm observed on 16 February 2010 from geosynchronous orbit (panel a), three ground-based CARISMA magnetometers mapping to near geosynchronous L-shells (panels b-d), and the THEMIS Fort Simpson (FSIM) ASI (panel e). The FAC structure prior and local to the auroral onset region of this substorm was previously characterised in Murphy et al. [2012]. In this manuscript we concentrate on the development of FACs following substorm onset and the structure of the SCW formed in the expansion phase rather than the evolution of the FACs and sequence of events leading to substorm onset. A clear dipolarisation of the magnetic field is observed at 07:25 UT characterised by the sharp increase in the magnetic field strength (red) and inclination angle (the angle between the equatorial plane and the magnetic field vector; blue) of the geosynchronous magnetic field. Prior to the dipolarisation a sharp decrease in the geosynchronous magnetic field is observed coincident with the formation of ground magnetic bays and auroral onset at 07:18:30 UT bottom panels of Figure 4.2. Figure 4.2 (b-d) shows the north-south (H, blue), east-west (D, red) and vertical (Z, black) magnetic field perturbations from the Dawson City (DAWS), FSIM and

Fort Smith (FSMI) ground-based magnetometers, respectively. The magnetometers show a typical substorm response including the formation of magnetic bays [Kisabeth and Rostoker, 1971] and onset of large amplitude ultra-low frequency waves [Olson, 1999] associated with the substorm expansion phase and formation of the SCW. The largest bay structure is observed by the FSIM magnetometer closest to the auroral onset as illustrated by the FSIM ASI keogram (panel e).

The FSIM keogram (panel e) was created by taking a slice through the FSIM ASI image perpendicular to the growth phase arc and in the local time sector of auroral onset. The resulting keogram shows a clear equatorward-propagating auroral arc typical of the growth phase [Akasofu 1964]. Just prior to onset a new equatorward arc formed at 07:06 UT, which briefly faded and finally brightened and expanded poleward at 07:18:30 UT, marking the onset of the substorm [c.f. Murphy et al., 2012].

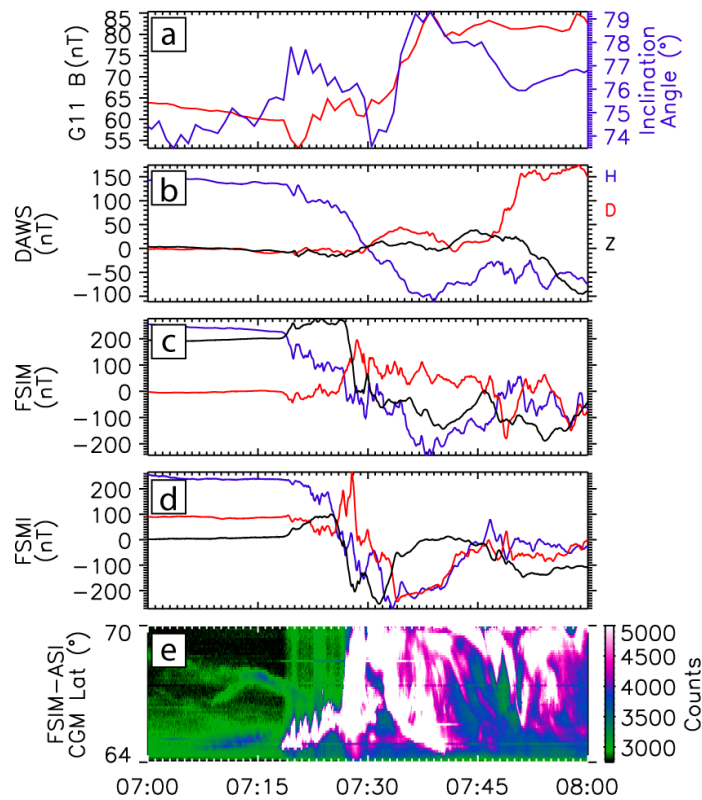


Figure 4.2: Summary of geosynchronous and ground-based observations for the 16 February 2010 substorm. (a) G11 total magnetic field (red) and inclination angle (blue). (b-d) H (blue), D (red), and Z (black) magnetic field variations from the DAWS, FSIM, and FSMI ground-based magnetometers, respectively. (e) FSIM keogram from the THEMIS ASI; the keogram is constructed from a slice through the ASI perpendicular to the growth phase arc and in the MLT sector of auroral onset.

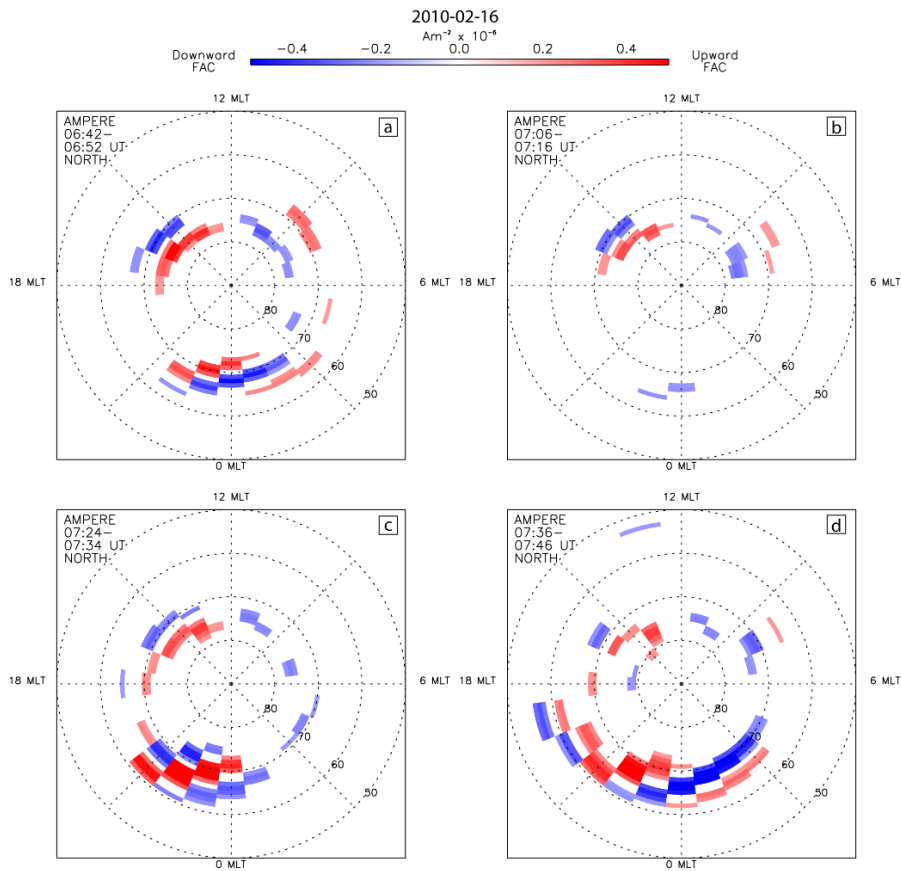


Figure 4.3: AMPERE derived FACs for 16 February 2010 during selected ten minute time periods. Red denotes upward FAC and blue denotes downward FAC. The FACs are plotted as a function of corrected geomagnetic latitude and magnetic local time with noon towards the top and midnight towards the bottom.

Figure 4.3 shows the evolution of the day- and night-side FAC densities through the substorm growth and expansion phases as observed by AMPERE at four selected ten minute quasi-stationary time periods. As detailed in the previous section, sequential passes from satellites in the Iridium constellation allows quasi-stationary time periods in the magnetic field data to be identified. During these periods we assume that any changes in the magnetic field represent spatial variations and thus can be used to determine the curl of the magnetic field required to infer FACs. Each panel of Figure 4.3 is plotted in magnetic local time (MLT) and corrected geomagnetic (CGM) latitude coordinates with noon at the top and midnight at the bottom. Red denotes upward FAC and blue denotes downward FAC. Between 0642-0652 UT shown in Figure 4.3a, AMPERE shows evidence of the day- and night-side region 1 and region 2 current systems [c.f., Iijima and Potemra, 1978]. Just prior to onset, at 07:06-07:16 UT shown in Figure 4.3b,

the night-side region 1 and 2 current systems are significantly reduced [c.f., Murphy et al., 2012] while the day-side region 1 and region 2 current systems remain relatively unchanged. Following auroral onset, the 07:24-07:34 UT and 07:36-07:46 UT frames, Figure 4.3 (c) and (d) respectively, show the development of structured upward and downward FACs between 60-75° CGM latitude. Initially, at 07:24-07:34 UT and shown in Figure 4.3c, the FAC elements form in the region of auroral onset, around 23 MLT and 68° CGM latitude, and subsequently, 0736-0746 UT Figure 4.3d, expand azimuthally to span about 10 hours of MLT.

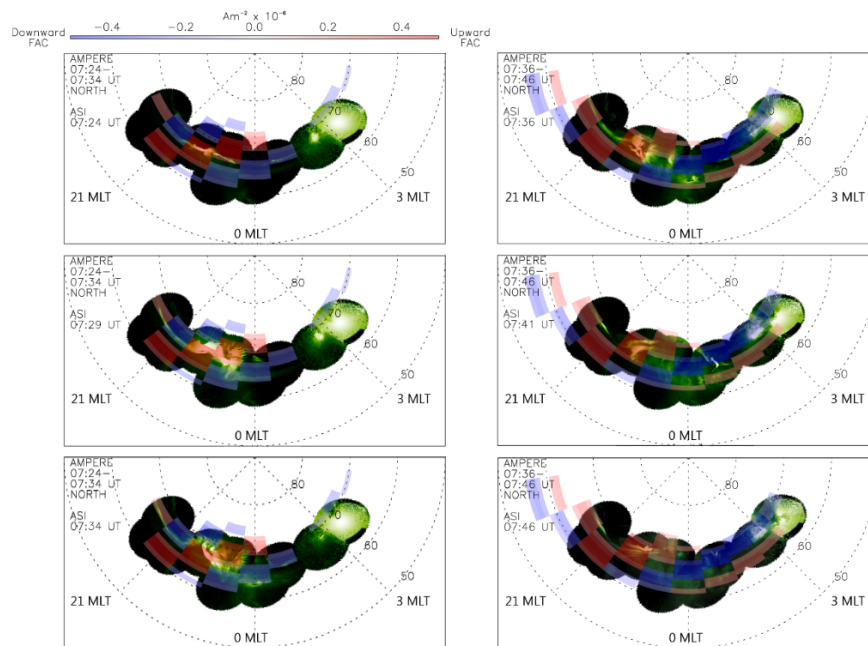


Figure 4.4: A superposition of the THEMIS ASI aurora observations and night-side FACs during the substorm expansion phase on 16 February 2010. The left panel denotes the initial enhancement of the FAC system between 07:24-07:34 UT and the right panel the subsequent evolution of the FAC system between 07:36-07:46. In each column the three rows overplot the aurora at the beginning, middle, and end of the ten minute window encompassing the AMPERE derived FACs (top, middle and bottom rows, respectively).

Figure 4.4 shows the AMPERE derived expansion phase FAC system between 07:24-07:34 UT and 07:36-07:46 UT (left and right panels, respectively). Superimposed onto the FACs are the THEMIS ASI images at three select times: the beginning of the ten minute AMPERE window used to derive the FACs, the middle of the ten minute window and the end of the ten minute window (top, middle and bottom frames, respectively).

Note that even over a ten minute period within the substorm expansion phase, during which the westward travelling surge forms and the aurora is extremely dynamic, the aurora is largely coincident with the upward FAC (red) regions as inferred by AMPERE. Regions of downward FAC are conversely typically devoid of discrete auroral forms or encompass more diffuse aurora.

### **4.3.2 The 24 March 2011 Event**

Figure 4.5, in the same format as Figure 4.2, is an overview of the geosynchronous magnetic field and ground-based observations of a substorm on 24 March 2011. The top panel shows the geosynchronous magnetic field and inclination angle at G13. Panels (b-d) show the formation of the ground-based magnetic bays at DAWS, FSIM and FSMI following substorm onset at 08:26:30 UT as illustrated in the FSIM keogram, panel (e). Prior to auroral onset and the formation of the magnetic bays, the FSIM keogram shows clear evidence of the substorm growth phase. The growth phase arc propagates equatorward [Akasofu 1964] and just prior to onset the arc dims [Pellinen and Heikkila, 1978; Murphy et al., 2012] and then rapidly brightens and expands poleward characterising the substorm expansion phase [Akasofu, 1964]. The geosynchronous magnetic field at G13 is nearly dipolar and shows little evidence of a dipolarisation, although both the field strength and inclination angle increase following onset. The lack of dipolarisation is likely due to the large azimuthal distance between the G13 satellite and auroral onset at FSIM (situated  $\sim 3$  hours of MLT to the post-midnight sector from auroral onset, c.f. Figure 4.1). There is however evidence of ultra-low frequency (ULF) oscillations in both the G13 total magnetic field and the inclination angle following auroral onset likely in response to substorm expansion phase onset.

Figure 4.6 shows the evolution of the AMPERE derived FACs during three selected quasi-stationary ten minute time periods. The top and middle panels, 08:00-08:10 UT and 08:14-08:24 UT, respectively, show the AMPERE FAC topology prior to auroral onset and the bottom panel, 08:32-08:42 UT, illustrates the FAC topology following onset. Between 08:00-08:10 UT there is evidence of region 1 and region 2 current systems on the dawn-side flank between  $70^\circ$  and  $80^\circ$  CGM latitude. On the night-side and dusk-side flank the current systems are less well-organised and there is no principal region 1-2 current system as defined by Iijima and Potemra [1978]. The dawn-flank continues to

show evidence of the region 1 and region 2 current systems between 08:14-08:24 UT (panel b). Just prior to auroral onset at 08:26:30 UT, the data in the midnight sector from panel (b) shows evidence of a decrease in the FAC density. The night-side FAC reduction occurs between 22 and 2 MLT and 60°-80° CGM latitude and is observed in a region conjugate to the subsequent auroral onset at 66° CGM latitude and 22.8 MLT [c.f. Murphy et al., 2012]. Following auroral onset, 08:32-08:42 UT, there is a clear increase in the strength of both the day- and night-side currents during the substorm expansion phase.

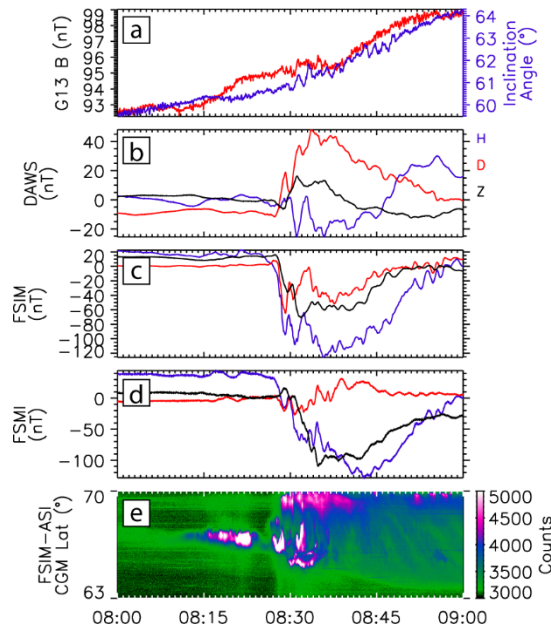


Figure 4.5: Summary of the geosynchronous magnetic field and ground-based magnetometer and ASI observations of a substorm on 24 March 2011. (a) The G13 total magnetic field (red) and inclination angle (blue). (b-c) DAWs, FSIM and FSIM magnetograms in the same format as Figure 2. (e) FSIM keogram in the same format as Figure 2.

Similar to the previous substorm, an enhanced region of structured upward and downward FACs form across midnight, following auroral onset, spanning about 22 MLT to nearly 4 MLT. Figure 4.7 highlights the relation between the aurora as observed by the THEMIS ASIs and the enhanced night-side current system forming during the substorm expansion phase. Similar to Figure 4.4 the ASI images are plotted with the AMPERE derived FAC at the beginning, middle and end of the ten minute AMPERE time window. Despite spanning a ten minute window, each panel shows remarkable correlation between regions of upward FAC and discrete aurora between 21 and 23 MLT

and  $\sim 65^\circ$ - $70^\circ$  CGM latitude. Similarly, the region of downward FAC, between 21-23 MLT and  $\sim 70^\circ$ - $75^\circ$  CGM latitude, is nearly devoid of aurora.

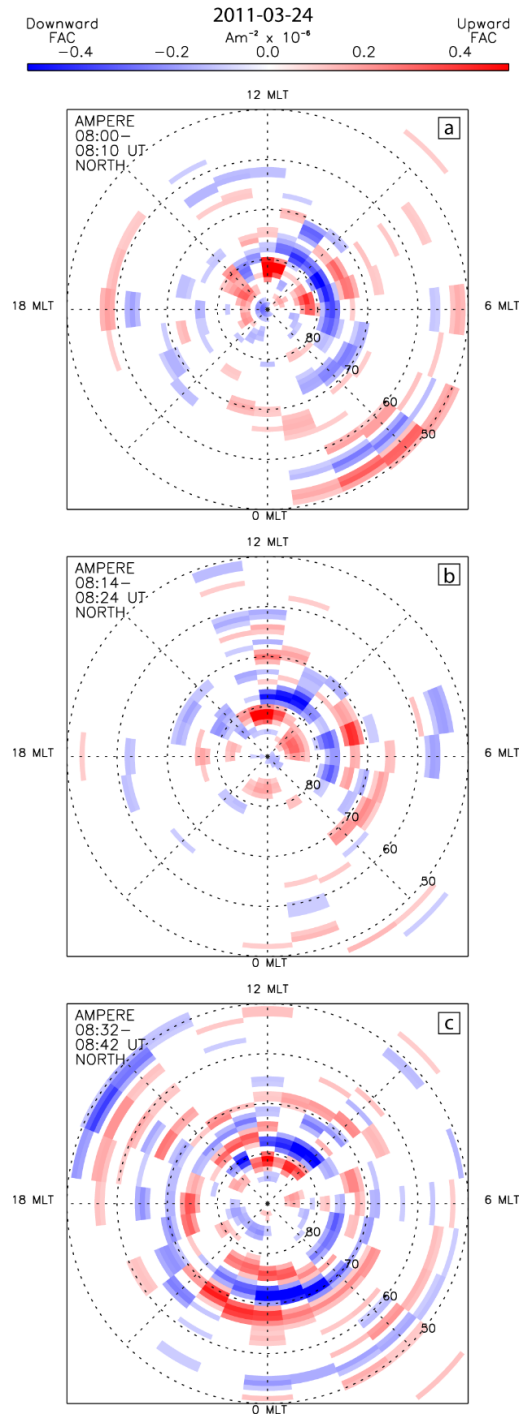


Figure 4.6: AMPERE derived FACs during three time periods for the 24 March 2011 substorm. Red denotes upward FAC and blue downward FAC.

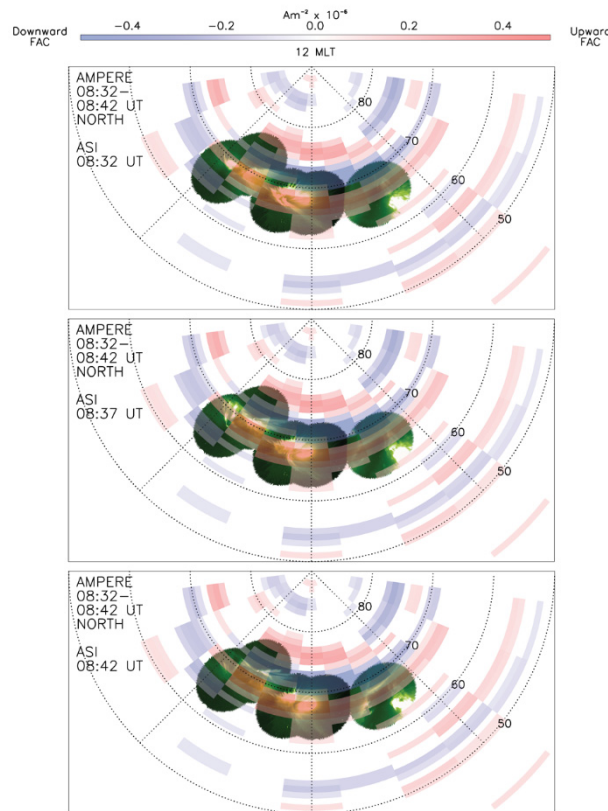


Figure 4.7: A superposition of the THEMIS ASI auroral observations and AMPERE derived FACs for the 24 March 2011 substorm between 08:32-08:42 UT in the same format as Figure 4.

### 4.3.3 The 16 May 2011 Event

Figure 4.8 shows a summary of the geosynchronous and ground-based magnetic fields and auroral observations of a substorm on 16 May 2011. For this particular substorm there are limited auroral observations. Therefore, we use the Gillam (GILL) and FSMI MSP data from the NORSTAR array to diagnose the auroral onset. The look directions of both MSPs are illustrated in Figure 4.1. The geosynchronous magnetic field shows a clear dipolarisation of the field at 08:28 UT, depicted by the sharp increase in the inclination angle. Prior to the dipolarisation there is a compression of the geosynchronous magnetic field, illustrated by the increase in the magnetic field strength and decrease in the inclination angle between about 08:15-08:25 UT. During this time period substorm bays begin to form in the FSMI, FSMI and GILL magnetograms (b-d,

respectively) and the aurora begins to expand poleward in the FSMI and GILL MSPs (e-f respectively). The FSIM magnetometer shows the earliest evidence of substorm magnetic bay structure at ~08:17 UT as the H-component (blue) begins to form a negative bay just before the aurora brightens and begins to move poleward at 08:20:30 UT as observed by the FSMI MSP.

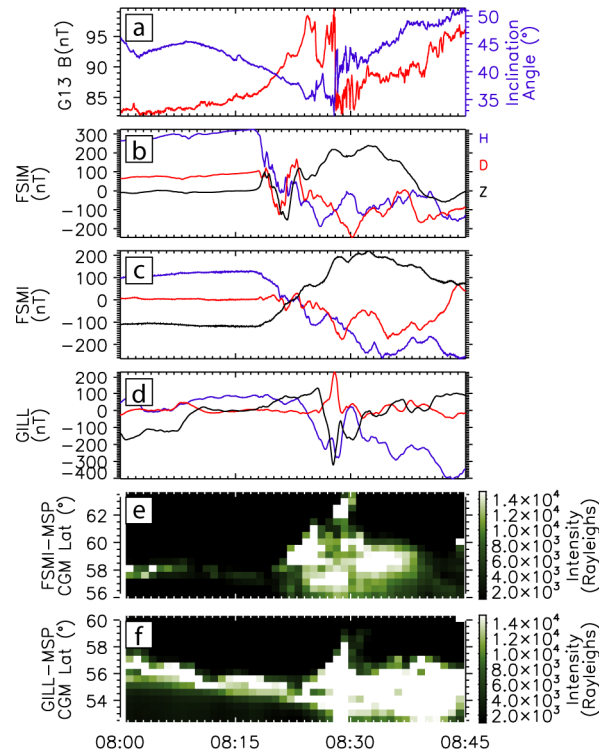


Figure 4.8: A summary of the 16 May 2011 substorm. (a) The G13 geosynchronous magnetic field (red) and inclination angle (blue). (b-d) FSIM, FSMI and GILL magnetograms are in the same format as Figure 2. (e-f) Green line emissions from the FSMI and GILL NORSTAR MSPs.

Figure 4.9, in the same format as Figure 4.3, show the AMPERE derived FACs through the growth and expansion phase of the substorm. Throughout the growth phase there is clear evidence of the region 1 and region 2 current systems on both the day- and night-side, between 07:40-07:50 UT in Figure 4.9a, and a similar though enhanced pattern of currents is seen just prior to auroral onset, 08:02-08:12 UT in Figure 4.9b on the day-side. Similar to the previous two events there is also evidence of a change in the FAC structure preceding aurora onset. Initially, in Figure 4.9a the 07:40-07:50 UT frame, the dusk-side low-latitude downward FAC (blue) extends to midnight and the high-latitude upward FAC (red) extends to 23 MLT. On the dawn-side the low-latitude upward FAC

extends past midnight to 23 MLT and the upward FAC extends to 1 MLT. Just prior to onset, in Figure 4.9b between 08:02-08:12 UT, these FAC structures undergo a clear and distinguished change. Both the upward and downward FAC structures on the dusk-side have withdrawn from the midnight meridian and on the dawn-side the upward and downward FACs have a notable change in the strength of the current densities through the midnight meridian. Following substorm onset, between 08:28-08:38 UT in Figure 4.9c, a complex system of upward and downward FAC forms on night-side, between 23-1 MLT and 60°-80° CGM latitude.

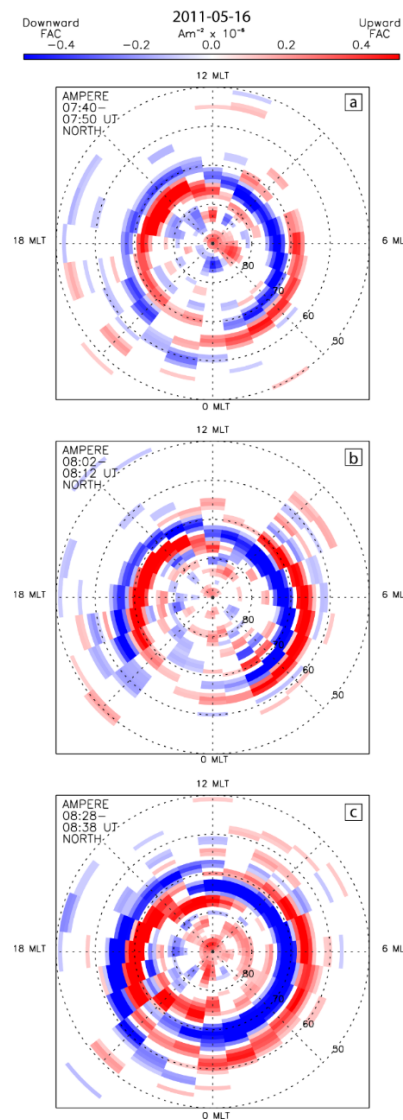


Figure 4.9: AMPERE derived FACs for the 16 May 2011 substorm during selected periods in the same format as Figure 3.

#### 4.3.4 The Substorm Current Wedge

The night-side expansion phase FACs shown in Figure 4.4, Figure 4.7, and Figure 4.9c are all characteristic of the SCW. These current systems show the existence of small scale FAC structures and are more complex than the simple equivalent current system of the SCW [McPherron et al., 1973] and FACs described by Iijima and Potemra [1978]. Figure 4.10, shows the night-side FACs forming during the substorm expansion phase for each of the three substorms studied here. The left column of Figure 4.10 shows the AMPERE derived FACs as well as the Pi2 ULF hodograms from selected low-, mid-, and auroral-latitude magnetometers. Lester et al. [1983] demonstrated that the direction of azimuth of Pi2 hodograms at low- and mid-latitudes can be used to infer the location of the upward and downward FAC elements and center of the SCW, whilst Milling et al. [2008] demonstrated the same polarisation pattern of Pi2s in the auroral zone. The Pi2 hodograms shown in Figure 4.10 were determined from 80-120 second period bandpassed magnetograms following substorm onset. The colour bar denotes the temporal evolution of each hodogram and the polarisation sense. In each hodogram H is parallel to the local latitude axis, north-south, and D points east-west parallel, or tangent, to the local MLT. The green line, or legend, represents 10 nT and the pink line represents 1 nT at auroral and lower latitude magnetometers, respectively. The center of each line marks the magnetometer location. Each hodogram and corresponding legend is independently scaled such that a smaller legend implies a larger Pi2 at that station and larger signal to noise ratio. Each legend is oriented in the north-south direction, pointing towards the geomagnetic pole.

The right panel of Figure 4.10 shows the net FAC as a function of MLT calculated by summing AMPERE FACs in latitude for each hour of MLT. The strength of the H- and D-component magnetic bays from auroral zone stations at the beginning (blue), middle (yellow) and end (red) of the ten minute AMPERE window are plotted as two-dimensional vectors along the x abscissa. The ground-based magnetic bays, formed as a result of the development of the SCW through the expansion phase, have distinct polarities based on the relative location of the magnetometer station to the longitudinal structure of the SCW, see for instance Clauer and McPherron [1974] Figure 7 [see also Smith et al., 2002 Figure 8]. In each panel of the right column of Figure 4.10 the

amplitude of the H and D magnetic bays are plotted to compare ground-based observations of the SCW with those from AMPERE, positive H and D pointing up and right, respectively.

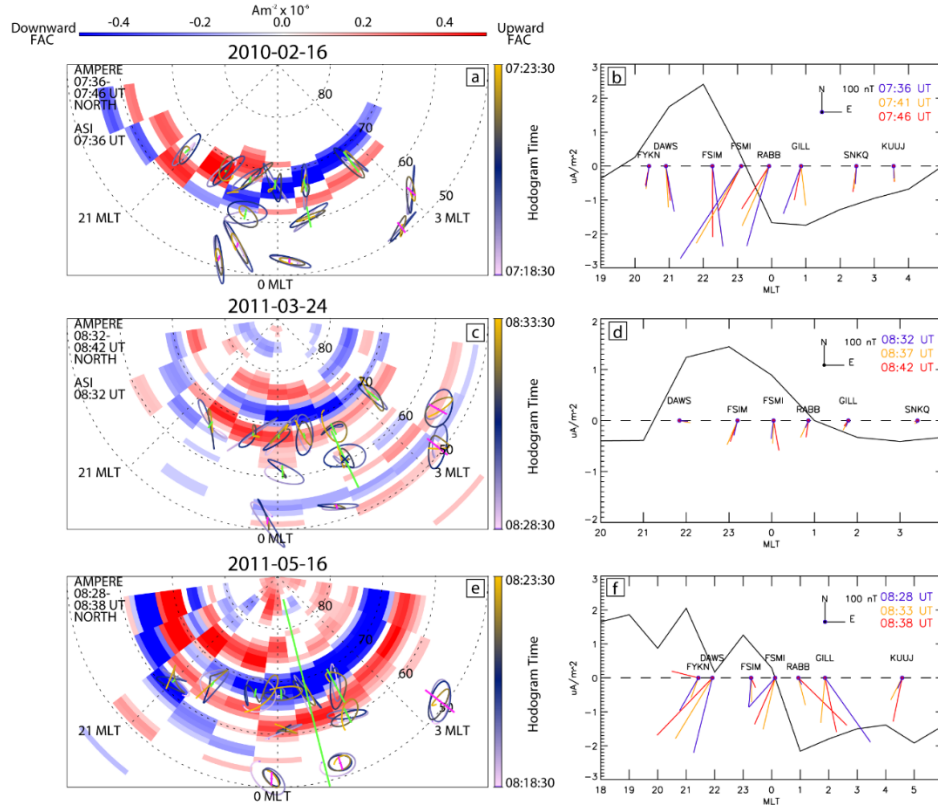


Figure 4.10: Left column: Night-side AMPERE derived FACs during the substorm expansion phase for the three substorms. The Pi2 hodograms from selected auroral and low-latitude magnetometer stations are overplotted. The vertical color bar denotes the time sequence of each hodogram, such that the color evolution in the hodograms allows the polarization sense (clockwise or counter clockwise) to be inferred. Right column: The latitudinal summation of the AMPERE FACs as a function of MLT for each of the two-dimensional AMPERE FAC topologies shown in the left column (black line). The strength of the H- and D-component auroral zone magnetic bays at the beginning (blue), middle (yellow) and end (red) of each ten minute window used to derive the AMPERE FACs are superimposed on each panel. In the bays positive H (north-south) points upward and positive D (east-west) points right as illustrated by the legend in the top right of each panel.

Both the right and left panels of Figure 4.10 support the classical view of the large scale structure of the SCW. For each of the three substorms the right column shows a net upward FAC pre-midnight and a net downward FAC post-midnight when the AMPERE FACs are integrated across latitude. Through the auroral zone the ground-based magnetometers show the largest negative H bays in the region where the net FAC is

nearly zero, i.e., through the expected center of the SCW. Through this region there is also a clear reversal in the D magnetic bays, negative to the east and positive to the west. This picture of the relation between net FAC and the ground-based magnetic bays is consistent with those presented by McPherron et al. [1973] and Smith et al. [2002] using the equivalent line current model.

The Pi2 hodograms also support the classical picture of the SCW. As demonstrated by Lester et al. [1983], inside the SCW the semi-major axis (or angle of azimuth) of the Pi2 hodograms point toward the center of the wedge and outside the SCW the semi-major axes' point away from the center of the wedge such that there is a rotation of the semi-major axis across the center of the SCW and across the upward and downward FAC elements [c.f. Figure 1 in Lester et al., 1984]. For each of the substorm events presented the auroral zone and low-latitude hodograms show a rotation in the Pi2 hodogram azimuths consistent with that described by Lester et al. [1983].

During the substorm on 16 February 2010 the auroral zone magnetometers show evidence of a reversal in the Pi2 azimuths between 21 and 22 MLT, the semi-major axis pointing west of north at ~21 MLT and east of north at ~22 MLT. No other clear reversal was observed in the auroral zone magnetometer data. At lower latitudes the hodograms show another reversal in azimuth between magnetic midnight and ~1 MLT where the semi-major axis of the low-latitude magnetometer at ~53° points west of north and between 1-2 MLT the semi-major axis of the hodogram at ~61° points east of north. Together, the inferred location of the upward and downward FAC elements of the SCW from the ground-based Pi2 observations is between 21 and 22 MLT and magnetic midnight and 1 MLT, respectively. The location of the upward and downward FACs determined from the Pi2 hodograms is consistent with the net FAC illustrated in Figure 4.10b.

On 24 March 2011, the Pi2 hodograms show a reversal of the semi-major axis in the auroral zone between 22 and 23 MLT and another reversal at both the auroral and low-latitude magnetometers between 3 and 4 MLT. At 22 MLT the semi-major axis at ~66° points west of north and at 23 MLT the semi-major axis at ~66° points east of north. In the morning sector the semi-major axis auroral zone hodogram at ~66 and ~3 MLT points just slightly west of north. Conversely, the low-latitude hodograms between 3-4

MLT both have semi-major axes which point east of north. Together, these hodograms suggest that the upward FAC of the SCW lies between 22-23 MLT and downward FAC element lies between 3-4 MLT. These observations are consistent with the net FAC shown in Figure 4.10d.

Finally, the hodograms on 5 May 2011 are more complicated than those of the two other substorms, especially in the auroral zone. The auroral zone does show evidence of a reversal in the azimuths of the hodograms between 1 and 2 MLT. At 1 MLT the semi-major axis points west of north and at 2 MLT the semi-major axis points east of north. However, to the west there is no clear evidence of any organised structure in the hodograms. Despite this, auroral zone hodograms between 1 and 2 MLT is characteristic of a region of downward FAC and consistent with a net downward FAC as show in Figure 4.10f. It is important to note that Lester et al. [1984] showed that not all substorms follow the predicted polarisation pattern, and that during events with pre-existing magnetic activity the polarisation patterns can become significantly more complicated making it difficult to infer the location of the upward and downward FAC elements of the SCW.

#### **4.4 Discussion**

In this paper we have presented multi-satellite observations of the FACs associated with the substorm growth and expansion phases and examine the two-dimensional structure and evolution of FACs in the SCW. FACs are inherently difficult to determine from in-situ measurements, especially from single satellites, as the derivation of these currents assumes that a temporal observation of the magnetic field can be used to approximate spatial gradients in the field. For this reason, single satellite inferences of FACs can be flawed as they are unable to separate spatial changes from temporal changes with single point measurements. This space-time ambiguity can be removed using multi-spacecraft studies to identify quasi-stationary time periods during which temporal changes can be neglected. In this paper we use derived FAC distributions from AMPERE and the Iridium constellation of 70+ satellites, during quasi-stationary time periods for three substorms, to develop a comprehensive two-dimensional view of the FAC systems coupling the ionosphere and magnetosphere. As a result, we present the most detailed

two-dimensional view of the structure of the FACs comprising the SCW to date. In particular we show:

1. During the late growth phase and immediately prior to substorm onset, there is evidence of a change or reduction in the night-side FACs in the region of subsequent auroral substorm onset.
2. During the substorm expansion phase, regions of upward FACs are associated with discrete auroral forms. This demonstrates, for the first time, a two-dimensional correspondence between discrete aurora and upward FAC.
3. Following substorm expansion phase onset an enhanced and highly structured system of upward and downward FACs forms on the night-side. When averaged over all latitudes, this complex current system reduces to what is typically described in terms of a simpler equivalent current system, the SCW.

During the late growth phase, immediately preceding onset, discrete changes in the FAC density are observed on the night-side in each of the three substorms studied here. Murphy et al. [2012] discussed in detail the change in FAC observed during the 16 February 2010 substorm. We briefly restate those results here and demonstrate that similar changes are observed during both of the two other substorms. For the 16 February 2010 case, Figure 4.3 shows a clear decrease in the FAC strength between the 06:42-0652 UT frame and the 07:06-07:26 UT frame between 21-3 MLT and 63°-73° CGM latitude. During the 24 March 2011 substorm, a reduction in the FAC density in the region between 21-3 MLT and 60°-80° CGM latitude is observed between the 08:00-08:10 UT frame and the 08:14-08:24 UT frame as illustrated in Figure 4.6 . Although the 16 May 2011 substorm shows less drastic changes there is still evidence of a change in the FAC densities and topology between the 07:40-07:50 UT and the 08:02-08:12 UT frames just prior to substorm onset in the pre-midnight sector between 60°-70° CGM latitude.

Previous observations have clearly shown the presence of wave activity in ground-based auroral images [Elphinstone et al., 1995; Donovan et al., 2008; Liang et al., 2008; Rae et al., 2010] with clear correlation between auroral waves and ground magnetic waves [e.g., Rae et al., 2009a, b; 2011; 2012] immediately prior to auroral substorm expansion phase onset and the formation of the SCW and westward traveling surge in the aurora. Moreover, Newell et al. [2010] showed a clear increase in wave-driven auroral particle precipitation in the minutes prior to substorm expansion phase onset. Recent observations of localised changes in the strength of night-side FACs prior to substorm onset suggest a key role for magnetosphere-ionosphere coupling in the late growth of a substorm [Murphy et al., 2012]. The changes in FACs prior to substorm onset are likely mediated via the exchange of Alfvén waves between the magnetosphere and ionosphere prior to the traditional definition of substorm onset [Murphy et al., 2012]. Such changes and related reduction in upward FACs may be manifested as auroral dimming preceding onset as illustrated in Figure 4.2e and Figure 4.5e [see also Pellinen and Heikkila, 1978; Baumjohann et al., 1981; Murphy et al., 2012]. The formation of auroral beads [Donovan et al., 2008; Rae et al., 2009a,b; Rae et al., 2010], potentially characteristic of a near-Earth plasmashet disturbance proceeding the substorm expansion phase [e.g., Roux 1985; Lui, 1996; Samson et al., 1996; Maynard et al., 1996] may also be related to localised changes in the night-side FAC topology. With additional in-situ instrumentation and ground-based observations, the detailed relationship between these features will be addressed further in future work. In any case, the observations of Murphy et al. [2012] considered together with those presented here provide important constraints to any substorm onset paradigm [c.f. Murphy et al., 2012].

Following auroral substorm onset, during the substorm expansion phase, the FACs coupling the ionosphere to the magnetosphere undergo a radical topological change which is most notable on the night-side. However, there is evidence of enhanced FACs on the day-side as well. On the day-side the region 1 and region 2 currents become enhanced and small-scale upward and downward FAC structures are observed in addition to the standard region 1 and region 2 current features (see Figure 4.3, Figure 4.6, and Figure 4.9). Whether this enhancement is the result of the substorm expansion phase or the effects of changes in solar wind driving is unclear. However, the

enhancement of day-side FACs during the substorm expansion phase is consistent with the observations of Rostoker et al. [1982] who suggested that the night-side magnetotail currents can couple to the entire magnetosphere-ionosphere current system, including the day-side, through an enhanced auroral electrojet which forms during the substorm expansion phase.

On the night-side, following auroral substorm onset, the FAC topology becomes highly structured and enhanced in each of the three substorms presented here. In each MLT sector, distinct azimuthal bands of upward and downward FAC form with periodic structuring in latitude (Figure 4.3, Figure 4.4, Figure 4.6, Figure 4.7, and Figure 4.9) [c.f. Inhester et al., 1984 and Gjerloev and Hoffman 2002]. These FAC structures are significantly more complicated than the equivalent line current system associated with the SCW [McPherron et al., 1973] and the enhanced region 1 and 2 current system developed during active magnetospheric conditions [Iijima and Potemra, 1978]. However, when spatially averaged, these structured net upward and downward FACs depict the same line current SCW proposed by McPherron et al., [1973].

FACs are inherently difficult to infer from in-situ observations. Temporal variations in the magnetic field can lead to inaccurately derived FACs [Peria et al., 2000; Zheng et al., 2003; Gjerloev et al., 2011]. Zheng et al. [2003] demonstrated using the Four Free-Flying Magnetometer payload of the Estrophy sounding rocket mission that the FAC density derived from multi-point measurements are typically smaller than those derived from single-point measurements. Similarly, using magnetometer data from the three ST 5 satellites Gjerloev et al. [2011] showed that the correlation between multi-point magnetic field measurements decreases as a function of spacecraft separation. The magnetic fields are often not stationary in time over the duration of successive satellite passes. These studies clearly demonstrate that the further apart the observations, the more susceptible they are to spatio-temporal ambiguities which introduce errors into any derived FAC. In order to derive accurate FACs from in-situ measurements a constellation of closely spaced satellites is required to reduce the uncertainty introduced by a space-time ambiguity.

In this study we have used quasi-stationary ten minute time periods defined by multiple night-side passes of satellites from the Iridium constellation to derive FAC estimates and

determine the two-dimensional FAC topology during the substorm expansion phase. However, the substorm expansion phase is very dynamic. The aurora explosively expands forming the westward traveling surge, the magnetotail dipolarises, and the auroral electrojets become enhanced. To verify that the AMPERE derived FACs are an adequate representation of the FACs in the expansion phase the derived FACs have been overplotted with auroral observations from THEMIS ASIs. Variability in auroral intensity in the THEMIS white light imagers is largely the result of the energy of precipitating electrons [Mende et al., 2011; see also Mende et al., 2008]. Thus by assuming that discrete aurora seen in the THEMIS ASI data are the result of precipitating electrons associated with upward FAC structures we are able to validate the AMPERE derived FACs and for the first time, verify that two-dimensional discrete arcs are identified by upward FAC structures.

Figure 4.4 and Figure 4.7 show the AMPERE FACs superimposed onto the THEMIS ASI data following substorms on 16 February 2010 and 24 March 2011, respectively. Both Figure 4.4 and Figure 4.7, show a remarkable correlation between the THEMIS ASI auroral observations and derived AMPERE FACs. In each case discrete auroral forms are principally associated with regions of upward FAC in the pre-midnight sector. The largest discrepancy is in the final two auroral frames in Figure 4.4a. A discrete auroral arc expands westward along the boundary between the upward and downward FACs at 21 MLT and 66° CGM latitude and back into a region of upward FAC at 22 MLT. This may be the result of local changes in the magnetic field and auroral precipitation, and specifically the poleward motion of the aurora during the expansion phase, leading to a localised breakdown in the quasi-stationary assumption used to derive FACs and an incorrectly derived location of the region of upward FAC over the ten minute time period. Despite this small discrepancy, overall Figure 4.4 and Figure 4.7 demonstrate a remarkable relation between the AMPERE derived upward FACs and discrete aurora seen in the THEMIS ASI data during the substorm expansion phase. Not only do these observations verify the accuracy of the derived location and structure of the FACs from AMPERE and Iridium, they also provide the first observations of a two-dimensional correspondence between discrete aurora and upward FAC.

Gelpi et al. [1987] demonstrated, using both in-situ magnetic field and auroral observations and ground-based magnetometer observations, that the head of the westward travelling surge was associated with upward FAC. Similarly, using FAST satellite passes through a single meridian of the westward traveling surge (WTS) identified by auroral observations from the Imager for Magnetopause-to-Aurora Global Exploration (IMAGE) spacecraft, Mende et al. [2003a; 2003b] demonstrated that the WTS is characteristic of intense upward FACs and precipitating electrons. Using ground-based auroral cameras and the FAST spacecraft, Dubyagin et al. [2003] have further shown that the substorm onset arc is embedded in a region of upward FAC. Our results are consistent with Mende et al. [2003a; 2003b] and Dubyagin [2003]. However, we extend these results for the first time to two-dimensions demonstrating a clear correspondence between discrete aurora and upward FAC over an extended range of latitude and MLT during the substorm expansion phase.

While the night-side current systems that form during the substorm expansion phase are more complex than the equivalent line current system [McPherron et al., 1973], Figure 4.10 clearly demonstrates that these current systems are characteristic of the SCW for each case study shown. The structured FACs illustrated in Figure 4.10 are consistent with auroral observations from the THEMIS ASI data, the ground-based Pi2 hodograms, and the ground-based magnetic bays forming as a result of the overhead SCW. Based on the three case study observations presented here, in Figure 4.11 we present an idealised schematic of the FAC topology seen by AMPERE the during substorm sequence. From top to bottom the panels in Figure 4.11 show the growth phase, just prior to substorm onset and during the substorm expansion phase. During the substorm growth phase the FAC system is characteristic of an enhanced region 1/region2 current system (c.f., Figure 4.11a). This enhanced current system is characteristic of the enhanced magnetospheric and ionospheric currents developing during substorm growth phase [McPherron, 1970] and under active magnetospheric conditions [Iijima and Potemra, 1978]. Following the substorm growth phase and just prior to auroral onset the night-side FACs undergo a distinct topological change, Figure 4.11b. The shaded grey region in Figure 4.11b highlights the region surrounding magnetic midnight where substorm onset typically occurs and the small circle characterises the localised change in FACs prior to auroral substorm onset. Murphy et al.

[2012] discussed this change in detail highlighting an important change in FAC local to and preceding auroral substorm onset. However, more work is required in order to fully understand the change in FACs and examine in detail the pre-onset changes in magnetosphere-ionosphere coupling prior to auroral onset. Hence in Figure 4.11b we only note that there is a change in night-side FACs preceding auroral onset. Following substorm expansion phase onset, a series of azimuthally banded and latitudinally periodic upward and downward FACs form across the night-side, Figure 4.11c. This night-side FAC topology is in fact the detailed two-dimensional structure of the SCW.

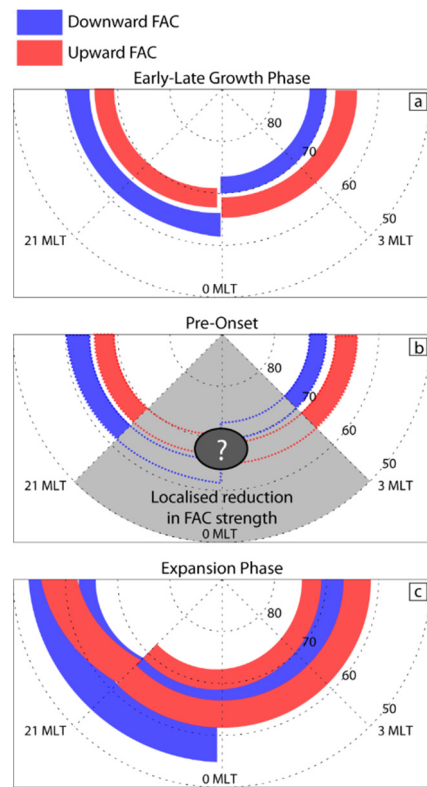


Figure 4.11: A schematic of the night-side FAC system during (a) the substorm growth phase, (b) prior to substorm onset, and (c) during the substorm expansion phase. In each panel red denotes upward FAC and blue downward FAC. Panel (c) is a schematic of the fine structure of the upward and downward FAC seen by AMPERE and which on a large scale composes the SCW FAC current system. Higher longitudinal resolution studies are needed to resolve the onset region in panel (b).

The original descriptions of the SCW equivalent current system as a downward FAC element in the east, an enhanced westward electrojet, and an upward FAC element in the west was derived from ground-based magnetometer observations [McPherron et al. 1973]. The FAC topology illustrated in Figure 4.11c has the same equivalent current

distribution as that described by McPherron et al. [1973], a net downward FAC in the east and net upward FAC in the west (c.f. Figure 4.10). However, with the increased spatial resolution of the AMPERE in-situ observations we are able to derive a more detailed view of the SCW, and detail potentially critical aspects of M-I coupling during substorms. Figure 4.12 is a schematic of the two dimensional FACs forming during the substorm expansion phase. Superimposed onto these FACs is illustrating the SCW equivalent current system. The blue, green and red arrows represent the equivalent current structure of the SCW; blue, the net downward FAC, red, the net upward FAC, and green, the enhanced westward electrojet. The azimuthal bands of upward and downward FAC, red and blue respectively, illustrate the complex structure of FACs forming during the expansion phase and comprising the SCW.

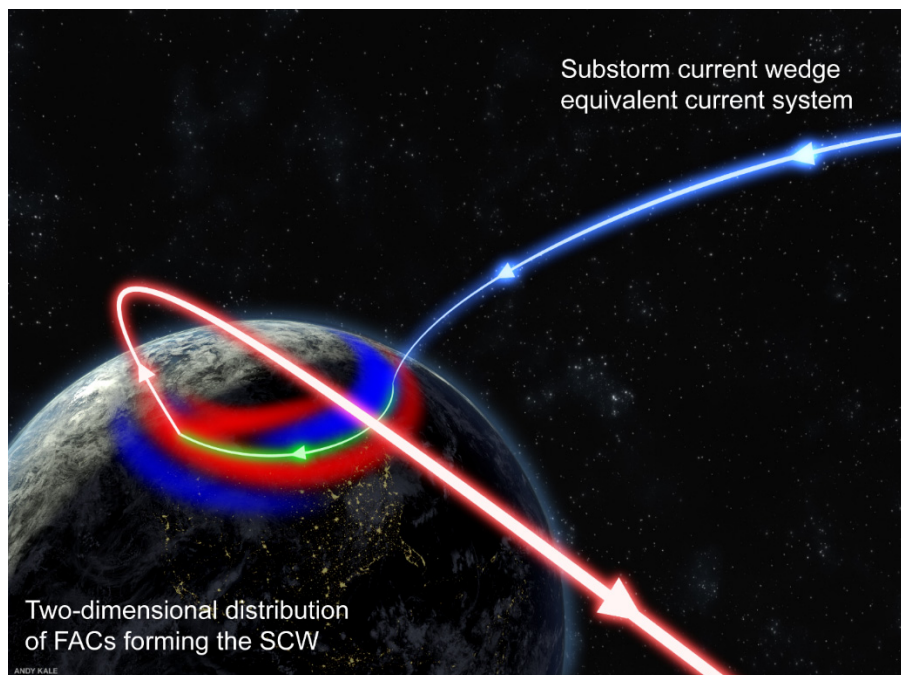


Figure 4.12: A schematic of the two dimensional FACs forming during the substorm expansion phase and the equivalent current system forming the SCW. The blue, green and red arrows represent the net upward FAC, the enhanced westward electrojet and the net upward FAC of the SCW. The azimuthal bands of upward and downward FAC, red and blue respectively, illustrate the complex structure of FACs forming during the expansion phase and comprising the SCW.

Using single satellite passes through the auroral zone, Rostoker et al. [1975] demonstrated that an intense region of upward FAC formed along the enhanced ionospheric electrojets surrounded to the north and south by regions of downward FAC following substorm onset which is similar to our AMPERE results. Using single satellite

passes through the auroral zone, Iijima and Potemra [1978] compiled a statistical study of Triad passes to develop a statistical view of the FAC topology during active magnetospheric conditions. These authors concluded that the region 1 and region 2 current systems persisted during active magnetospheric conditions, although in the region of the Harang discontinuity the currents were significantly more complex. During moderately active conditions Iijima and Potemra [1978] found evidence of a current system similar to that described by Rostoker et al. [1973], whereas during very active conditions the currents were very complicated, exhibiting fine-scale variations. The current systems described by Rostoker et al. [1973] and Iijima and Potemra et al. [1978] are consistent with the equivalent current system described by McPherron et al. [1973] and with the SCW schematic shown in Figure 4.11c. The upward FAC surrounded by downward FACs at higher and lower latitudes [c.f. Rostoker et al., 1973; Iijima and Potemra, 1978] is similar to the FAC topology forming in the post-midnight sector. In the pre-midnight sector however, a more complicated current system forms following substorm onset and there is no evidence of the distinct region 1 and region 2 current systems as described by Iijima and Potemra [1978].

The differences between the pre-midnight current system described here and the current systems described by Rostoker et al. [1973] and Iijima and Potemra [1978] likely result from comparing single-satellite case and statistical studies to the more accurate description of FAC structure obtained from multi-satellite studies presented here. Iijima and Potemra [1978] developed a two dimensional distribution of FACs by spatially averaging large scale FACs from multiple passes of the Triad satellite through the auroral zone. This averaging will obscure small scale spatial structures, producing a smoothed distribution of FACs in both MLT and latitude. In this study we have derived the schematic illustrated in Figure 4.11c using two-dimensional multi-satellite coverage from three case studies. In each case-study we were able to determine the full two-dimensional distribution of FACs, rather than relying on a statistical average. Therefore, the schematic illustrated in Figure 4.11 is not subject to any spatial smoothing and is expected to be a more accurate representation of the FAC current topology during the substorm cycle.

In each of the substorms studied, the complex night-side FAC system formed in the expansion phase developed during auroral break-up and in two cases during the dipolarisation of the geosynchronous magnetic field. Thus, the inward convection of electrons [Vasyliunas, 1968], onset of fast flows [Angelopoulos et al., 1992], and development of dipolarisation fronts [Runov et al., 2008] following tail reconnection are likely to be intimately linked to the development of the current system depicted in Figure 4.11c.

Yao et al. [2012] recently demonstrated that the azimuthal divergence or deceleration of fast flows in the tail observed during the substorm expansion phase produced a FAC current signature consistent with the equivalent current system described by McPherron et al. [1973]. Our AMPERE-derived observations of the net FAC as a function of MLT are consistent with the observations of Yao et al. [2012]. The two-dimensional AMPERE FAC distributions show latitudinal and azimuthal structuring in the form of discrete upward and downward FAC current sheets. Birn et al. [1999] demonstrated that the braking of earthward flows contributed to the initial formation of the SCW but that the more dominant and permanent current contributions were the result of pressure gradients. Further, Mende et al. [2003b] concluded that high-energy precipitating electrons, energised by Alfvén waves driven by the dipolarisation of the field or reconnection at the near-Earth neutral line are responsible for part of the current forming in the westward travelling surge. The FAC current system developing during the substorm expansion phase illustrated in Figure 4.11c is a superposition of all the current forming during the substorm expansion phase. Therefore it is not surprising that the current system is more complicated than that described by McPherron et al [1973] or that illustrated in Yao et al. [2012]. Indeed we have demonstrated that expansion phase FAC current system is very well correlated with the expansion phase aurora and forms following auroral breakup and dipolarisation of the tail. Though this current system is more complex than the classical view of the SCW it is fully consistent with the equivalent current system described by McPherron et al. [1973] (see schematic in Figure 4.12).

## **4.5 Summary and Conclusions**

The substorm current wedge has historically been viewed using an equivalent current system comprised of a downward FAC element in the dawn sector, an enhanced

westward electrojet, and an upward FAC element in the dusk sector [McPherron et al., 1973]. In this manuscript we have used in-situ measurements from the low-Earth orbiting Iridium constellation and the AMPERE mission [Anderson et al., 2000 and Waters et al., 2001] to characterise in more detail the two-dimensional FAC system coupling the ionosphere to the magnetosphere during the substorm growth and expansion phases. These results are only possible using multi-point measurements available via AMPERE.

In particular, we have demonstrated that several minutes prior to substorm onset there is a localised change or reduction in the night-side FAC system which was described by Murphy et al. [2012] and which represents a change in the magnetosphere-ionosphere coupling before onset. Following substorm onset a complex and highly structured system of FACs forms on the night-side (Figure 4.12). The upward FAC elements of this intricate FAC system are correlated with discrete aurora during the expansion phase. This demonstrates for the first time a two-dimensional correspondence between upward FAC structures and discrete aurora. Although more complex than the equivalent line current system comprising the SCW, the structured FAC system we report here and which form during the substorm expansion phase is fully consistent with that described by McPherron et al. [1973] and with ground-based observations of the SCW during the expansion phase [Lester et al., 1983 and Smith et al., 2002] if it is integrated over all latitudes to show the net upward and downward FAC as a function of MLT. Finally we present a detailed schematic of the FACs through the substorm growth and expansion phases, Figure 4.11 and Figure 4.12, and note that the complexity of the currents suggests future work should address the effects of multiple night-side FAC sources to explain the observed morphology of the SCW.

## **4.6 References**

- Akasofu, S. I. (1964), The development of the auroral substorm, *Planet. Space Sci.*, 12, 273-282.
- Anderson, B. J., K. Takahashi, and B. A. Toth (2000), Sensing global Birkeland currents with Iridium® engineering magnetometer data, *Geophys. Res. Lett.*, 27(24), 4045–4048, doi:10.1029/2000GL000094.

- Angelopoulos, V., W. Baumjohann, C. F. Kennel, F. V. Coroniti, M. G. Kivelson, R. Pellat, R. J. Walker, H. Lühr, and G. Paschmann (1992), Bursty bulk flows in the inner central plasma sheet, *J. Geophys. Res.*, 97(A4), 4027–4039, doi:10.1029/91JA02701.
- Baumjohann, W., R.J. Pelunen, H.J. Opgenoorth, E. Nielsen (1981), Joint two-dimensional observations of ground magnetic and ionospheric electric fields associated with auroral zone currents: Current systems associated with local auroral break-ups, *Planetary and Space Science*, 29, 4, Pages 431-447, doi:10.1016/0032-0633(81)90087-8.
- Birn, J., M. Hesse, G. Haerendel, W. Baumjohann, and K. Shiokawa (1999), Flow braking and the substorm current wedge, *J. Geophys. Res.*, 104(A9), 19895-19903.
- Clauer, C., and R. McPherron (1974), Mapping the Local Time-Universal Time Development of Magnetospheric Substorms Using Mid-Latitude Magnetic Observations, *J. Geophys. Res.*, 79(19), 2811-2820.
- Cummings, W., J. Barfield, and P. Coleman Jr. (1968), Magnetospheric substorms observed at the synchronous orbit, *J. Geophys. Res.*, 73(21), 6687-6698.
- Donovan, E. F., et al. (2003), All-sky imaging within the Canadian CANOPUS and NORSTAR projects, *Sodankyla Geophys. Obs. Publ.*, 92, 109–112.
- Donovan, E., et al. (2008), Simultaneous THEMIS in situ and auroral observations of a small substorm, *Geophys. Res. Lett.*, 35, L17S18, doi:10.1029/2008GL033794.
- Dubyagin, S. V., V. A. Sergeev, C. W. Carlson, S. R. Marple, T. I. Pulkkinen, and A. G. Yahnin (2003), Evidence of near-Earth breakup location, *Geophys. Res. Lett.*, 30(6), 1282, doi:10.1029/2002GL016569.
- Elphinstone, R. D., et al. (1995), The double oval UV auroral distribution: 1. Implications for the mapping of auroral arcs, *J. Geophys. Res.*, 100(A7), 12,075–12,092, doi:10.1029/95JA00326.

- Gelpi, C., H. J. Singer, and W. J. Hughes (1987), A comparison of magnetic signatures and DMSP auroral images at substorm onset: Three case studies, *J. Geophys. Res.*, 92(A3), 2447–2460, doi:10.1029/JA092iA03p02447.
- Gjerloev, J. W., and R. A. Hoffman, Currents in auroral substorms, *J. Geophys. Res.*, 107(A8), doi:10.1029/2001JA000194, 2002.
- Gjerloev, J. W., Ohtani, S., Iijima, T., Anderson, B., Slavin, J., and Le, G. (2011), Characteristics of the terrestrial field-aligned current system, *Ann. Geophys.*, 29, 1713-1729, doi:10.5194/angeo-29-1713-2011.
- Iijima, T. and T. A. Potemra (1976), The amplitude distribution of field-aligned currents at northern high latitudes observed by Triad, *J. Geophys. Res.*, 81(13), 2165–2174, doi:10.1029/JA081i013p02165.
- Iijima, T. and T. A. Potemra (1978), Large-scale characteristics of field-aligned currents associated with substorms, *J. Geophys. Res.*, 83(A2), 599–615, doi:10.1029/JA083iA02p00599.
- Inhester, B., W. Baumjohann, R. A. Greenwald, E. Nielsen, Joint two-dimensional observations of ground magnetic and ionospheric electric fields associated with auroral zone currents, 3, *Auroral zone currents during the passage of a westward traveling surge*, *J. Geophys.*, 49, 155, 1981.
- Kisabeth, J. L. and G. Rostoker (1971), Development of the polar electrojet during polar magnetic substorms, *J. Geophys. Res.*, 76(28), 6815–6828, doi:10.1029/JA076i028p06815.
- Lester, M., W. J. Hughes, H. J. Singer, Polarization patterns of Pi 2 magnetic pulsations and the substorm current wedge, *J. Geophys. Res.*, 88, 7958, 1983.
- Lester, M., W. J. Hughes, and H. J. Singer (1984), Longitudinal structure in Pi 2 pulsations and the substorm current wedge, *J. Geophys. Res.*, 89(A7), 5489–5494, doi:10.1029/JA089iA07p05489.
- Liang, J., E. F. Donovan, W. W. Liu, B. Jackel, M. Syrjäsuo, S. B. Mende, H. U. Frey, V. Angelopoulos, and M. Connors (2008), Intensification of preexisting auroral arc

- at substorm expansion phase onset: Wave-like disruption during the first tens of seconds, *Geophys. Res. Lett.*, 35, L17S19, doi:10.1029/2008GL033666.
- Lui, A. T. Y. (1996), Current disruption in the Earth's magnetosphere: Observations and models, *J. Geophys. Res.*, 101, 13,067–13,088, doi:10.1029/96JA00079.
- Mann, I. R., et al. (2008), The Upgraded CARISMA magnetometer array in the THEMIS era, *Space Sci. Rev.*, 141, 413–451, doi:10.1007/s11214-008-9457-6.
- Maynard, N. C., W. J. Burke, E. M. Basinska, G. M. Erickson, W. J. Hughes, H. J. Singer, A. G. Yahnin, D. A. Hardy, and F. S. Mozer (1996), Dynamics of the inner magnetosphere near times of substorm onsets, *J. Geophys. Res.*, 101(A4), 7705–7736, doi:10.1029/95JA03856.
- McPherron, R. L. (1970), Growth phase of magnetospheric substorms, *J. Geophys. Res.*, 75(28), 5592–5599, doi:10.1029/JA075i028p05592.
- McPherron, R. L., C. T. Russell, and M. P. Aubry (1973), Satellite studies of magnetospheric substorms on August 15, 1968: 9. Phenomenological model for substorms, *J. Geophys. Res.*, 78(16), 3131–3149, doi:10.1029/JA078i016p03131.
- Mende, S. B., C. W. Carlson, H. U. Frey, L. M. Peticolas, and N. Østgaard (2003a), FAST and IMAGE-FUV observations of a substorm onset, *J. Geophys. Res.*, 108(A9), 1344, doi:10.1029/2002JA009787
- Mende, S. B., C. W. Carlson, H. U. Frey, T. J. Immel, and J.-C. Gérard (2003b), IMAGE FUV and in situ FAST particle observations of substorm aurorae, *J. Geophys. Res.*, 108(A4), 8010, doi:10.1029/2002JA009413.
- Mende, S. B., et al. (2008), The THEMIS array of ground-based observatories for the study of auroral substorms, *Space Sci. Rev.*, 141, 357–387.
- Mende, S. B., H. U. Frey, V. Angelopoulos, and Y. Nishimura (2011), Substorm triggering by poleward boundary intensification and related equatorward propagation, *J. Geophys. Res.*, 116, A00I31, doi:10.1029/2010JA015733.

- Milling, D. K, et al. (2008), Ionospheric localisation and expansion of long-period Pi1 pulsations at substorm onset, *Geophys. Res. Lett.*, 35, L17S20, doi:10.1029/2008GL033672.
- Murphy, K. R., et al. (2012), Reduction in field-aligned currents preceding and local to auroral substorm onset, *Geophys. Res. Lett.*, 39, L15106, doi:10.1029/2012GL052798.
- Newell, P. T., A. R. Lee, K. Liou, S.-I. Ohtani, T. Sotirelis, and S. Wing (2010), Substorm cycle dependence of various types of aurora, *J. Geophys. Res.*, 115, A09226, doi:10.1029/2010JA015331.
- Olson, J. V. (1999), Pi2 pulsations and substorm onsets: A review, *J. Geophys. Res.*, 104(A8), 17,499–17,520, doi:10.1029/1999JA900086.
- Pellinen, R. J., and W. J. Heikkila (1978), Observations of auroral fading before breakup, *J. Geophys. Res.*, 83(A9), 4207–4217, doi:10.1029/JA083iA09p04207.
- Peria, W. J., C. W. Carlson, R. E. Ergun, J. P. McFadden, J. Bonnell, R. C. Elphic, and R. J. Strangeway (2000), Characteristics of field-aligned currents near the auroral acceleration region: FAST observations, in *Magnetospheric Current Systems*, *Geophys. Monogr. Ser.*, vol. 118, edited by S. Ohtani et al., pp. 181–189, AGU, Washington, D. C., doi:10.1029/GM118p0181.
- Rae, I. J., et al. (2009a), Near-Earth initiation of a terrestrial substorm, *J. Geophys. Res.*, 114, A07220, doi:10.1029/2008JA013771.
- Rae, I. J., et al. (2009b), Timing and localization of ionospheric signatures associated with substorm expansion phase onset *J. Geophys. Res.*, 114, A00C09, doi:10.1029/2008JA013559.
- Rae, I. J., C. E. J. Watt, I. R. Mann, K. R. Murphy, J. C. Samson, K. Kabin, and V. Angelopoulos (2010), Optical characterization of the growth and spatial structure of a substorm onset arc, *J. Geophys. Res.*, 115, A10222, doi:10.1029/2010JA015376.

- Rae, I. J., K. R. Murphy, C. E. J. Watt, I. R. Mann (2011), On the nature of ULF wave power during nightside auroral activations and substorms: 2. Temporal Evolution, *J. Geophys. Res.*, doi:10.1029/2010JA015762.
- Rae, I. J., C. E. J. Watt, K. R. Murphy, H. U. Frey, L. G. Ozeke, D. K. Milling, and I. R. Mann (2012), The correlation of ULF waves and auroral intensity before, during and after substorm expansion phase onset, *J. Geophys. Res.*, 117, A08213, doi:10.1029/2012JA017534.
- Rostoker, G., J. C. Armstrong, and A. J. Zmuda (1975), Field-aligned current flow associated with intrusion of the substorm-intensified westward electrojet into the evening sector, *J. Geophys. Res.*, 80(25), 3571–3579, doi:10.1029/JA080i025p03571.
- Rostoker, G., M. Mareschal, and J. C. Samson (1982), Response of dayside net downward field-aligned current to changes in the interplanetary magnetic field and to substorm perturbations, *J. Geophys. Res.*, 87(A5), 3489–3510, doi:10.1029/JA087iA05p03489.
- Roux, A. (1985), Generation of field-aligned current structures at substorm onsets, in *Proceedings of ESA Workshop on Future Missions in Solar, Heliospheric and Space Plasma Physics*, Eur. Space Agency Spec. Publ., ESA SP-235, 151.
- Runov, A., et al. (2008), Multipoint in situ and ground-based observations during auroral intensifications, *J. Geophys. Res.*, 113, A00C07, doi:10.1029/2008JA013493
- Russell, C. T., et al. (2008), THEMIS ground-based magnetometers, *Space Sci. Rev.*, 141, 389–412, doi:10.1007/s11214-008-9337-0.
- Samson, J. C., et al. (1996), Substorm intensifications and resistive shear flow-ballooning instabilities in the near-Earth magnetotail, in *Proceedings of the Third International Conference on Substorms (ICS-3)*, Eur. Space Agency Spec. Publ., ESA SP-389, 399.
- Singer, H. J., et al. (1996), Monitoring space weather with the GOES magnetometers, *Proc. SPIE Int. Soc. Opt. Eng.*, 2812, 299–308.

- Smith, A. J., M. P. Freeman, S. Hunter, and D. K. Milling (2002), VLF, magnetic bay, and Pi2 substorm signatures at auroral and midlatitude ground stations, *J. Geophys. Res.*, 107(A12), 1439, doi:10.1029/2002JA009389.
- Tsyganenko, N. A. (1995), Modelling the Earth's magnetospheric magnetic field confined within a realistic magnetopause, *J. Geophys. Res.*, 100(A4), 5599–5612, doi:10.1029/94JA03193.
- Vasyliunas, V. (1968), A Survey of Low-Energy Electrons in the Evening Sector of the Magnetosphere with OGO 1 and OGO 3, *J. Geophys. Res.*, 73(9), 2839-2884.
- Waters, C. L., B. J. Anderson, and K. Liou (2001), Estimation of global field aligned currents using the Iridium<sup>®</sup> system magnetometer data, *Geophys. Res. Lett.*, 28(11), 2165–2168, doi:10.1029/2000GL012725.
- Yao, Z. H., et al. (2012), Mechanism of substorm current wedge formation: THEMIS observations, *Geophys. Res. Lett.*, 39, L13102, doi:10.1029/2012GL052055.
- Zheng, Y., K. A. Lynch, M. Boehm, R. Goldstein, H. Javadi, P. Schuck, R. L. Arnoldy, and P. M. Kintner (2003), Multipoint measurements of field-aligned current density in the auroral zone, *J. Geophys. Res.*, 108, 1217, doi:10.1029/2002JA009450.

## Chapter 5 Inner-magnetospheric onset preceding reconnection during substorms<sup>4</sup>

### 5.1 Introduction

Substorms occur as the result of the interaction and coupling of the solar wind to the Earth's magnetosphere. Magnetic reconnection on the day-side extracts energy from the solar wind, this energy is stored in the night-side magnetosphere in the form of stretched field lines. As more energy is extracted and stored the tail become increasingly stretched and unstable, until a critical point is reached and the tail destabilises, explosively releasing the stored energy. This explosive release of energy is referred to as substorm expansion phase onset. In the ionosphere and in ground-based observations this is manifested as a sudden brightening of the aurora followed by the azimuthal and poleward expansion of the aurora [Akasofu, 1964], formation of magnetic bays in ground-based magnetograms [McPherron et al., 1973] and increased ionospheric riometer absorption [Brown, 1966]. In the magnetosphere, substorm expansion phase onset is characterised by an enhancement energetic particles (~10s-~100s keV) in the inner magnetosphere [e.g., Reeves et al., 1990], thickening of the plasma sheet [e.g., Baker et al., 1996; Miyashita et al., 2009], dipolarisation of the magnetic field [e.g., McPherron et al., 1973], and development of fast plasma sheet flows or bursty bulk flows (BBFs) [Angelopoulos et al., 1994]. These physical features have been associated with both onset of inner magnetospheric plasma instabilities [Lui, 1996] and the formation of a near-Earth X line and onset of reconnection [Baker et al., 1996]. However, despite both the ionospheric and magnetospheric signatures being extremely well characterised, the substorm expansion phase, time sequence of events, and in particular the process (or processes) initiating the onset of the expansion phase continues to be hotly debated [see for instance, Angelopoulos et al., 2008; Lui, 2009; Angelopoulos et al., 2009].

Two models are currently favoured to explain the sequence of events and ionospheric and magnetospheric signatures of a substorm: the current disruption [e.g. Lui, 1996] or

---

<sup>4</sup> A version of this chapter is to be submitted for publication to the *Journal of Geophysical Research*. Murphy, K. R., et al. (2013), *Inner-magnetospheric onset preceding reconnection during substorms*.

near-Earth geophysical onset model [e.g., Erickson et al., 2000] and the near-Earth neutral line model [e.g. Baker et al., 1996]. In the current disruption or near-Earth geophysical onset model, substorm expansion phase onset is initiated by a localised instability leading to a diversion of the cross-tail current, auroral brightening and formation of the substorm current wedge (SCW) and dipolarisation of the tail. Candidate instabilities include ballooning modes [e.g., Roux et al., 1991; Voronkov et al., 1997], cross-field current instabilities [e.g., Lui et al., 1995], lower hybrid turbulence [e.g., Huba et al., 1977] and the growth of drift waves in the inner magnetosphere [e.g., Maynard et al., 1996a; Erickson et al., 2000]. In this model, a rarefaction wave propagates radially outward triggering the onset of reconnection at a near-Earth neutral line at times later than the initial onset which occurs earlier and closer to the Earth on closed field lines. The current disruption model and near-Earth geophysical onset model, is referred to as inside-out since the initial ionospheric and magnetospheric signatures of substorm onset map to the inner magnetosphere and are followed only later by reconnection which occurs further away in the magnetotail.

In the near-Earth neutral line model substorm onset is triggered by the onset of reconnection in a thin plasmashet at distances of  $\sim 20$  RE [e.g. Baker et al., 1996]. The onset of reconnection drives earthward flows in the form of BBFs which propagate radially inward toward the Earth. As these flows encounter the more dipolar field of the inner-magnetosphere they decelerate, disrupting the cross-tail current and leading to the formation of the SCW [e.g., Shiokawa et al., 1998] causing a dipolarisation of the magnetotail and consequent brightening of the aurora [e.g., Angelopoulos et al., 2008]. The near-Earth neutral line model is referred to as outside-in as the initial signature of substorm onset is in the magnetotail on stretched field lines. A modified near-Earth neutral line paradigm, proposed by Nishimura et al. [2010] suggests that an inward transport of plasma by BBFs generated by reconnection leads to a destabilisation of the inner magnetosphere. In this model, auroral brightening is preceded by both fast flows in the tail and associated auroral streamers [Nakamura et al., 2001] and is followed by the formation of the SCW and dipolarisation of the magnetotail.

Recent work has provided strong evidence for both the inside-out and outside-in substorm paradigms. Using the Time History of Events and Macroscale Interaction

during Substorms (THEMIS; Angelopoulos, 2008) All Sky Imagers (ASIs; Mende et al., 2008), Rae et al. [2009] demonstrated that the aurora initially brightens on closed field lines and subsequently expands azimuthally in wave-like fashion, or as auroral “beads” [c.f., Elphinstone et al., 1995; Donovan et al., 2007; Liang et al., 2008; Motoba et al., 2012]. In a follow up study, Rae et al. [2010] presented a detailed analysis of the growth rates and azimuthal wave numbers of the auroral beads and concluded, for the substorm studied, that the most likely process leading to the initiation of substorm onset was either the cross-field current instability or the shear flow or kinetic ballooning instability. Conversely, Angelopoulos et al. [2008] presented detailed in-situ and ground-based observations of a substorm and concluded that, for that particular substorm, onset was initiated by reconnection in the tail. Using a major conjunction of the THEMIS probes these authors demonstrated that signatures of reconnection in the tail proceeded auroral brightening, current disruption and the formation of the SCW in the inner magnetosphere (note also the comment by Lui [2009] and reply by Angelopoulos et al. [2009]).

In this paper we present detailed observations of two substorms on 9th April 2011 and develop a comprehensive characterisation of the ionospheric and magnetospheric signatures through substorm onset and into the substorm expansion phase. The initial development of the substorm in the ionosphere and inner magnetosphere is very similar for both substorms; however, the tail response in the outer magnetosphere is distinctly different for the two substorms. Based on ionospheric data both substorms clearly initiate on closed field lines in the inner magnetosphere, being followed by rapid azimuthal and poleward expansion characteristic of auroral onset. This is followed by the formation of ground-based magnetometer bays, increased ionospheric riometer absorption in the auroral zone, and an enhancement in energetic particle flux and reduction of magnetic field strength at geosynchronous orbit. Based on in-situ data the initial substorm shows no evidence of any changes in plasmashet morphology and no evidence of either earthward flows or plasma sheet expansion and magnetic dipolarisation associated with reconnection following the auroral onset. However, albeit after auroral onset, the second substorm shows a rapid thinning of the plasma sheet followed by a second auroral activation, a rapid expansion of the plasma sheet and the formation of high-latitude magnetometer bays and enhanced riometer ionospheric

absorption. Prior to or even at auroral onset there is no evidence of earthward plasmashet flows or associated auroral streamers for either of the substorms. We interpret these observations as strong evidence that these particular substorms are initiated in the inner magnetosphere, most-likely by a localised plasma instability. Only during the second substorm is reconnection triggered further down tail in the plasmashet, with consequent changes in magnetotail morphology, but even for this case these changes follow significantly later than the initial auroral onset. These observations have important implications for any substorm model. In particular, they suggest that substorms can be initiated in the inner magnetosphere preceding magnetic reconnection and that earthward plasma flows or associated auroral streamers are not a necessary condition for initiating substorm onset.

## 5.2 Instrumentation

We present detailed observations of the dynamics and onset of two consecutive substorms on the 9th April 2011 in order to examine the sequence of events in the ionosphere and magnetotail through the substorm growth and expansion phases. Between 04:00-07:00 UT the three THEMIS probes (A, D, and E; Angelopoulos, 2008) were in the night-side magnetosphere in good magnetic conjunction with ground-based instrumentation in the North American sector. **Error! Reference source not found.** shows the north-magnetic foot prints of the THEMIS probes and the Geostationary Operational and Environment Satellites (GOES; Singer et al., 1996) 13 and 15 during the conjunction, as well as the location of ground-based instrumentation used in this study.

The blue, orange, and red traces in **Error! Reference source not found.** illustrate the north magnetic foot prints of THEMIS A, E, and D between 04:00-07:00 UT, respectively (traced with Tsyganenko 89 with KP of 3; Tsyganenko, 1989). The THEMIS fluxgate magnetometers [Auster et al., 2008] provide in-situ observations of the terrestrial magnetic field and the electrostatic analyzer (ESA) provides measurements of magnetospheric plasma [McFadden et al., 2008] at 3 s cadences. For the purpose of this study the direction of in-situ plasma flows are rotated into a field aligned coordinate system derived from a 15 minute running average of the magnetic field. In this coordinate system the radial position vector,  $r$ , points outward from the earth and the  $z$  component is aligned with the background field, the  $y$  component of the field is defined

by the cross-product of z and r (approximately azimuthal) and the x component completes the orthogonal coordinate system.

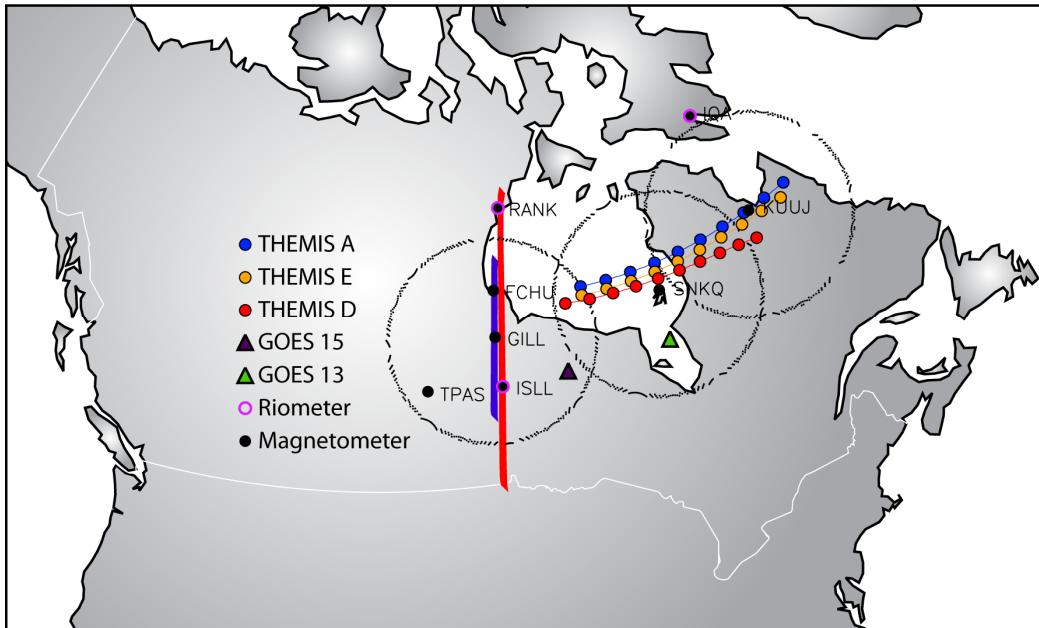


Figure 5.1: The location of ground-based instrumentation and in-situ spacecraft on 9th April 2011. The blue, orange, and red traces show the location of THEMIS A, E and D, respectively, between 4 and 7 UT, traced to the northern hemisphere. The THEMIS probes travel east to west and each circle marks a half hour interval. The purple and green triangles show the north magnetic footprints of GOES 15 and 13, respectively. The large black circles show the field of view of the GILL, SNKQ, and KUUJ THEMIS ASIs. The black circles and pink outlines mark the location of ground-based magnetometer and riometers, respectively.

The purple and green triangles in **Error! Reference source not found.** show the north magnetic foot prints of GOES 15 and 13, respectively (traced with Tsyganenko 89 with KP of 3; Tsyganenko, 1989). The GOES satellites provide measurements of the inner magnetospheric magnetic field and energetic electron and ion flux. Magnetic field measurements are provided by the onboard fluxgate magnetometers at 0.512 s cadence in the PEN spacecraft coordinate system. P is perpendicular to the orbital plane, E is perpendicular to P and directed earthward, and N completes the right hand set and is directed eastward (similar to the geocentric solar ecliptic coordinate system). Measurements of the electron and ion flux are provided by the Magnetospheric Electron and Ion Detector (MAGED and MAGPD) at 5 energy channels spanning the range 40-475 keV for electrons and 95-575 keV for ions with 9 look directions. For brevity, we use a single look direction (anti-earthward).

Ground-based observations of the aurora, the Earth's magnetic field and riometer absorption allow large two-dimensional regions and structures of the ionosphere to be probed through the substorm growth and expansion phases. The large dotted black circles in **Error! Reference source not found.** depict the field of view (mapped to 110 km) of select white light imagers from the THEMIS All Sky Imager (ASI) array providing detailed images of the aurora at a 3 s cadence [Mende et al., 2008]. The THEMIS ASIs utilise a fisheye lens to maximise the field of view of the imagers; however this can also skew auroral forms at the edge of the field of view. To limit this distortion the keograms presented in this paper are constructed by selecting a specific range of geomagnetic latitude and longitude within the field of view of the ASI (mapped to 110 km). This section of the ASI is then divided into equally spaced latitudinal bins and the intensity of each bin is calculated as the average pixel intensity. This keogram hence provides 1-D observations of the aurora as a function of geomagnetic latitude and constant geomagnetic longitude. A similar east-west keogram is constructed providing 1-D observations of the aurora as a function of geomagnetic longitude and constant geomagnetic latitude [c.f., Donovan et al., 2008].

The blue and red segments illustrate the field of view of the Gillam (GILL) NORSTAR meridian scanning photometer at 486 nm (proton aurora) and 630 nm (electron aurora) wavelengths, respectively [Donovan et al., 2003]. The proton aurora is mapped to height of 110 km. The location of the peak in intensity of the proton aurora is used to infer the transition between dipole and tail-like field topologies in the magnetosphere [Samson et al., 1992]. The electron aurora is mapped to a height of 230 km. The poleward edge of the electron aurora is used to infer the approximate latitude of the open-closed field line boundary [Blanchard et al., 1995] as described in detail in Murphy et al. [2012; see also, Rae et al., 2004].

The small black circles show the location of select magnetometers from the Canadian Array for Realtime Investigations of Magnetic Activity (CARISMA) [Mann et al., 2008], THEMIS [Russell et al., 2008] and Canadian Magnetic Observatory System (CANMOS) networks. The magnetometer data is presented in H (magnetic north), D (magnetic east) and Z (vertical) coordinates at 0.5 s cadence. The pink circles in **Error! Reference source not found.** show the location of select riometers which are part of the Natural

Resources Canada (NRCAN) and NORSTAR arrays. The riometer data has been detrended by removing a quiet day background to show enhancements in ionospheric absorption through the substorm growth and expansion phases.

### 5.3 Observations

Figure 5.2 presents an overview of THEMIS-A (a and b), GOES 15 geosynchronous (c and d), and ground-based ASI (e) and magnetometer observations (f) between 04:00-07:00 UT on the 9th April 2011. During this time period there are a number of auroral activations that can be identified in the auroral intensity (Figure 5.2e). For the purpose of this study we are interested in auroral activations that are followed by both poleward and azimuthal expansion which can be classified as substorms [Akasofu, 1977 and references therein]. These substorms are highlighted by the grey boxes between 04:15-04:45 UT and 05:30-06:30 UT, and the initial auroral activations are identified by the dashed lines. Both substorms are associated with a typical substorm injection (or energetic particle flux enhancement) at geosynchronous orbit (Figure 5.2d) auroral brightening and azimuthal expansion (Figure 5.2e) and the formation of auroral zone magnetometer bays (red line Figure 5.2f). However, the initial event has no characteristic dipolarisation at geosynchronous orbit, rather the field strength decreases following onset (black line Figure 5.2c).

The second event is characterised by two auroral activations, one around 05:36 UT and a second around 05:52 UT. For the first activation a clear dipolarisation is seen at geosynchronous orbit, accompanied by energetic particle injections, riometer absorption, and auroral zone bays. Only the second activations show clear higher latitude bays associated with higher latitude auroral activations. The second substorm is also characterised by large amplitude plasma flows observed by THEMIS-A (red line Figure 5.2a), and the formation of latitude magnetometer bays following the plasma flow (blue line Figure 5.2f). In addition the second substorm is followed by a dynamic change in the plasma sheet (Figure 5.2b) which can be contrasted with no changes in the plasma sheet during the first substorm. Following onset, during the second substorm, the plasma sheet thins and subsequently thickens following the second auroral activation (Figure 5.2e). In the subsequent sections we present a detailed analysis of the aurora, and data from ground-based magnetometers and riometers and in-situ

observations to compare and contrast the two substorms and develop a comprehensive understanding of sequence of events observed during each substorm.

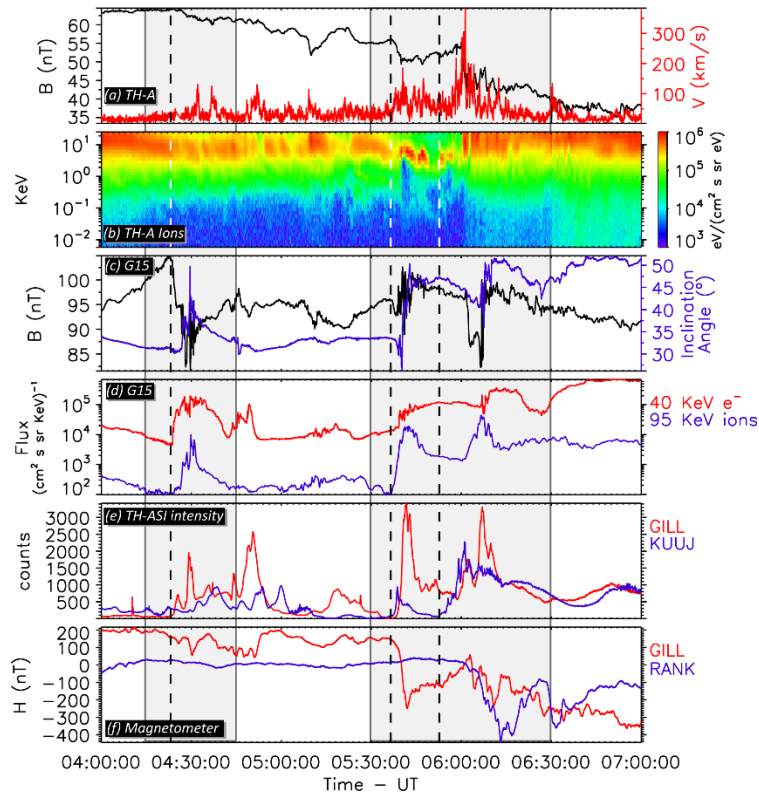


Figure 5.2: Overview of the in-situ and ground-based observations on 9<sup>th</sup> April 2011. The grey panels highlight the periods of interest. The first dashed line marks auroral onset during the first substorm. The second dashed line marks auroral onset in the second substorm and third dashed line mark a second auroral activation during the second substorm. (a) THEMIS A magnetic field strength (black) and magnitude the ion velocity (red). (b) THEMIS A ion flux. (c) GOES 15 magnetic field strength (black) and inclination angle (blue). (d) GOES 15 40 KeV electron flux (red) and 95 KeV ion flux (blue). (e) THEMIS ASI average intensity from the GILL (red) and KUUJ (blue) ASIs. (f) Ground-based magnetometer observations of the H-component from the GILL and RANK magnetometers.

### 5.3.1 Substorm 1, 04:15-04:45 UT

Figure 5.3 shows auroral observations from the Gillam (GILL) MSP (a) and ASI (b and c) through substorm expansion phase onset during the first substorm. Figure 5.3a shows H-beta proton aurora (486 nm) from the GILL MSP, the asterisks mark the location of the peak in the proton aurora characteristic of the transition between dipole to stretched field in the night-side magnetosphere [Samson et al., 1992]. Figure 5.3b shows the GILL ASI keogram; the peak in the proton aurora and poleward edge of the electron aurora derived from the GILL MSP are overplotted as white and green circles, respectively. The

bottom panel of Figure 5.3 shows the longitudinal expansion and beading of the aurora through expansion phase onset as characterised by an east-west keogram derived from the GILL ASI. Detailed analysis of the initial brightening and beading of the aurora places substorm onset at 04:23:06 UT at 64.8° corrected geomagnetic (CGM) latitude, depicted by the dashed line in each panel. The initial beading occurs on spatial scales of  $\sim 1^\circ$  in longitude and subsequently expands to larger and larger spatial scales (Figure 5.3c) [c.f., Rae et al., 2009]. Figure 3b clearly demonstrates that auroral onset occurs below the poleward edge of the electron aurora, on closed field lines in the transition region between dipole and stretched field topologies, and on the most equatorward arc. Following auroral onset the aurora expands poleward and azimuthally over nearly 6 hours of MLT (Figure 5.3 a and b). The proton aurora, however, shows little poleward motion following onset. Based on the stability of the plasmasheet boundaries inferred from the auroral observations this suggests that no dynamic change of the inner magnetosphere, such as a dipolarisation, has occurred as the boundary between the dipole and tail field remains largely unchanged. This is consistent with the observations of the plasmasheet seen by THEMIS which remain unperturbed during this time. Note that there is no evidence of latitudinally extended equatorward propagating auroral features characteristic of an auroral streamer [Nakamura et al., 2001], in either the GILL ASI or surrounding ASIs.

Figure 5.4 shows selected ground-based magnetometer and riometer observations (see **Error! Reference source not found.**) during the first substorm, top and bottom panels respectively. The auroral zone ground-based magnetometers, GILL, Sanikiluaq (SNKQ) and Kuujuaq (KUUJ), show clear evidence of a substorm growth phase preceding onset. This is depicted by the development of convection bays [Erickson and Wolf, 1980; Hau et al., 1989], and the negative slope in the H-component magnetograms corresponding to the enhancement of the ionospheric electrojet system [McPherron, 1970] preceding substorm onset. Following auroral onset the GILL and SNKQ auroral zone and lower latitude ISLL magnetometer show the development of a substorm bay and the substorm current wedge (SCW) [McPherron et al., 1973]. The high latitude Rankin Inlet (RANK) and Iqaluit (IQA) magnetometer show no evidence of substorm bays or the SCW following auroral onset. Just prior to expansion phase onset the Island Lake (ISLL) riometer, Figure 5.4b, shows the characteristic absorption signature associated with

substorms [e.g. Brown, 1966; Baker et al., 1982] while the higher latitude RANK and IQA riometers show no evidence of ionospheric absorption.

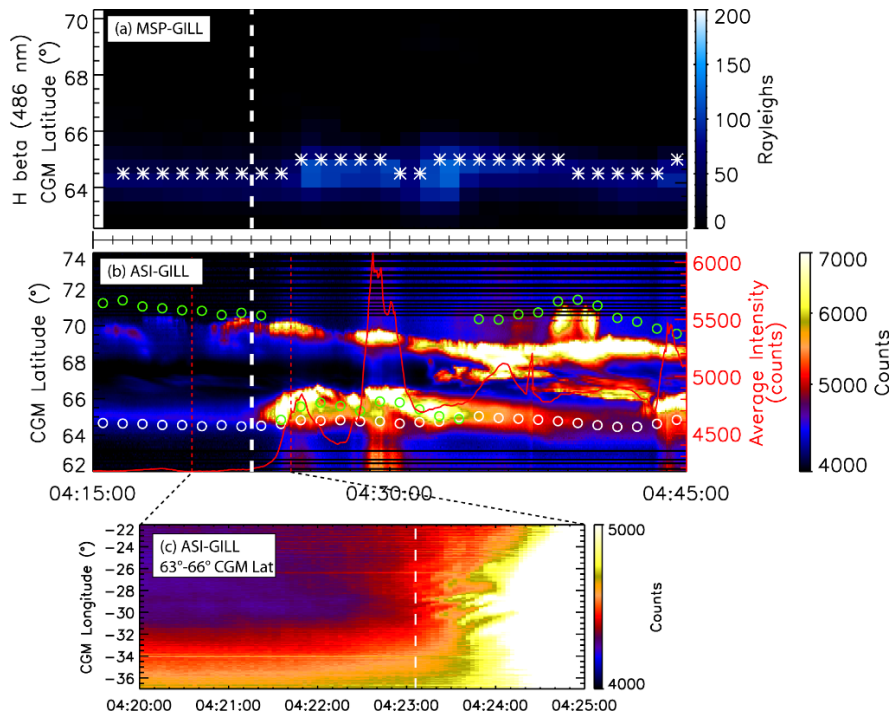


Figure 5.3: Aurora observations from the GILL MSP and ASI during the initial substorm. (a) GILL MSP observations of the proton aurora H-beta (486 nm), overplotted as asterisks is the peak in the intensity of the proton aurora. (b) North-south keogram from the GILL ASI, overplotted as white and green circles are the latitude of the peak in the proton aurora poleward edge of the electron aurora derived from data from the GILL MSP and the average intensity of the ASI (red). (c) East-West keogram from the GILL ASI showing the initial development of auroral beads at onset. The dashed white line marks auroral onset.

Figure 5.5 is a summary of ground-based measurements and key in-situ observations. For brevity we have only included THEMIS-A of the three THEMIS probes which, due to their close proximity, observe similar phenomena and field topologies during the first substorm. The top two panels summarise the ground-based ASI (a) and magnetometer and riometer (b) observations. The bottom four panels, c through h, summarise the in-situ observations from GOES 13 and 15 and THEMIS-A. The dashed line through all panels marks auroral substorm onset at 04:23:06 UT. For this particular substorm, auroral onset in the GILL ASI is closest to the magnetic footprint of the GOES 15 satellite and the THEMIS probes lie approximately in the midnight meridian at ~4 UT conjugate to the KUUJ ASI.

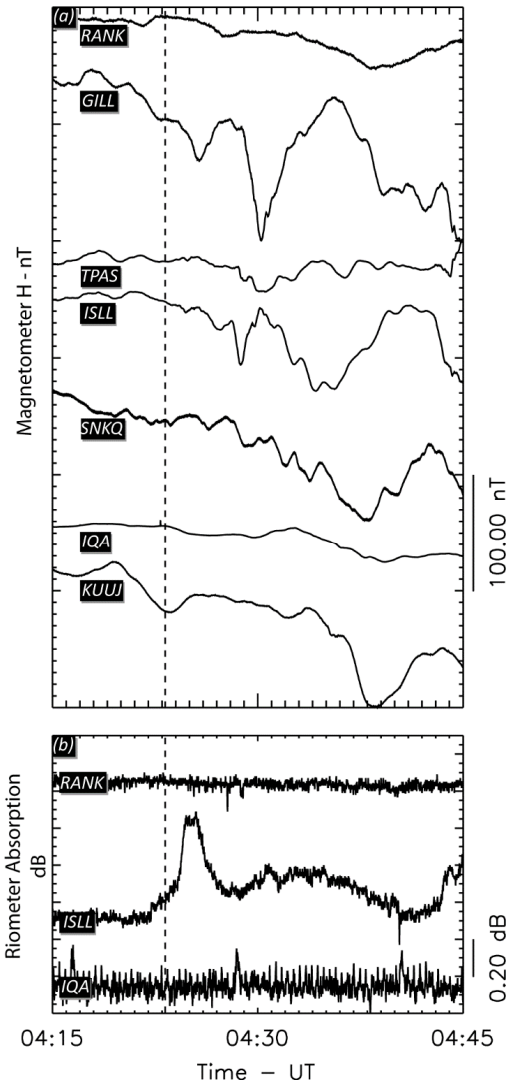


Figure 5.4: (a) Select H-component magnetometer observations during the first substorm. Major tick marks represent 100 nT and minor tick marks 10 nT. (b) Riometer absorption from the RANK, ISLL and IQA riometers. Major tick marks represent 0.2 dB. The dashed line marks auroral onset.

Evident in the GOES and THEMIS data is the fact that all magnetospheric signatures of the substorm expansion phase follow auroral onset. An enhancement of energetic electron and ion flux is observed initially at GOES 15, nearly conjugate to auroral onset, and to the east at GOES 13 (see Figure 5.5 c and d, respectively). Similarly, just following auroral onset there is a decrease in the magnetic field strength, Figure 5g, and an increase in the inclination angle, Figure 5.5h, at GOES 15 followed later by a similar feature at GOES 13. The increase in the inclination angle is characteristic of a substorm dipolarisation, however the decrease in the magnetic field strength suggests this change is the result of stretching or inflation of the geosynchronous field rather than a

dipolarisation. Interestingly, the increase in the inclination angle at GOES 13 occurs several minutes following that GOES 15, although this is perhaps associate with a second increase in the inclination angle at GOES 15.

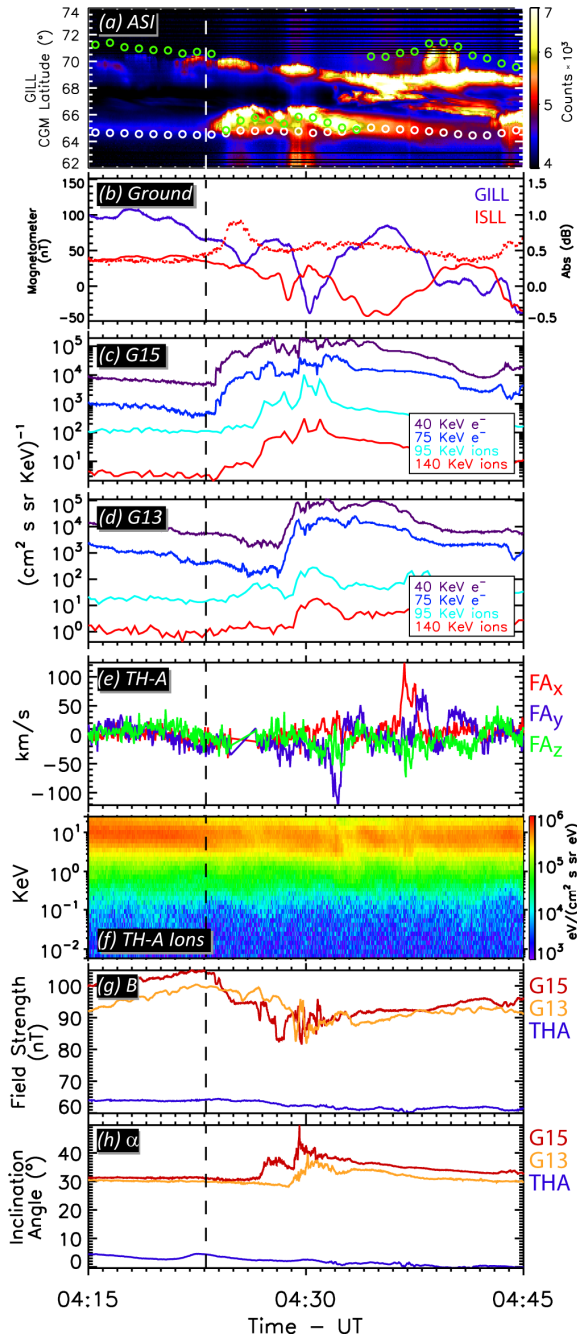


Figure 5.5: Select ground and in-situ observations during the first substorm. (a) North-south keogram from the GILL ASI overplotted with MSP boundaries in the same format as Figure 3b. (b) H-component magnetometer observations from the GILL (blue) and ISLL (red) magnetometers (left axis) and absorption from ISLL riometer (dotted red line, right axis). (c) Select energetic ion and electron fluxes from the GOES 15 MAGPD and MAGED instruments. (d) Same as (c) for GOES 13. (e) Field aligned ion bulk flow from the THEMIS A probe. (f) ESA ion differential flux from THEMIS A probe. (g) Magnetic field strength from THEMIS A (blue), GOES 13 (orange), and GOES 15 (red). (h) Magnetic field inclination angle from THEMIS A (blue), GOES 13 (orange), and GOES 15 (red).

THEMIS-A in the plasma sheet (Figure 5.5e) at a radial distance of 8.9 RE and east of GOES 13 shows no clear substorm signature. Just following auroral onset the field continues to stretch (blue line Figure 5.5g). Small fluctuations of the ion plasma are

observed following onset (Figure 5.5f); however for the duration of the first substorm all three THEMIS probes remain in the plasma sheet with no obvious changes to plasma sheet morphology. At the THEMIS locations in the plasmashet there is no dipolarisation [McPherron et al., 1973], flux transport [Sergeev et al., 2012], onset of fast flows [Angelopoulos et al., 1994] or expansion of the plasmashet, or flux pile up [Baker et al., 1996]. A small data gap does exist in the THEMIS-A plasma flow following substorm onset, Figure 5.5e. However, prior to the data gap there is no evidence of enhanced plasma flow preceding auroral onset at THEMIS A, D or E (note there is no data gap in either THEMIS D or E). At 8.9 RE it is interesting to note that THEMIS A is only approximately 2 RE tailward of geosynchronous altitudes and yet sees very different features to GOES 15 and 13 through onset. THEMIS A is clearly in the plasmashet and GOES 13 and 15 are on significantly more dipolar fields despite their proximity.

In summary, in the ionosphere the substorm shows the classical substorm signature. The initial brightening of the aurora is localised to closed field lines and expands azimuthally in wave-like fashion. This is followed by the poleward expansion of the aurora and formation of the westward travelling surge (WTS), increased ionospheric riometer absorption localised to auroral latitudes and development of the SCW. In the magnetosphere the substorm signatures are confined to geosynchronous orbit. The THEMIS probes, close to the midnight meridian and only ~2 RE tailward of GOES, observe continued stretching of the tail and no evidence of the substorm expansion phase in the form of changes to plasmashet ion flux, indicating no obvious dipolarisation or rapid changes to plasmashet morphology. At geosynchronous orbit there is an enhancement of energetic ions and electrons which propagates west to east. However, rather than dipolarising the geosynchronous magnetic field strength decreases following onset, consistent with the H-Beta auroral observations. The enhancement of energetic particles at geosynchronous is characteristic of a dispersionless injection [e.g., Reeves et al., 1990], however there is no signature of any particle enhancement at THEMIS suggesting that the energetic particle enhancement is localised and begins inside the altitudes of the THEMIS probes. The injection subsequently propagates azimuthally but no radially propagating injection or dipolarisation front is seen at THEMIS altitudes in the plasmashet [c.f., Reeves et al., 1996].

### 5.3.2 Substorm 2, 05:30-06:30 UT

Figure 5.6 presents a summary of auroral observations for the second substorm from the KUUJ and SNKQ ASIs and the GILL MSP. The top three panels are keograms from the KUUJ and SNKQ ASIs, and the proton aurora from the GILL MSP, respectively, in the same format as Figure 5.3. The bottom panels are east-west keograms highlighting the two discrete auroral activations; auroral onset (left) and the second during the expansion phase (right). Auroral onset occurs at SNKQ, Figure 5.6f, at 05:36:30 UT at 65.2° degrees CGM latitude marked by the white dashed line. Similar to the first substorm, and based on MSP data, auroral onset occurs on closed field lines and just poleward of the transition between dipole and stretched magnetic field, Figure 5.6b. The initial auroral expansion begins in the form of small scale auroral beads with initial azimuthal spatial scales of  $\sim 1^\circ$  (Figure 5.6e) which subsequently expand poleward (Figure 5.6b) and azimuthally (Figure 5.6 e-f) [c.f. Rae et al., 2009]. Following auroral onset there is a sharp transition in the proton aurora (Figure 5.6c) to higher latitudes starting at 05:41:30-05:42:30 UT, characteristic of a dipolarisation as the boundary between dipole and stretched field moves radially outward in the night-side magnetosphere. Note that there is no evidence of north-south aligned auroral streamers believed to be associated with Earthward magnetotail plasma flow [Nakamura et al., 2001] prior to auroral onset.

A second auroral activation is observed during the substorm expansion phase, initially at KUUJ at 05:52:39 (Figure 5.6 a and f) and marked by the yellow dashed line, which subsequently propagates west to SNKQ (Figure 5.6 b and g). Similar to the onset of both the first substorm and this one, during the second activation the aurora brightens and begins to bead with azimuthal spatial scales of  $\sim 1^\circ$  along the peak in the proton aurora. Note significantly that this second activation occurs at a higher latitude, 67.3° CGM (Figure 5.6a), as might be expected following the initial dipolarisation after aurora onset. This second activation is also associated with continued poleward motion of the proton aurora.

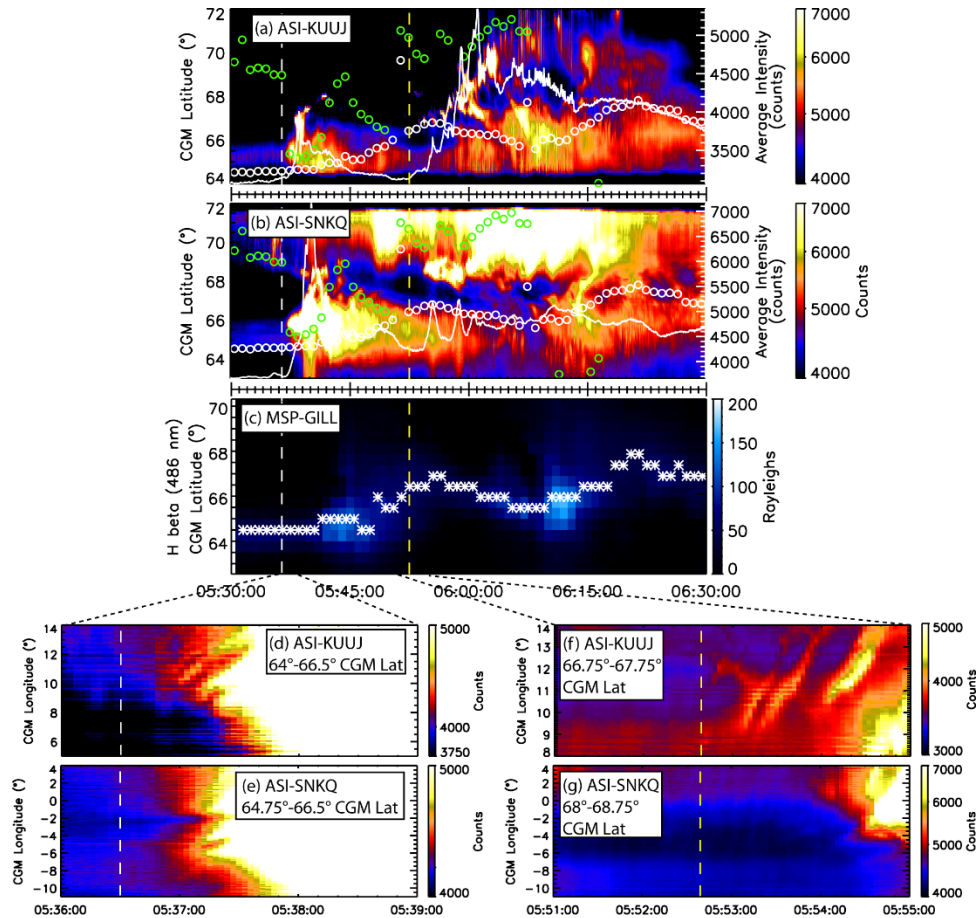


Figure 5.6: Auroral observations during the second substorm. (a) North-south keogram from the KUUJ ASI in the same format as Figure 3(b). (b) North-south keogram from the SNKQ ASI in the same format as Figure 3(b). (c) Proton H-beta aurora from the GILL MSP in the same format as Figure 3(a). (d) and (e) East-west keograms from the KUUJ and SNKQ ASIs during the initial auroral activation. (f) and (g) East-west keograms from the KUUJ and SNKQ ASIs during the secondary activation. The dashed white line marks auroral onset at SNKQ and the dashed yellow line marks the secondary auroral activation at KUUJ.

Figure 5.7 shows conjugate magnetometer and riometer observations during the second substorm. Following the initial auroral onset at SNKQ at 05:36:30 UT (first dashed line) large amplitude magnetic bays form at the auroral stations GILL, SNKQ, and KUUJ and lower latitude ISLL and The Pas (TPAS) magnetometers. Similarly, following the second activation at KUUJ at 05:52:39 UT (second dashed line) an additional bay begins to form at the KUUJ magnetometer. No high-latitude magnetic activity (RANK and IQA) is observed until much later in the substorm expansion phase around 6 UT following the second activation. Following auroral onset the lower-latitude ISLL riometer shows significant absorption, while the higher latitude RANK and SNKQ riometers show no evidence of absorption until much later in the expansion phase.

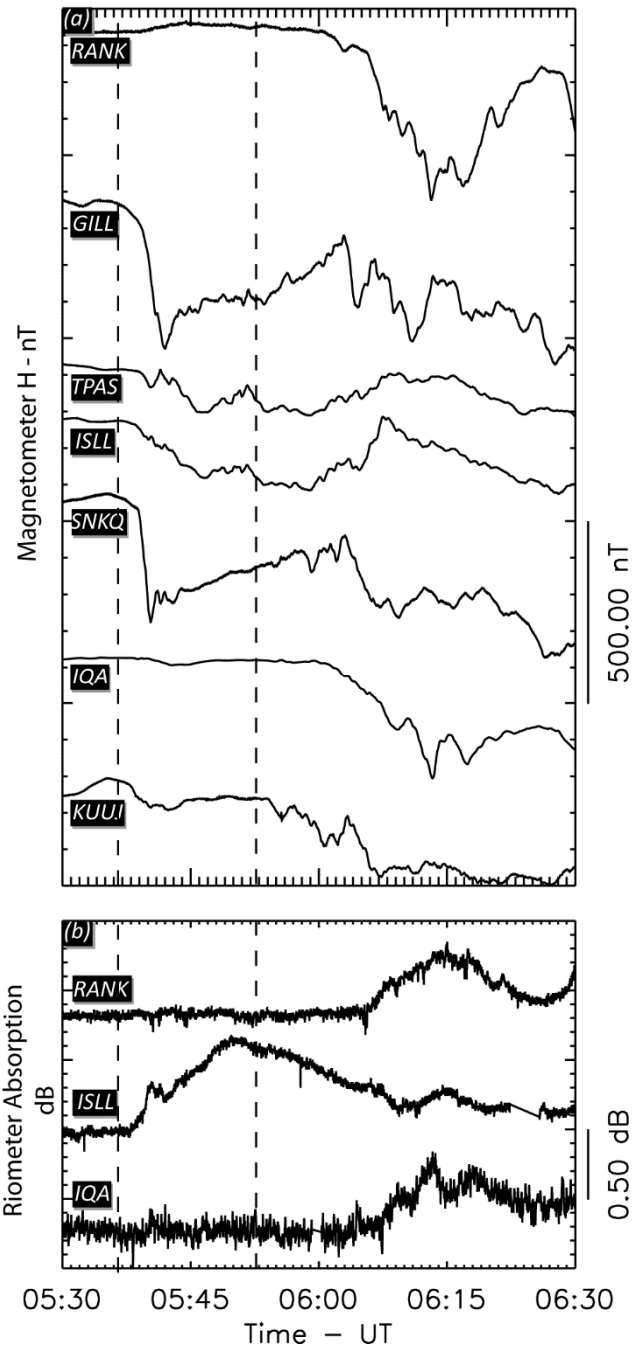


Figure 5.7: Select ground-based magnetometer and riometer observations during the second substorm. (a) H-component magnetometer, major ticks represent 500 nT. (b) Riometer absorption, major ticks represent 0.5 dB. The first dashed line marks auroral onset and the second dashed line marks the secondary auroral activation during the second substorm.

Similar to the first substorm, the magnetospheric signatures of the substorm expansion phase all follow auroral substorm onset. Figure 5.8 presents a summary of select ground-based observations and key in-situ observations from GOES 13, 15 and THEMIS-

A. The black dashed lines mark auroral onset at SNKQ and the second auroral activation at KUUJ. Following auroral onset GOES 13 and 15 observe a brief decrease in the local magnetic field strength (Figure 5.8h) and an enhancement in energetic electron and ion flux at 05:38:00 UT (GOES 13, Figure 5.8e) and 05:39:16 UT (GOES 15, Figure 5.8d). This is followed by a clear dipolarisation in the magnetic field (Figure 5.8h) and a coincident increase in the inclination angle (Figure 5.8h) between 05:39:35-05:40:30 UT at GOES 13 which propagates west toward GOES 15 at 05:40:00-05:42:15 UT. The dipolarisation at GOES 15 occurs coincident in time with the poleward motion of the proton aurora at the nearly conjugate GILL MSP. At THEMIS-A, located at a radial distance of  $9.9 R_E$  and mapping to longitudes between GOES 13 and 15 in the midnight meridian, the magnetic field and plasma sheet thin following auroral onset, apparent as a decrease the strength of the magnetic field and plasma sheet excursions seen in the ion flux at THEMIS-A (Figure 5.8 g and h) [c.f., Angelopoulos et al., 2008]. This thinning is followed by a small amplitude field-aligned flow at 05:40:00 UT (Figure 5.8f), subsequent to the low energy electron enhancements at both GOES 13 and 15 (Figure 5.8 d and e).

The second auroral activation observed at KUUJ at 05:52:39 UT is followed by an expansion of the plasma sheet, observed by the three THEMIS probes (Figure 5.8g), and an enhancement in ion flux at GOES 13 and 15 (Figure 5.8 d and e). The expansion of the plasmasheet is associated with high-speed field aligned flows at the THEMIS probes (Figure 5.8f) and the formation of ground-based magnetic bays at the high-latitude RANK and IQA stations followed by an enhancement of the auroral zone magnetic bays at SNKQ and KUUJ, Figure 5.8b. Similar high-latitude riometer absorption signatures are observed by the RANK and IQA riometers following the expansion of the plasma sheet (Figure 5.8c).

Figure 5.9 shows detailed observations of the plasma sheet and ion dynamics during the second substorm from THEMIS A, E and D and GOES 15 and 13. Following the initial auroral onset all three THEMIS probes observe a clear thinning of the plasma sheet (Figure 5.9 a-c), while both GOES 15 and 13 observe an enhancement in the ion flux (Figure 5.9 g and i) and electron flux (Figure 5.8 d and e) associated with a geosynchronous dipolarisation. Following the second auroral activation a significant global reconfiguration of the magnetotail is observed. The plasma sheet expands,

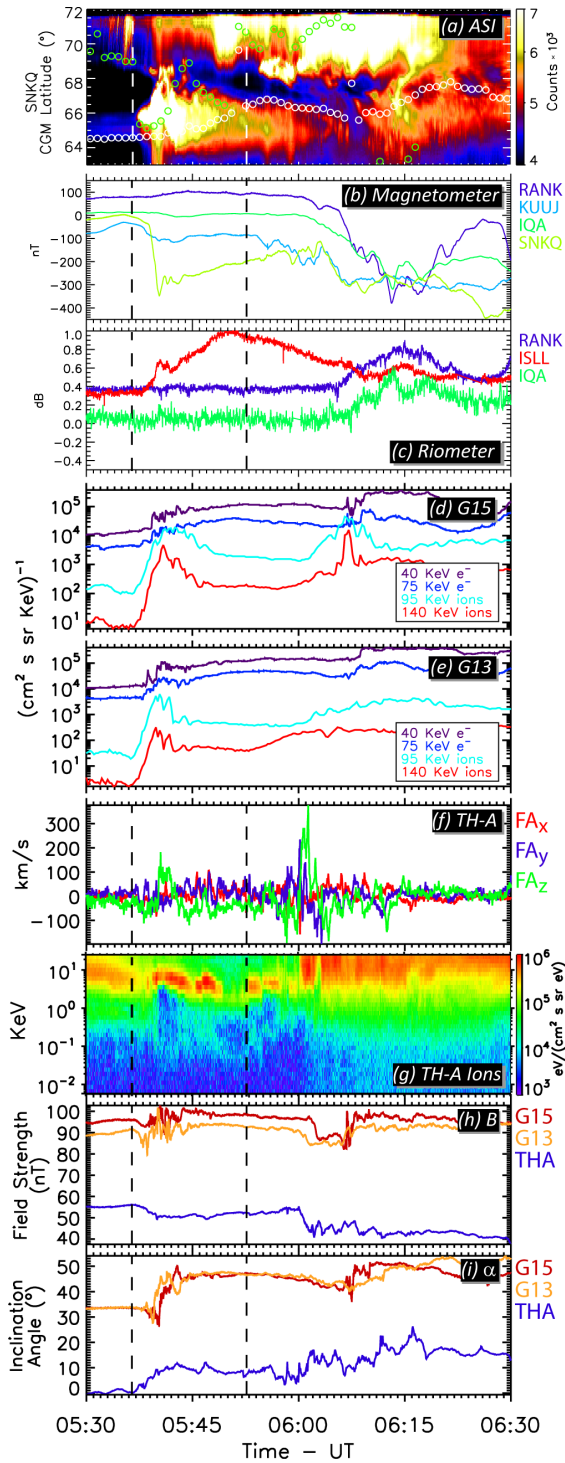


Figure 5.8: Select ground-based and in-situ observations during the second substorm. The initial dashed line marks auroral onset and the second dashed line marks the time of the secondary auroral activation. (a) North-south keogram from the SNKQ ASI. (b) H-component magnetometer traces. (c) Riometer absorption. (d) Select energetic ion and electron fluxes from GOES 15. (e) Same as (d) for GOES 13. (f) Field aligned plasma flow from THEMIS A. (g) Differential ion flux from THEMIS A. (h) Total magnetic field strength from THEMIS A, GOES 13, and GOES 15. (i) Magnetic field inclination angle from THEMIS A, GOES 13, and GOES 15.

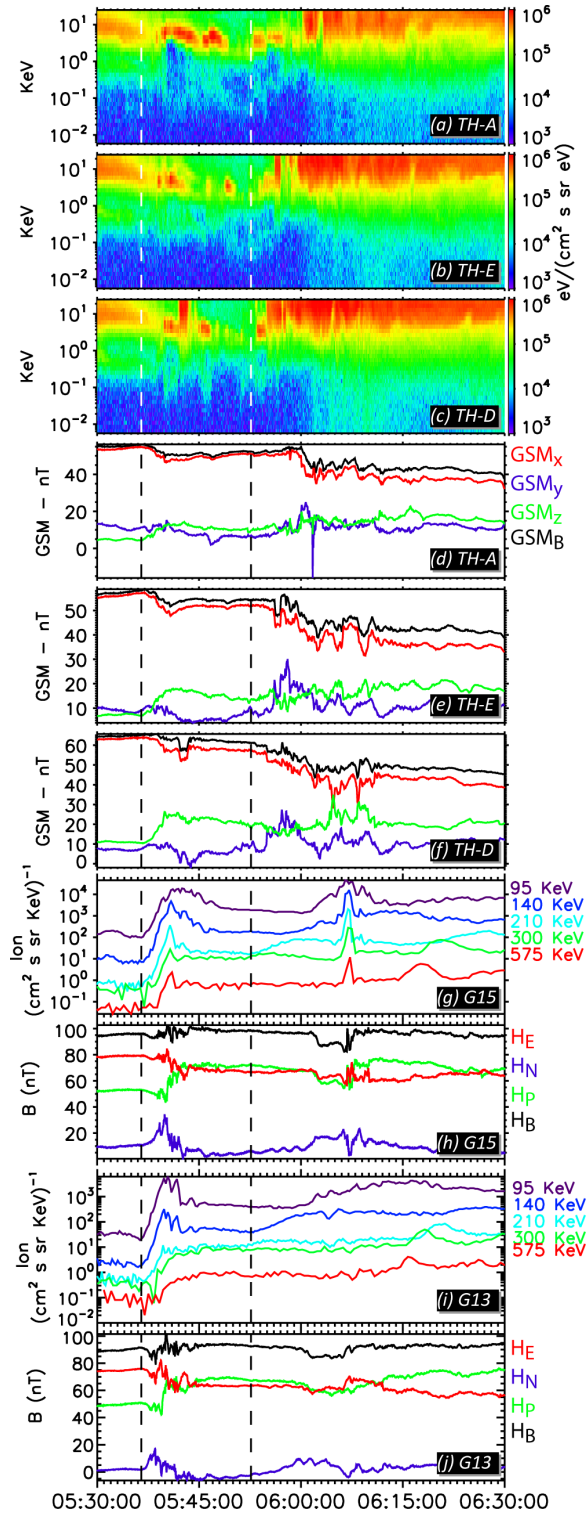


Figure 5.9: Observations of the ion plasma sheet from THEMIS A, E, D, GOES 15 and GOES 13 during the second substorm. The initial dashed line marks auroral onset and the second dashed line marks the time of the secondary auroral activation. (a-c) Energetic ion flux from THEMIS A, E and D, respectively. (d-f) GSM magnetic field at THEMIS A, E and D, respectively. (g) Energetic ion flux from GOES 15. (h) PEN magnetic field from GOES 15, see text for description of coordinate system. (i) Same as (g) for GOES 13. (j) Same as (h) for GOES 13.

observed initially by THEMIS D, closest to the neutral sheet, followed by E and A, respectively. At each of the THEMIS probes the expansion of the plasma sheet is followed by a sharp decrease in the magnetic field strength and dipolarisation of the local field and formation of high-latitude magnetometer bays on the ground and ionospheric absorption.

The second substorm has a nearly identical ionospheric response to the first substorm onset. However, the magnetospheric response in each case is very different. In summary, for the second substorm the aurora initially brightens on closed field lines, starting from a localised region and expanding in a wave-like fashion azimuthally. This initial brightening is followed by poleward expansion, the formation of the westward travelling surge, enhanced riometer ionospheric absorption and development of the SCW. At geosynchronous orbit there is a decrease in the magnetic field strength and enhancement in energetic particles followed by a rapid dipolarisation. Similar to the first event the lack of any particle enhancement or flow at the THEMIS probes prior to the geosynchronous particle enhancement suggests that the enhancement in energetic particles at geosynchronous orbit is the result of a localised process which is not associated with any injection or Earthward propagation of a dipolarisation front at THEMIS altitudes in the tail. The initial auroral brightening is followed by a rapid thinning of the plasma sheet, and subsequently a secondary auroral activation which is followed by a rapid expansion of the plasma sheet and increased ionospheric riometer absorption and formation of magnetometer bays at higher-latitudes on the ground.

## **5.4 Discussion**

The physical process which triggers substorm expansion phase onset and the subsequent sequence of events has been the subject of considerable controversy. Recent observations have presented evidence that substorm expansion phase onset is initially triggered in the inner magnetosphere [e.g., Rae et al., 2009] potentially driven by localised plasma instability [e.g., Rae et al., 2010]. However, similar studies of other substorms have come to the opposite conclusion suggesting that substorm expansion phase onset is initiated by reconnection in the tail [e.g., Angelopoulos et al., 2008]. In addition, a modified reconnection paradigm has been presented which suggests that an inward transport of plasma by high velocity flows generated via tail reconnection may

lead to a destabilization of the tail at the near-Earth boundary of the plasmashet and hence to the onset of the substorm expansion phase [Nishimura et al., 2010]. In this paper we have presented a detailed multi-point study of two substorms on the 9th April 2011. In particular we demonstrated that during these substorm events:

- Auroral onset occurs on closed field lines near the peak in the proton aurora.
- Auroral onset develops initially as wave-like auroral beads which propagate azimuthally with an azimuthal wavelength of  $\sim 1^\circ$ .
- Auroral onset is followed by auroral-zone and mid-latitude magnetometer bays and enhanced ionospheric riometer absorption.
- No clear Earthward magnetotail flows are observed prior to auroral onset.
- In the case of the second substorm, post-onset, there is a clear expansion of the plasmashet and reconfiguration of the tail are associated with a secondary high-latitude auroral activation and high-latitude magnetometer bays and enhanced ionospheric riometer absorption.

The two substorms presented here have very different magnetotail signatures, however the initial development of each substorm and the ionospheric and geosynchronous signatures right at onset are very similar. A localised brightening of the aurora and wave-like azimuthal expansion is followed by the formation of magnetic bays and an increase in ionospheric riometer absorption at auroral latitudes, and an enhancement of energetic ions and electrons and a decrease in the magnetic field strength seen at geosynchronous orbit. In both events there is no obvious preceding tail activity, such as fast flows or auroral streamers, despite having excellent coverage of the magnetotail with the THEMIS probes and clear skies in the ASI field of view. Only in the second event was there evidence of a global topological change of the magnetotail and indication of reconnection during the late expansion phase. These observations have important implications for any processes active in triggering substorm onset and for phenomenological models of the substorm. In particular, it suggests that substorm onset was initiated in the inner magnetosphere for both substorm presented here.

More significantly this indicates that earthward tail flows, such as BBFs or auroral streamers are not necessary for substorm onset.

The initial brightening and localisation of auroral onset on closed field lines prior to any tail activity is evidence of the likely action of an inner magnetospheric onset driven by a localised plasma instability in the inner magnetosphere, at, or very near geosynchronous orbit. The localisation of ionospheric riometer absorption and magnetometer bays to the auroral-zone and mid-latitudes, rather than at higher latitudes, is also consistent with an inner magnetospheric onset process. Similar auroral observations involving localised brightening and wave-like azimuthal expansion, have been reported by Elphinstone et al. [1995], Donovan et al. [2007], Liang et al. [2008], and Rae et al. [2009 and 2010]. These authors all concluded that substorm onset was likely the result of an inner magnetospheric instability which initiates in a localised region of the inner magnetosphere and evolves azimuthally along a region where the instability can continue grow. Further, Motoba et al. [2012] demonstrated these auroral forms were observed in both the northern and southern hemisphere at magnetically conjugate locations. These observations clearly indicate that the source of these auroral waveforms, and of the instability triggering onset, is located in the equatorial magnetosphere.

The rise in energetic particle flux and the initial decrease in the magnetic field strength at geosynchronous orbit, following auroral onset, is also characteristic of the development of a near-Earth plasma instability such as the ballooning mode [Roux et al., 1991]. Such an instability can lead to the heating and energisation of the local plasma, the generation of transient FACs and the modification of the magnetic field geometry [e.g., Roux et al., 1991; Voronkov et al., 1997]. The hot plasma results in a decrease in magnetic field strength in order to maintain total pressure. The development of transient FACs driven in regions of excess hot ions and electrons [Roux et al., 1991] also leads to increased ionospheric particle precipitation, deflection of the ionospheric magnetic field, and auroral intensifications (c.f., Figure 5.3, Figure 5.4 and Figure 5.5). According to this model these disturbances initially propagate azimuthally, along the boundary between dipole and tail-like field, just like the initial brightening of the aurora and disturbances at geosynchronous orbit. Such disturbances may also trigger the onset

of reconnection in the tail and changes in magnetotail and plasmashet morphology [Lui, 1996].

Recent work has suggested that the injection of plasma into the inner magnetosphere in the form of BBFs or dipolarisation fronts is a necessary condition for destabilizing the inner magnetosphere at substorm onset [Nishimura et al., 2010]. These authors postulate that the fast flows or BBFs, a result of reconnection further down tail, generate waves in the magnetosphere that lead to auroral intensifications observed in the ionosphere and subsequently to the onset of the substorm expansion phase. Despite the THEMIS probes being in the ideal location in the plasma sheet, neither of the substorms presented here show evidence of fast flows in the magnetosphere or their auroral counterparts in the ASIs, north-south aligned auroral streamers [Nakamura et al., 2001], prior to auroral onset. The lack of any tail flows or auroral streamers is clearly indicative of the conclusion that the inner magnetosphere does not require fast tail flows to destabilize at onset.

Plasma sheet flows are observed during the second substorm, during periods of plasma sheet thinning and thickening during the late expansion phase and following substorm onset. During the second substorm, the three THEMIS probes show a rapid thinning of the plasma sheet following auroral onset. As each probe exits the plasma sheet they observe high-speed field aligned flows most likely associated with beams in the plasmashet boundary layer [Walsh et al., 2011]. Following the later second auroral activation, at higher latitudes, the plasmashet rapidly expands, passing over the three THEMIS probes (Figure 5.9). The expansion of the plasma sheet is associated with a high-speed field-aligned flows, a magnetic field dipolarisation, and increased ionospheric riometer absorption at magnetic bays at high-latitudes on the ground (Figure 5.7). These signatures are characteristic of the onset of reconnection in the tail [e.g., Baker et al., 1996].

Proponents of the near-Earth onset model for substorms have suggested that a global constraint or threshold is required for the full development of the substorm expansion phase which includes large scale changes in the magnetotail and plasmashet triggered by the onset of reconnection further downtail [Lui, 1996]. This global constraint might be provided by a number of scenarios, dependent on the state of the magnetosphere

and ionosphere. In recent work magnetosphere-ionosphere (M-I) coupling has been shown to play an important role in destabilising the magnetosphere immediately prior to the substorm expansion phase onset. Murphy et al. [2012] showed a clear reduction in the strength of field-aligned currents local to and preceding auroral onset. These authors suggested this change in M-I coupling could play a significant role in the substorm onset process, perhaps preconditioning the system prior to onset [c.f. Millan et al., 2010] or leading to onset itself. Maynard et al. [1996a; see also Maynard et al., 1996b, 1997, 1998 and Erickson et al., 2000] postulated that the reflection of Poynting flux at the ionosphere following the onset of an inner magnetosphere instability played an important role during the development of the substorm expansion phase. If the reflected wavepacket constructively interfered with a second wavepacket a substorm occurs. Conversely if the waves destructively interfere a localised pseudo-breakup ensues without a full substorm. These observations provide strong evidence suggesting that M-I coupling has an important role to play in the substorm expansion phase, and that something as simple as the ionospheric conductivity at the foot point of the magnetospheric instability may be crucial in determining whether a full magnetospheric substorm develops [Lysak, 1991].

Alternatively, the global constraint might relate to the stability of the magnetosphere as a whole. As more and more energy is stored in the night-side magnetosphere the tail becomes increasingly stretched and the plasma sheet continues to thin. This creates two regions susceptible to energy storage and release; the inner magnetosphere through plasma instabilities, and the near-Earth tail through reconnection. If conditions in the inner magnetosphere are favourable for ballooning to become unstable [e.g., Roux et al.], for the development of lower hybrid turbulence [e.g., Huba et al., 1977], drift waves [e.g., Maynard et al., 1996a] or cross field current instabilities [e.g., Lui et al., 1995], then a substorm might be triggered in the inner magnetosphere. If conditions in the tail are suitable for magnetic reconnection then a substorm might be initiated by reconnection in the tail. In this concept, either or perhaps even both regions might become unstable depending on local plasma and magnetic field conditions. In other words free energy might be released from either or both regions leading to a substorm onset. Conceptually, each region once unstable might perturb the other leading to complex inter-region timings which vary from substorm to substorm. Indeed such a model might explain the

intensity of the substorm debate if one seeks a solution based on only one possible onset region.

## 5.5 Conclusions

In this manuscript we have presented detailed observations of two substorms. Both substorms initiate in the inner magnetosphere on closed field lines. The location of the auroral onset, azimuthal expansion of the aurora, enhancement of geosynchronous energetic particles, and wave-like development of the aurora during both events strongly suggests that these substorms were triggered by an inner magnetosphere plasma instability. Following auroral onset only the second substorm shows evidence of a global topological change of the night-side magnetotail and plasmashield which could be interpreted as the onset of tail reconnection following initial development of a plasma instability in the inner magnetosphere. During both events there is no clear evidence of fast flows or BBFs in the magnetotail at the THEMIS satellites nor of auroral streamers in the ionosphere preceding onset despite having excellent near-midnight magnetotail coverage with the THEMIS probes and clear viewing conditions in the ASIs. This clearly indicates to us, that despite recent work [Nishimura et al., 2010], flows are not a necessary condition for substorm onset.

The observations presented here provide evidence that under some conditions, the inside-out scenario for magnetic substorms is valid. The substorm being initiated on closed field lines in the inner magnetosphere following the development of a localised plasma instability which leads to current disruption and the formation of the SCW. Under appropriate conditions, such as during the second substorm, plasma sheet thinning can enable the formation of a near-Earth X line and trigger reconnection further down the magnetotail. Based on the results in this paper, we suggest that substorm onset might in general be triggered by either the release of stored energy in the near-Earth plasmashield, or by tail reconnection, or both – the relative timing of energy release between either (or both) of these regions being determined by ambient conditions. In this way, various potentially complex timing interdependencies between the ionosphere, near-Earth plasmashield, and magnetotail are possible. Though it is clear that additional quantitative statistical studies are required to conclusively demonstrate this.

In short, either or even both unstable regions can form and coexist in the tail; one at the transition between dipole and stretched field in the inner magnetosphere, and the other in the thin plasma sheet further down tail. In this scenario either or both regions may become unstable, dependent on local plasma and magnetic field conditions such that reconnection may proceed the formation of any inner magnetospheric plasma instability or vice-versa. Note, however, that regardless of the process which initiates any particular substorm, even if it occurs in the inner magnetosphere, reconnection likely remains a critical element in the substorm cycle. Only under the action of tail reconnection can there be a large scale reconfiguration of the night-side magnetotail and plasmasheet. Regardless of the link between the inner magnetosphere and formation of a near-Earth X line, our observations clearly demonstrate that the two substorms studied here initiate in the inner magnetosphere, and only in the case of the second substorm does reconnection follow substorm onset. Consequently this also demonstrates that magnetotail flows (or their auroral counterparts in the form of streamers) are not a necessary condition for substorm onset.

## 5.6 References

- Akasofu, S. I. (1964), The development of the auroral substorm, *Planet. Space Sci.*, 12, 273–282, doi:10.1016/0032-0633(64)90151-5.
- Akasofu, S. I. (1977), *Physics of Magnetospheric Substorms*, D. Reidel Publishing Company, Dordrecht.
- Angelopoulos, V., et al. (1994), Statistical characteristics of bursty bulk flow events, *J. Geophys. Res.*, 99(A11), 21257–21280, doi:10.1029/94JA01263.
- Angelopoulos, V., et al. (2008), Tail reconnection triggering substorm onset, *Science*, doi:10.1126/science.1160495.
- Angelopoulos, V., et al. (2009), Response to comment on “Tail reconnection triggering substorm onset,” *Science*, 324(5933), 1391.
- Auster H. U., et al. (2008), The THEMIS Fluxgate Magnetometer. *Space Science Reviews*. doi:10.1007/s11214-008-9365-9

- Baker, D. N., E. W. Hones Jr., R. D. Belian, P. R. Higbie, R. P. Lepping, and P. Stauning (1982), Multiple-spacecraft and correlated riometer study of magnetospheric substorm phenomena, *J. Geophys. Res.*, 87(A8), 6121–6136, doi:10.1029/JA087iA08p06121.
- Baker, D. N., T. I. Pulkkinen, V. Angelopoulos, W. Baumjohann, and R. L. McPherron (1996), Neutral line model of substorms: Past results and present view, *J. Geophys. Res.*, 101(A6), 12,975–13,010, doi:10.1029/95JA03753.
- Blanchard, G. T., L. R. Lyons, J. C. Samson, and F. J. Rich (1995), Locating the polar cap boundary from observations of 6300 Å auroral emission, *J. Geophys. Res.*, 100(A5), 7855–7862, doi:10.1029/94JA02631.
- Brown, R. R., Electron precipitation in the auroral zone, *Space Sci. Rev.*, 5, 311, 1966.
- Donovan, E. F., et al. (2003), All-sky imaging within the Canadian CANOPUS and NORSTAR projects, *Sodankyla Geophys. Obs. Publ.*, 92, 109–112.
- Donovan, E. F., et al. (2007), The azimuthal evolution of the substorm expansive phase onset, in *Proceedings of the Eighth International Conference on Substorms*, edited by M. Syrjäsoo and E. Donovan, pp. 55–60, Univ. of Calgary, Calgary, Alberta, Canada.
- Donovan, E., et al. (2008), Simultaneous THEMIS in situ and auroral observations of a small substorm, *Geophys. Res. Lett.*, 35, L17S18, doi:10.1029/2008GL033794.
- Elphinstone, R. D., et al. (1995), Observations in the vicinity of substorm onset: Implications for the substorm process, *J. Geophys. Res.*, 100(A5), 7937–7969, doi:10.1029/94JA02938.
- Erickson, G. M., R. A. Wolf, Is steady convection possible in Earth's magnetotail, *Geophys. Res. Lett.*, 7, 897, 1980.
- Erickson, G. M., et al. (2000), Electromagnetics of substorm onsets in the near-geosynchronous plasma sheet, *J. Geophys. Res.*, 105(A11), 25265–25290, doi:10.1029/1999JA000424.

- Hau, L.-N., R. A. Wolf, G.-H. Voigt, C. C. Wu, Steady state magnetic field configurations for Earth's magnetotail, *J. Geophys. Res.*, 94, 1303, 1989.
- Huba, J. D., N. T. Gladd, and K. Papadopoulos (1977), The lower-hybrid-drift instability as a source of anomalous resistivity for magnetic field line reconnection, *Geophys. Res. Lett.*, 4, 125–128, doi:10.1029/GL004i003p00125.
- Liang, J., et al. (2008), Intensification of preexisting auroral arc at substorm expansion phase onset: Wave-like disruption during the first tens of seconds, *Geophys. Res. Lett.*, 35, L17S19, doi:10.1029/2008GL033666.
- Lui, A. T. Y. et al. (1995), Preliminary nonlocal analysis of cross-field current instability for substorm expansion onset, *J. Geophys. Res.*, 100, 19147.
- Lui, A. T. Y. (1996), Current disruption in the Earth's magnetosphere: Observations and models, *J. Geophys. Res.*, 101, 13,067–13,088, doi:10.1029/96JA00079.
- Lui, A. T. Y. (2009), Comment on “Tail reconnection triggering substorm onset,” *Science*, 324(5933), 1391, doi:10.1126/science.1167726.
- Lysak, R. L., Feedback instability of the ionospheric resonant cavity, *J. Geophys. Res.*, 96, 1553, 1991.
- Mann, I. R., et al. (2008), The Upgraded CARISMA magnetometer array in the THEMIS era, *Space Sci. Rev.*, 141, 413–451, doi:10.1007/s11214-008-9457-6.
- Maynard, N. C. et al. (1996a), Dynamics of the inner magnetosphere near times of substorm onsets, *J. Geophys. Res.*, 101(A4), 7705–7736, doi:10.1029/95JA03856.
- Maynard, N. C., W. J. Burke, G. M. Erickson, E. M. Basinska, and A. G. Yahnin (1996b), Magnetosphere-ionosphere coupling during substorm onset, in *Third International Conference on Substorms (ICS-3)*, Eur. Space Agency Spec. Publ., ESA SP389, pp. 301–305, Noordwijk, Netherlands.
- Maynard, N. C., et al. (1997), Geotail measurements compared with the motions of high-latitude auroral boundaries during two substorms, *J. Geophys. Res.*, 102(A5), 9553–9572, doi:10.1029/97JA00307.

- Maynard, N. C., G. M. Erickson, W. J. Burke, and G. R. Wilson (1998), Magnetospheric electric fields during substorm onset and expansion phases, in *Substorms*, 4, edited by S. Kokubun, and Y. Kamide, pp. 605–610, Kluwer Acad., Dordrecht.
- McFadden, J.P., et al. (2008), The THEMIS ESA Plasma Instrument and In-flight Calibration. *Space Science Reviews*. doi:10.1007/s11214-008-9440-2
- McPherron, R. L. (1970), Growth Phase of Magnetospheric Substorms, *J. Geophys. Res.*, 5592-5599.
- McPherron, R. L., C. T. Russell, and M. P. Aubry (1973), Satellite studies of magnetospheric substorms on August 15, 1968: 9. Phenomenological model for substorms, *J. Geophys. Res.*, 78(16), 3131–3149, doi:10.1029/JA078i016p03131.
- Mende, S., et al. (2008), The THEMIS array of ground based observatories for the study of auroral substorms, *Space Sci. Rev.*, 141, 357–387, doi:10.1007/s11214-008-9380-x.
- Milan, S. E., A. Grocott, and B. Hubert (2010), A superposed epoch analysis of auroral evolution during substorms: Local time of onset region, *J. Geophys. Res.*, 115, A00I04, doi:10.1029/2010JA015663.
- Miyashita, Y., et al. (2009), A state-of-the-art picture of substorm-associated evolution of the near-Earth magnetotail obtained from superposed epoch analysis, *J. Geophys. Res.*, 114, A01211, doi:10.1029/2008JA013225.
- Motoba, T. et al. (2012), Magnetic conjugacy of northern and southern auroral beads, *Geophys. Res. Lett.*, 39, L08108, doi:10.1029/2012GL051599.
- Murphy, K. R., I. R. Mann, I. J. Rae, C. L. Waters, B. J. Anderson, D. K. Milling, H. J. Singer, and H. Korth (2012), Reduction in field-aligned currents preceding and local to auroral substorm onset, *Geophys. Res. Lett.*, 39, L15106, doi:10.1029/2012GL052798.
- Nakamura, R. et al. (2001), Earthward flow bursts, auroral streamers, and small expansions, *J. Geophys. Res.*, 106(A6), 10,791–10,802, doi:10.1029/2000JA000306.

- Nishimura, Y., et al. (2010), Substorm triggering by new plasma intrusion: THEMIS all-sky imager observations, *J. Geophys. Res.*, 115, A07222, doi:10.1029/2009JA015166.
- Rae, I. J., et al. (2004), Comparison of photometer and global MHD determination of the open-closed field line boundary, *J. Geophys. Res.*, 109, A01204, doi:10.1029/2003JA009968.
- Rae, I. J., et al. (2009), Near-Earth initiation of a terrestrial substorm, *J. Geophys. Res.*, 114, A07220, doi:10.1029/2008JA013771.
- Rae, I. J., et al. (2010), Optical characterization of the growth and spatial structure of a substorm onset arc, *J. Geophys. Res.*, 115, A10222, doi:10.1029/2010JA015376.
- Reeves, G. D., et al. (1990), Multi-satellite measurements of the substorm injection region, *Geophys. Res. Lett.*, 17, 2015-2018.
- Reeves, G. D., et al. (1996) Radial Propagation of Substorm Injection Fronts, International Conference on Substorms, Proceedings of the 3rd International Conference held in Versailles, 12-17 May 1996. Edited by E.J. Rolfe and B. Kaldeich. ESA SP-389. Paris: European Space Agency, 1996., p.579
- Roux, A., S. Perraut, P. Robert, A. Morane, A. Pedersen, A. Korth, G. Kremser, B. Aparicio, D. Rodgers, and R. Pellinen (1991), Plasma sheet instability related to the westward travelling surge, *J. Geophys. Res.*, 96, 17,697–17,714, doi:10.1029/91JA01106.
- Russell, C. T., et al. (2008), THEMIS ground-based magnetometers, *Space Sci. Rev.*, 141, 389–412, doi:10.1007/s11214-008-9337-0.
- Samson, J. C., L. R. Lyons, P. T. Newell, F. Creutzberg, and B. Xu (1992), Proton aurora and substorm intensifications, *Geophys. Res. Lett.*, 9(21), 2167–2170, doi:10.1029/92GL02184.
- Sergeev, V. A., V. Angelopoulos, and R. Nakamura (2012), Recent advances in understanding substorm dynamics, *Geophys. Res. Lett.*, 39, L05101, doi:10.1029/2012GL050859.

- Shiokawa, K., et al. (1998), Azimuthal pressure gradient as driving force of substorm currents, *Geophys. Res. Lett.*, 25, 959.
- Singer, H. J., et al. (1996), Monitoring space weather with the GOES magnetometers, *Proc. SPIE Int. Soc. Opt. Eng.*, 2812, 299–308.
- Tsyganenko, N. A. (1989) A magnetospheric magnetic field model with a warped tail current sheet, *Planet Space Sci.*, 37, 5-20.
- Voronkov, I., et al. (1997), Coupling of shear flow and pressure gradient instabilities, *J. Geophys. Res.*, 102(A5), 9639–9650, doi:10.1029/97JA00386.
- Walsh, A. P., C. J. Owen, A. N. Fazakerley, C. Forsyth, and I. Dandouras (2011), Average magnetotail electron and proton pitch angle distributions from Cluster PEACE and CIS observations, *Geophys. Res. Lett.*, 38, L06103, doi:10.1029/2011GL046770.

## Chapter 6 Conclusions and Future Work

In this thesis we have highlighted the importance of ULF waves, FACs and magnetosphere-ionosphere coupling in the development of the magnetospheric substorm and provided strong evidence that substorm onset can, at times, be initiated in the inner magnetosphere. Chapter 2 presented a statistical analysis of ULF waves in three period bands ( $Pi1^*$ ,  $Pi1-2$ , and  $Pi2$ ) during the substorm growth and expansion phases. In particular it was shown that the ULF wave power spectra observed during substorms is characteristic of a power law and that the spatial distribution of wave polarisation in the three ULF waves bands is consistent with the expected pattern in the presence of a SCW [Lester et al., 1983]. These results strongly suggest that the separation of  $Pi$  type ULF waves into distinct wavebands based on period alone [Jacobs et al., 1964 and Bösinger et al., 1981] is artificial and that during substorms different impulsive ULF waves are excited by the same physical process. Moreover, the entire spectrum of ULF waves should be carefully analysed when studying substorms rather than selecting one specific frequency band.

In Chapter 3 we examined the global FAC morphology associated with a clear substorm on 16 February 2010. We demonstrated for this particular substorm that there was a clear reduction in FACs coupling the ionosphere and magnetosphere at least six minutes prior to auroral onset. Following the reduction in FACs, a new auroral arc formed on closed field lines which brightened and expanded poleward signifying the onset of the substorm. We argued that the change in FACs observed prior to onset is the result of a localised change in M-I coupling. Such a change implies an important role for M-I coupling in destabilizing the inner magnetosphere at substorm onset and perhaps more importantly selecting the location in the ionosphere where auroral onset begins. In Chapter 4 we presented a detailed two-dimensional view of the FACs associated with the substorm expansion phase utilising in-situ observations from AMPERE and ground-based auroral and magnetometer observations. We demonstrated that the structure of FACs forming during the expansion phase and comprising the SCW are significantly more complex than the simple equivalent current model of the SCW [McPherron et al., 1973]. These observations provide important insight into the two-dimensional structure of FACs coupling the magnetosphere and ionosphere and more importantly in determining

how the magnetosphere and ionosphere couple during substorms and especially for understanding the generator responsible for driving FACs and the formation of the SCW.

Finally in Chapter 5 we presented a comprehensive ground and in-situ analysis of two substorms on 9 April 2011. Using auroral observations we demonstrated that for both substorms the initial signature of substorm onset was the localised brightening and azimuthal expansion of the aurora on closed field lines. In both substorms, auroral onset precedes in-situ signatures of onset seen at geosynchronous orbit and in the tail. In addition a dipolarisation of the tail was only observed during the second substorm, and not in the first; only in the latter case was the onset followed by a thinning and subsequent rapid expansion of the night-side plasma sheet. The observations presented in Chapter 5 provides evidence that expansion phase onset can be initiated in the inner magnetosphere on closed field lines. In addition these observations strongly imply that substorm onset can precede magnetic reconnection in the tail and that fast flows or auroral streamers are not a necessary condition for substorm onset.

The observations presented in this thesis clearly demonstrate that M-I coupling most likely plays a crucial role in the onset of substorms and subsequent development of the substorm expansion phase. In addition it has been shown that substorms can be initiated in the inner magnetosphere, apparently independent of the onset of fast magnetic reconnection in the near-tail. Despite this, it remains unclear how M-I coupling influences substorm onset and what physical processes might both link M-I coupling to onset and also lead to the formation and development of FACs through onset and the formation of the substorm current wedge.

Strong evidence has been presented in the literature in support of both the current disruption [Rae et al., 2009] and near Earth neutral line models of substorm onset [Angelopoulos et al., 2008]. As the tail stretches, during the substorm growth phase, two potentially unstable regions form in the inner magnetosphere. One is the transition region between dipole and tail magnetic field where plasma instabilities can most easily form, and a second in the thin current sheet where fast reconnection can more easily take place. Indeed, given recent evidence, it is likely that substorms could be initiated in both regions depending on the prevailing plasma physical conditions. Thus it becomes important to determine whether one happens more often than the other, and, with

regards to current disruption, determining which instability (or instabilities) might lead to substorm onset. Key to addressing these issues is multi-point observations on the ground, at low-altitudes, and in-situ in the inner-magnetosphere and in the magnetotail. With the recent launch of the Van Allen Probes, combined with current ground-based infrastructure, AMPERE, THEMIS, Cluster and the geosynchronous GOES satellites, there is unprecedented coverage of the night-side magnetosphere. Though conjunctions of these assets remains largely fortuitous, future studies will continue to benefit from such conjunctions. These can be used to address the role of M-I coupling in the expansion phase and for characterising the plasma instability which may lead to substorm onset which are initiated independently of reconnection. In addition, such a large array of instrumentation and coverage of the magnetosphere will allow for statistical studies to determine the dominant location and physical processes leading substorm onset. It is hoped that the results presented in this thesis will both guide and stimulate future studies of the magnetospheric substorm.

## 6.1 References

- Angelopoulos, V., et al. (2008), Tail reconnection triggering substorm onset, *Science*, 321(5891), 931-935, doi:10.1126/science.1160495.
- Bösinger, T., et al. (1981), Correlation between Pi type magnetic micropulsations, auroras, and equivalent current structures during two isolated substorms, *J. Atmos. Terr. Phys.*, 43(9), 933-945.
- Jacobs, J. A., et al. (1964), Classification of Geomagnetic Micropulsations, *J. Geophys. Res.*, 69(1), 180-181.
- Lester, M., W. J. Hughes, H. J. Singer, Polarization patterns of Pi2 magnetic pulsations and the substorm current wedge, *J. Geophys. Res.*, 88, 7958, 1983.
- McPherron, R. L., C. T. Russell, and M. P. Aubry (1973), Satellite studies of magnetospheric substorms on August 15, 1968: 9. Phenomenological model for substorms, *J. Geophys. Res.*, 78(16), 3131–3149, doi:10.1029/JA078i016p03131.
- Rae, I. J., et al. (2009), Near-Earth Initiation of a Terrestrial Substorm, *J. Geophys. Res.*, doi:10.1029/2008JA013771.

